UNIVERSIDAD POLITÉCNICA DE MADRID

ESCUELA TÉCNICA SUPERIOR DE INGENIERÍA
AERONAÚTICA Y DEL ESPACIO

Entropy, chaos and irreversibility in the turbulence energy cascade

Alberto Vela Martín

Ingeniero Aeronaútico

September 2019

POLITÉCNICA

DEPARTAMENTO DE MECÁNICA DE FLUIDOS Y
MOTOPROPULSIÓN

Entropy, chaos and irreversibility in the turbulence energy cascade

AUTOR

Alberto Vela Martín

DIRECTOR

Javier Jiménez

September 2019

"I do not find the Hanged Man. Fear death by water."

The Wasteland, T.S. Elliot

Abstract

This thesis studies the turbulent energy cascade from the perspective of statistical mechanics and relates inter-scale energy fluxes to information-entropy production. The microscopical reversibility of the energy cascade is tested by constructing a reversible 3D turbulent system using a dynamic model for the sub-grid stresses. This system, when reversed in time, develops a sustained inverse cascade towards the large scales, evidencing that the characterization of the inertial energy cascade must consider the possibility of an inverse regime. This experiment suggests the introduction of a probabilistic concept, namely entropy, to explain the prevalence of direct over inverse energy cascades. Entropy production, as a statistical property of ensembles in phase space, is connected to the dynamics of the energy cascade in physical space by considering the space locality of the energy fluxes and their relation to the local structure of the flow. An entropic mechanism for the prevalence of direct energy transfer is proposed based on the dynamics of the rate-of-strain tensor, which is identified as an important indicator of statistical irreversibility in the energy cascade. A deeper analysis of the entropy generation mechanisms is accomplished by defining a space-local measure of phase-space mixing based on the Lyapunov exponents. The statistics of this quantity consistently reveal that the dynamics of the rate-of-strain tensor are fundamentally connected to entropy production. This analysis, which also describes the spatio-temporal structure of chaos in the energy cascade, reveals a strong localization of highly chaotic and entropy-producing events in the vicinity of interacting vortical structures.

Resumen

Esta tesis estudia la cascada de energía turbulenta desde la perspectiva de la mecánica estadística, y relaciona los flujos de energía entre escalas con la producción de caos y entropía. Se estudia la reversibilidad microscópica de la cascada de energía mediante la construcción de un sistema turbulento reversible, que utiliza un modelo dinámico para modelar los esfuerzos de submalla. Este sistema, cuando se invierte en el tiempo, desarrolla una cascada inversa sostenida hacia las escalas grandes, evidenciando que la caracterización de la cascada de energía inercial debe considerar la posibilidad de un régimen inverso. Este experimento sugiere la introducción del concepto probabilístico de la entropía para explicar la prevalencia de cascadas directas sobre inversas. Este trabajo conecta la producción de entropía, como una propiedad estadística de los conjuntos de experimentos en el espacio de fases, con la dinámica de la cascada de energía en el espacio físico. Para ello se considera la localidad espacial de los flujos de energía y su relación con la estructura local del flujo. En base a este análisis, se propone un mecanismo entrópico para la prevalencia de transferencia de energía directa basado en la dinámica del tensor de velocidades de deformación, que se identifica como el principal indicador de irreversibilidad estadística en la cascada de energía. Un análisis más profundo de los mecanismos de generación de entropía se lleva a cabo definiendo una medida local, en el espacio físico, de la generación de entropía basada en los exponentes de Lyapunov. Las estadísticas de esta cantidad indican que la dinámica del tensor de velocidad de deformación esta fundamentalmente relacionado con la producción de entropía. Este análisis, que describe la estructura espacio-temporal del caos en la cascada de energía, revela una fuerte localización de eventos áltamente caóticos y productores de entropía en la vecindad de estructuras vorticales que interactuan entre ellas.

Acknowledgements

I would like to thank my family, specially Nadia, friends, and work colleagues for their support and encouragement during the final stages of this thesis. I thank Lindy Hop for making these years probably one of the happiest times in my life, and for not letting me take anything too seriously.

I would like to thank my advisor, Javier Jiménez, for choosing a beautiful topic that has allowed me to get in touch with the fascinating field of non-equilibrium thermodynamics. I also thank him for passive and actively fostering my independence.

Contents

Abbreviations

CMT	**C**onditional **M**ean **T**rajectory
DNS	**D**irect **N**umerical **S**imulation
FR	**F**luctuation **R**elations
GPU	**G**raphic **P**rocessing **U**nit
HLE	**H**ighest **L**yapunov **E**xponent
KS	**K**olmogorov–**S**inai
LE	**L**yapunov **E**xponent
LES	**L**arge **E**ddy **S**imulation
LILE	**L**argest **I**nertial **L**yapunov **E**xponent
LLE	**L**owest **L**yapunov **L**yapunov **E**xponent
LV	**L**yapunov **V**ector
NED	**N**on-**E**quilibrium **D**ynamics
NS	**N**avier–**S**tokes
SGS	**S**ub-**G**rid **S**tresses

Symbols

Operators

$\langle\cdot\rangle$	Spatial average
$\widehat{\cdot}$	Fourier transform
$\tilde{\cdot}$, $\bar{\cdot}$, $\check{\cdot}$	Filtering operations
$\cdot'$	Quantity without the spatial average
$\langle\cdot\rangle_m$	Conditional average
$\langle\cdot\rangle_C$	Conditional average in the Q–R space
$\langle\cdot\rangle_{q_i}$	Conditional average to the quadrants of the Q–R space
$\{\cdot\}_{q_i}$	Contribution to the total average of quadrants in the Q–R space
$\langle\cdot\rangle_k$	Average over wave-number shells
∂	Partial derivative
$\cdot^T$	Traceless tensor
d_t	Absolute temporal derivative
D_t	Convective derivative
$\cdot^*$	Complex conjugate
$\lvert\cdot\rvert$	Absolute value

Greek letters

$\alpha_1 > \alpha_2 > \alpha_3$	Eigenvalues of the rate-of-strain tensor
β	Threshold
Γ	Amplification of the Lyapunov vector in scale space
Δ	Scale
Δ_g	Grid spacing
ϵ	Dissipation
ϵ_s	Sub-grid energy transfer
ζ	Test field

η	Kolmogorov length scale
η_s	Pseudo-Kolmogorov length scale
h_{KS}	Kolmogorov–Sinai entropy
H	Information entropy
θ_1, θ_2, θ_3	Angles with respect to the eigenvectors of the rate-of-strain tensor
λ	Lyapunov exponents
λ_{st}	Short-time Lyapunov exponent
λ^+	Highest Lyapunov exponent
λ^-	Lowest Lyapunov exponent
λ_ℓ	Space-local Lyapunov exponent
Λ	Kinetic energy of the Lyapunov vector
μ	Perturbation intensity
ν	Kinematic viscosity
ν_s	Eddie viscosity
ξ	Test field
π	Pi number
Π	Energy fluxes in Fourier space
ρ	Error in Fourier space
σ	Standard deviation
σ_0	Standard deviation without volume average
σ_V	Standard deviation after volume average
Σ	Energy transfer in physical space
τ_{ij}	Sub-grid stress tensor
υ_2	Contribution of the non-local component of the pressure Hessian in the evolution of α_2
Υ	Accessible phase-space volume
ϕ	Angle
φ	Test field
$\mathbf{\Phi}$	Probability transport velocity in the Q–R space
$\mathbf{\Xi}$	State vector in phase space
Ψ	Energy transfer in physical space
$\boldsymbol{\omega}$	Vorticity vector
ϖ	Asymmetry function in the Q–R space
Ω	Dissipation function

Roman letters

a	Threshold
$\boldsymbol{B}$	Non-linear terms of the Navier–Stokes equation
C	Dynamic LES local model parameter
C_s	Dynamic LES average model parameter
$\mathfrak{D}$	Distance in phase space
$E(k)$	Energy spectrum
$E_{\boldsymbol{ab}}$	Energy co-spectrum of $\boldsymbol{a}$ and $\boldsymbol{b}$
$\mathcal{E}$	Kinetic energy density
$G(k)$	Gaussian filter
$\boldsymbol{k}$	Wave-number vector
k	Wavenumber magnitude
ℓ	Correlation length
L	Integral scale
$\mathcal{L}$	Sub-grid scale tensor difference
$\mathfrak{L}$	Forcing scale
$\boldsymbol{M}$	LES model
$\mathcal{M}$	Sub-grid model tensor difference
n	Number of degrees of freedom
N	Grid points
p	Modified pressure
P	Probability density
$\mathcal{P}$	Asymmetry function
q	Wave-number
q_i	Quadrant in the Q–R plane
Q	Second invariant of the velocity gradient tensor
R	Third invariant of the velocity gradient tensor
$\mathcal{R}$	Correlation in scale
Re	Reynolds number
S_{ij}	Rate-of-strain tensor
$\mathcal{S}$	Correlation in space
t	Time
t_s	Pseudo-Kolmogorov time

t_{inv}	Inversion time
T	Eddy-turnover time
$\boldsymbol{u}$	Velocity vector
U	Root-mean square of the velocity
$\mathfrak{U}$	Forcing velocity
$\boldsymbol{v}_i$	Eigenvectors of the rate-of-strain tensor
V	Volume
$\boldsymbol{x}$	Position vector

Chapter 1

Introduction

Turbulence is an ubiquitous phenomena in nature and constitutes one of the most important unsolved problems of classical mechanics. The energy cascade is the fundamental process shared by almost all turbulent flows, and plays a central role in turbulence theory. The study of the cascade has been addressed in different ways, and the objects used to describe it are many. In this thesis, we approach the study of the cascade from the perspective of statistical mechanics and dynamical system theory.

Here, we offer an informal and brief introduction, first, to turbulence and the energy cascade, and, second, to dynamical system theory and statistical mechanics. For a more detailed introduction to turbulence the reader is referred to the work of Lesieur [1] and Pope [2]. An extensive account of the theory of the cascade is given in the remarkable book of Frisch [3], and a critical review of the state of turbulence theory can be found in the work of Tsinober [4]. We also propose [5] and [6] as more extensive introductions to dynamical system theory and statistical mechanics.

1.1 The turbulent energy cascade

1.1.1 What is turbulence and what equations describe it?

Describing turbulence in a few sentences is perhaps as difficult and as impossible as the 'problem' of turbulence itself. Such effort would imply reducing the results of countless

experiments, empirical observations and potential theories to a few words. As a short definition, we choose the words of Tsinober [7]:

"Turbulence is the manifestation of the spatio-temporal chaotic behaviour of fluid flows at large Reynolds numbers, i.e. of a strongly nonlinear dissipative system with a extremely large number of degrees of freedom (most probably) described by the Navier-Stokes equations."

We also refer to the appendices of the same reference [7], where the reader can find a collection of short descriptions of turbulence by relevant figures in turbulence research. In this chapter we will address many of the relevant features of turbulent flows, which serves as a firsthand introduction to the phenomena of turbulence.

Let us start by introducing the Navier–Stokes (NS) equations, which govern the evolution of incompressible fluids,

$$\begin{aligned} \partial_t u_i + u_j \partial_j u_i &= -\partial_i p + \nu \partial_{kk} u_i, \\ \partial_i u_i &= 0, \end{aligned} \tag{1.1}$$

where u_i is the i-th component of the velocity vector, $\boldsymbol{u}$, ∂_i is the partial derivative with respect to the i-th direction, p is a modified pressure, and ν is the kinematic viscosity of the fluid. Repeated indices imply summation. It is widely accepted that, these equations, together with appropriate initial and boundary conditions describe the evolution of incompressible turbulent flows.

Dimensional analysis shows that the NS equations depend only on a single dimensionless number, the Reynolds number $Re = UL/\nu$, which compares the advection of momentum with the diffusion of momentum. Here U is a characteristic velocity and L is a characteristic length of the flow.

1.1.2 The classical theory of the cascade

The turbulent cascade is a scientific paradigm that dates back to the pioneering work of Richardson [8] and the celebrated papers of Kolmogorov [9, 10], who laid the theoretical foundations for the study of turbulence. Generally speaking, the energy cascade is the process that transports energy from the large to the small scales, accounting for the gap between scales where energy is produced, and scales where it is dissipated. This

process is intrinsically related to the ability of turbulent flows to dissipate energy even at vanishing viscosity.

Let us consider a flow in the absence of walls, or a mean shear, contained in a volume V, and a forcing mechanism acting at scale $\mathfrak{L}$ with a typical velocity $\mathfrak{U}$. In the steady state, the temporal average of the amount of energy injected per unit volume by the forcing mechanism is equal to the volume-averaged energy dissipation,

$$\epsilon = \frac{1}{V}\int_V \nu(\partial_j u_i)^2 dV, \tag{1.2}$$

which depends on the kinematic viscosity and on the intensity of the velocity gradients. Empirical evidence show that, in the limit of vanishing kinematic viscosity, the average energy dissipation is not zero, and depends only on $\mathfrak{L}$ and $\mathfrak{U}$, such that $\epsilon \sim \mathfrak{U}^3/\mathfrak{L}^2$ [11, 12].

Surprisingly, the kinematic viscosity might become arbitrarily small while keeping the dissipation fixed. As shown by (1.2), this can only be a consequence of the growth of the velocity gradients magnitude. This surprising phenomenon is known as the dissipative anomaly, and constitutes one of the most relevant empirical foundations of turbulence theory.

To account for the dissipative anomaly the classical theory of the cascade by Kolmogorov [10] and Onsager [13], among others, describes turbulence as a multiscale physical phenomenon, which takes place between the 'large' scales of the forcing mechanism, and the 'small' scales of the velocity gradients. While the large scales of the flow are fixed by $\mathfrak{L}$, the scale of the velocity gradients can become arbitrarily small in order to produce enough dissipation, regardless of the value of the kinematic viscosity. For a sufficiently small ν, the spatial scales of the velocity gradients are much smaller than $\mathfrak{L}$, and their dynamics are assumed to be decoupled from those of the integral scales of the flow, and therefore universal [14].

Under this assumption of universality, the statistics of the velocity gradients depend only on ν and ϵ, leading to the so called Kolmogorov length- and time-scale, $\eta = (\nu^3/\epsilon)^{1/4}$ and $t_\eta = (\nu/\epsilon)^{1/2}$, which describe the temporal and spatial scale of dissipatve mechanisms. Considering that $\epsilon \sim \mathfrak{U}^3/\mathfrak{L}$, the ratio between the dissipative scales and the integral scales of the flow are

$$\frac{\mathfrak{L}}{\eta} \sim Re_{\mathfrak{L}}^{3/4} \qquad \frac{\mathfrak{T}}{t_\eta} \sim Re_{\mathfrak{L}}^{1/2} \tag{1.3}$$

where $\mathfrak{T} = \mathfrak{L}/\mathfrak{U}$ is the integral time-scale, and $Re_{\mathfrak{L}} = \mathfrak{U}\mathfrak{L}/\nu$ is the Reynolds number based on the integral scale, which measures the separation between the integral and dissipative scales of the flow. By increasing this parameter, it is possible to make the gap between the integral and dissipative scales arbitrarily large.

The energy cascade is the fundamental process that bridges this gap by transporting the energy from the 'large' scales to the 'small' scales. The term cascade is not used here freely, but deliberately illustrates a fundamental property of this process: locality. Just as water flows down a cascade step by step, the energy transport from the large to the small scales takes place in a stepwise manner between $\mathfrak{L}$ and η.

In the limit of high Re, locality implies that the energy cascade occurs across scales that are too small to be affected by the energy injection mechanisms and too large to be affected by the dissipation. These scales, known as the inertial scales, are driven only by inertial forces, i.e the advection and the pressure terms in the NS equations, which conserve the kinetic energy. Hence, the flux of energy from the large to the small scales is similar at all scales in the inertial range, and equal to the average rate of energy dissipation.

The cascade theory assumes that the details of the forcing mechanisms are lost across multiple 'steps' of the cascade, and the statistics of the inertial range depend only on the scale, Δ, and on the average energy flux, which matches the dissipation. This assumption led Kolmogorov [10] to propose a self-similar structure of the inertial range: the statistics of the inertial range depend on the scale through powerlaw expressions of the form Δ^{γ}, where γ is a characteristic exponent which is derived from dimensional arguments. In particular, self-similarity implies that the turbulent kinetic energy spectrum $E(k)$, a second-order statistic of the velocity field, has the following form

$$E(k) \sim \epsilon^{2/3} k^{5/3}, \tag{1.4}$$

where $E(k)$ measure of the distribution of kinetic energy across scales, and $k \sim 1/\Delta$ is the wavelength, the inverse of the scale [1]. This form of the energy spectrum in fully developed turbulence has been obtained in experiments and numerical simulations [12, 15, 16], constituting one of the main predictions of the Kolmogorov theory, and a cornerstone of turbulence research. Further evidences of self-similarity in the inertial

scales have been reported, for instance, in the temporal fluctuations of the average energy fluxes [17], or in the clustering of small heavy particles [18].

However, the Kolmogorov theory fails to predict higher-order statistics of the velocity field, which display anomalous scaling [19]. This is known to be a consequence of the intermittent structure of turbulent flows. Turbulent quantities, such as the dissipation or the filtered kinetic energy, are not homogeneously distributed in space, but peak intensely in reduced regions of the flow. This phenomenon locally breaks self-similarity in the statistical sense [3], and imposes a reinterpretation of the classical theory. Although alternative models have been proposed to account for the intermittent structure of turbulence [20–22], numerical simulations at high Reynolds number reveal that the structure of the flow is far more complex than what originally proposed [23–26], and suggest that the classical theory must be reinterpreted to consider the available tools and data. Another important drawback of this theory is its lack of connection to the NS equations, which are not referred in any of the founding papers by Kolmogorov [9, 10].

Despite all these limitations, the impact of the Kolmogorov theory on turbulence research is undeniable, and the energy cascade constitutes a dominant paradigm in the field. Criticism to the theory of the cascade exist [4, 7], but it is unclear whether alternative theories can offer a better explanation of the empirical evidences. In the sense of Kuhn [27], the field of turbulence seems rather in a stage of refinement of a dominant paradigm, than in a pre-paradigmatic stage.

1.1.3 The energy cascade in physical space

The classical theory of the cascade is mathematically formulated in terms of time-independent statistical objects, such as the energy spectrum or the statistics of the velocity increments, which describe fundamental properties of turbulence in scale space. These statistical objects contain only a limited information on the structure of the flow, and do not account for the dynamical processes that govern the energy cascade, which take place in the spatial and temporal coordinates of turbulent flows.

To account for this limitation, the classical theory provides a complementary phenomenological description of the cascade in physical space. Richardson [8] was the first to suggest that turbulent flows are composed of ‘whirls’, which feed energy to smaller

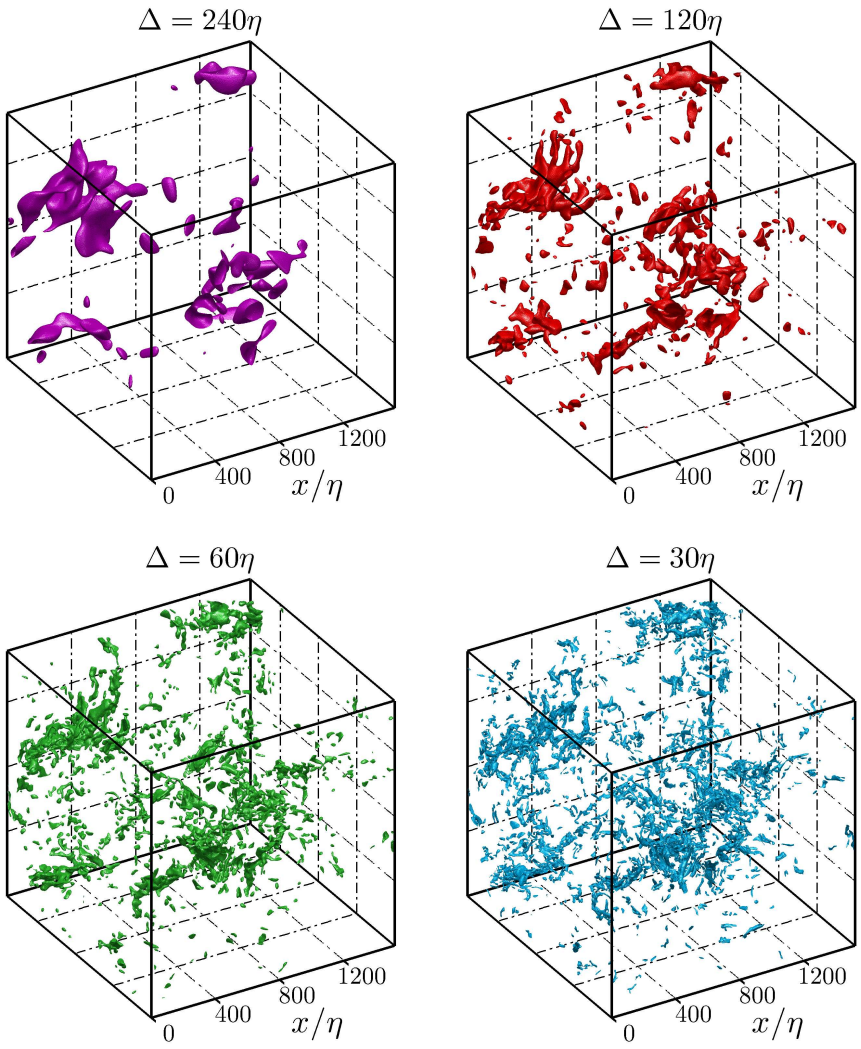

Figure 1.1: Visualisation of bandpass-filtered energy at four different scales in homogeneous isotropic turbulence, where η is the Kolmogorov scale. Figure extracted from [28].

'whirls', which at the same time feed yet smaller 'whirls', and so on until viscosity is able to dissipate them. This simple and rather naive conceptual image introduces the idea of scale and self-similarity, and accounts for the fundamental property of locality.

The modern interpretation of this picture states that 'eddies' 'break' in smaller and smaller pieces until the dissipative scales. However, the concepts of 'eddy' and 'breaking' are in general ambiguously defined, and the relation of these concepts with the turbulent velocity fields and the NS equations is generally not clear. Cardesa et al. [28] identified potential candidates for 'eddies' as isocontours of intense bandpass-filtered energy, which are shown, at different scales, in figure (1.1). The statistical behaviour of these 'eddies' supports, on average, the classical picture of the energy cascade as an 'approximately' local process, but does not reflect the nature of the 'breaking' mechanism.

Let us note that the classical picture of Richardson [8] implies that the cascade is a local process both in physical and scale space, and identifying 'eddies' and their 'breaking' mechanisms must rely on the study of the dynamics of the cascade in physical space. A standard approach to this study is to obtain an equation for the filtered energy in an inertial scale, Δ, by filtering the Navier–Stokes equations with a lowpass filter, leading to an equation with the following generic form,

$$D_t \mathcal{E}_\Delta = \partial_i \mathcal{J}_i - \mathcal{D}, \tag{1.5}$$

where D_t is the material derivative, $\boldsymbol{\mathcal{J}}$ is an energy flux in physical space, and $\mathcal{E}_\Delta$ is the kinetic energy density in space above Δ. The field $\mathcal{D}$ represents a space-local definition of interscale energy fluxes across Δ [17, 29–32]. This field appears as a natural object to determine the 'breaking' mechanisms in physical space, for instance, by identifying statistically significant correlations between regions of high energy transfer across a scale, and the local dynamics of the flow at that same scale.

Unfortunately, this approach faces two fundamental limitations: the uncertainty principle between the representations in scale and physical space, and the changes of the local energy transfer field for different definitions of the fluxes. The first limitation implies that an 'eddy' cannot be sharply localised in scale and physical space at the same time [33]. Therefore, only an approximate degree of locality is achievable in both spaces, for instance, by the use of Gaussian filters or wavelet transforms [34, 35]. The second fundamental limitation stems from the freedom to define the fluxes [36]. In (1.5), only $D_t \mathcal{E}_\Delta$ is directly measurable, while $\boldsymbol{\mathcal{J}}$ and $\mathcal{D}$ depends on the choice of what we consider the relevant interactions among scales, and what is a scale and a scale flux. Infinitely many possible definitions of $\boldsymbol{\mathcal{J}}$ and $\mathcal{D}$ are compatible with (1.5). To fix the fluxes, we must impose additional restrictions, which should be based solely on physical arguments.

Although some physical mechanisms for energy transfer have been proposed [37, 38], there is not, to this date, a general consensus on what mechanisms underlie the cascade process. Vortex stretching is perhaps one of the most popular candidates [39–41]. However, the connection of this mechanism with energy transfer, or with any sort of 'breaking', is not immediate. Moreover, favouring this mechanism over other gradient-producing mechanisms, such as the self-amplification of the rate-of-strain tensor, is probably unjustified [42].

1.2 Numerical experiments of the energy cascade

1.2.1 Direct numerical simulations: tampering with the Navier–Stokes equations

The study of turbulence has traditionally relied on experimental facilities working under controlled and reproducible conditions. These facilities allow to reach high Reynolds numbers [16, 43], but are difficult to instrumentalise and only a limited amount of information is accessible by direct experimental measurements.

Since the advent of the computer era, direct numerical simulations (DNS) of the NS equations have become a relevant tool in turbulence research [44]. Although the achievable Reynolds numbers are still bellow those of industrial applications, this technique offers full information on the spatio-temporal structure of the flow and its dynamics. DNS have fundamentally shaped turbulence research in the last three decades, and its impact is expected to increase in the future due to the growing availability of computational resources.

A perhaps underestimated advantage of direct numerical simulations is the possibility of tampering with the Navier–Stokes equations. A great insight into the dynamics of turbulent flows is possible by modifying the NS equations in ways not possible in experimental facilities. This approach consist of adding, removing or modifying terms in the NS equations [45–47], imposing artificial boundaries [48, 49], or modified initial conditions [50, 51]. The work presented in this thesis relies both, on modifying some terms in the Navier–Stokes equations, and on imposing artificial initial conditions.

1.2.2 Homogeneous isotropic turbulence in a periodic box as a tool to study the energy cascade

One of the fundamental hypothesis of the cascade theory is the local homogeneity and isotropy of the flow, which implies that the statistics of the velocity field should not depend on the position, or in the orientation of the measurements. Nonhomogeneity and anistropy are usually related with the presence of solid walls or mean shears, as in wall-bounded flows, jets or mixing layers. These flows are forced in a preferential direction or are affected by linear instabilities, which give rise to persistent structures that violate the

isotropy hypothesis in the large scales. Since it is not clear how these large structures propagate their influence down the cascade at the limited Reynolds numbers of the available in DNSs [52–54], the study the energy cascade hinges on an ideal experimental setup without large-scale anisotropies.

The fundamental research tool for the turbulence cascade is the so-called 'box'–turbulence, i.e the statistically homogeneous and isotropic turbulence (HIT) generated in a triply periodic box by numerical simulation of the NS equations [55]. This setup is the simplest possible 3D turbulent flow, and takes advantage of the periodic boundary conditions for the efficient integration of the NS equations, allowing to achieve high Reynolds numbers at an affordable computational cost.

1.2.3 GPUs and statistical ensembles

In order to maintain a steady state, and due to the lack of natural forcing mechanisms, box-turbulence is usually forced at the large scales through an artificial negative viscosity. By invoking ergodicity [56], the statistics of the flow can be compiled from a single long simulation, instead of from an ensemble of multiple independent realisations of the same flow. In statistically steady flows, only the initial transient is necessary, and statistics can be compiled once the fully turbulent state is reached. This approach is more convenient from the computational point of view, since obtaining appropriate initial conditions and restarting the simulations is usually expensive.

However, this work deals with a decaying flow, which does not converge to a steady state, and the statistical analysis relies on the generation of ensembles of many different realisations. This approach is possible thanks to the use of highly efficient graphic processing units (GPUs), which allow to run small- and medium-size simulations at an unprecedented speed. As part of this thesis, the author has produced a GPU code to simulate HIT in a triply periodic box with a dynamic Smagorinsky LES model. This code has allowed the generation of ensemble of experiments with $\mathcal{O}(10^3)$ different realisations. GPU codes derived from this one have been used by Flores et al. [57] or Ávila and Vela-Martín [58] to produce ensembles of thousands of experiments, which provide novel insights into the physics of turbulence. In view of the positive results of these experiments, and of the work presented in this thesis, this approach is likely to have an important impact on turbulence research in the next few years.

1.3 Chaos and strange attractors

1.3.1 A dynamical system approach to turbulence

The dynamical system approach to turbulence considers that solutions of the NS equations can be represented by a finite number of degrees of freedom, n. Landau and Lifshitz [59] suggested that n is of the order of the number of degrees of freedom in the inertial range,

$$n \sim \left(\frac{\mathfrak{L}}{\eta}\right)^3 = Re_{\mathfrak{L}}^{9/4}. \tag{1.6}$$

This estimate is justified on the exponential decay of the energy spectrum in the far dissipative range [60]. Moreover, Yoshida et al. [50] and Lalescu et al. [51] showed that the scales below the Kolmogorov scale have no dynamical relevance, since they are constrained by the dissipation and enslaved to larger scales. DNS experiments suggest that this estimate is acceptable, and some investigations indicate that n is probably smaller than expressed in (1.6) [61].

Consequently, we can transform the NS equations, a set of partial differential equations, into a set of ordinary differential equations by projecting them into a finite set of base functions or modes, being the set of truncated Fourier modes an example of practical relevance for HIT [62]. We can now envision a turbulent flow as described by a point in an n dimensional phase space, which represents all possible solutions of the NS equations, and its evolution by a continuous phase-space trajectory. In the limit of infinitely many different experiments, ensembles translate into 'dense' clouds of points in phase-space, and each state of the system can be described by a 'continuous' probability density which changes in time. The introduction of probabilities is justified on the chaotic nature of turbulence dynamics.

1.3.2 Chaos and determinism

By definition, the NS equations are deterministic, i.e the same initial condition always leads to the same flow field after a fixed amount of time, and there is a unique trajectory defined for each phase-space point. However, this is just an idealisation of reality.

Although deterministic, the NS equations are also chaotic: any initial disturbance is amplified in a finite time, leading to the impossibility of exactly reproducing experiments after a finite time.

As a consequence, turbulent flows are intrinsically unpredictable. Assuming that we can only obtain a finite amount of information from the initial conditions of an experiment, the uncertainty on the state of the flow is always amplified in a finite horizon, beyond which, predictions are fundamentally impossible [63]. The chaotic nature of turbulence implies that the exact details of each experiment are not reproducible, i.e the microscopic details of single isolated flow field are irrelevant, and only a statistical treatment of the phenomena of turbulence is meaningful.

1.3.3 Chaos and order: the turbulent attractor

Although both terms are usually used indistinctly, chaos does not imply randomness. Turbulent flows are known not to be random, but to display a recurrent complex spatio-temporal structure. Although each turbulent flow is 'unique', the structure that characterises these flows is universal and reproducible. For instance, each cloud in the sky is unique, but we are intuitively able to identify common patterns in all the clouds. Similarly, the visualisation of different snapshots of the same turbulent flows conveys the idea that they all share a similar common dynamical process. This structure emerges, in most turbulent flows, independently of the initial conditions, and all initial flow fields converge to the same set of states with a common structure, the so-called attractor [56].

The existence of an attractor in steady states is, among other things, a consequence of the dissipative nature of the NS equations, which leads to the contraction of phase-space volume. Since the total probability is conserved, the probability density evolves towards a phase-space volume with zero measure. This volume represents only a negligible fraction of all the possible flow fields compatible with the NS equations, including random structureless fields, supporting the view that turbulence is far from random. The existence of an attracting set of states is probably not exclusively related to the dissipation, but to dynamics far from equilibrium in general. For instance the truncated Euler equations out of equilibrium, which are conservative and volume-preserving, are known to reproduce the behaviour NS turbulence in the inertial range [64, 65]. In this thesis, we

will provide further evidence of the connection between the truncated Euler equations and the NS equations in the inertial range.

The relevant question is what characteristics define the states within this attracting set of states, i.e what makes these states more probable than other states outside the attractor. This question is central to the field of statistical mechanics, and connects with the statistical formalism of classical thermodynamics [66].

1.4 Statistical mechanics

1.4.1 Equilibrium statistical mechanics

The formalism of statistical mechanics, which dates back to the seminal work of Maxwell, Boltzmann and Gibbs, represents a clear success in the description of complex systems through simple statistical objects.

Under the assumption of thermodynamic equilibrium, classical statistical mechanics postulates that systems can be described by a set of thermodynamical variables, reducing the complexity of 'microscopic' interactions to a few characteristic measurable 'macroscopic' quantities. By thermodynamic equilibrium, we refer to a state where no net fluxes of matter or energy appear within the system, and measurable quantities do not fluctuate in time. By microscopic information we refer to the detailed information of the system and all its constituents.

For instance, the kinetic theory of gases models an ideal gas as the interaction of many solid spheres, which collide in a conservative fashion and follow the laws of Newtonian mechanics. In a closed system in equilibrium, the microscopic information about the position and velocity of each isolated sphere is not fundamental for the description of the system at a macroscopic or observable level, which depends only on a few statistical properties of the system. In the simplest case, a confined gas can be described by the average kinetic energy of its particles, which defines the temperature. Provided that the number of particles and the confining volume are known, the pressure exerted by the particles on the walls of the container can be derived.

The success of this statistical approach relies on disregarding the complex dynamics of the solid spheres, and on assuming that the system will not evolve towards special

macroscopic states, but will remain in the equilibrium state. For example, a confined gas in equilibrium will almost always remain homogeneously distributed, and will not spontaneously concentrate in a corner of the container. This assumption is justified on the powerful concept of entropy, which is central to the theoretical corpus of statistical mechanics, and articulates the celebrated 'second law' of thermodynamics.

The second law postulates that the uncertainty of the observer with respect to the microscopic state of a system in equilibrium is maximum. The system can be in any possible microscopic configuration compatible with the macroscopic observables and the laws of motion, and all possible configurations of the system are equally probable. In the case of a confined gas, in the overwhelming majority of these states, the particles are evenly distributed in the container, and the total kinetic energy is 'evenly' distributed across all particles. Therefore the most probable macroscopic state is that in which the density and the temperature of the gas are homogeneous in the container. The uncertainty is quantified by an extensive macroscopic variable, the entropy.

The second law represents an extremal principle for closed systems: the total entropy of a closed system can never decrease and is maximum at equilibrium. By closed system we refer to a system that does not exchange matter, energy or information with other systems. The second law appears as a 'law of laws' that selects the most probable macroscopic state among all possible states consistent with the physical laws that govern the system.

Entropy is also used to explain the 'arrow of time', justifying the tendency of the macroscopic universe to evolve in one definite direction, and bridging the paradox of how reversible microscopic dynamics give rise to an irreversible macroscopic world. If we confine the gas in a corner of the container, the second law states that, after a sufficiently long time, we will again find the gas homogeneously distributed in the container. However, the inverse process will almost never take place.

This is surprising given that Newtonian mechanics, which govern the dynamics of the gas particles, are completely time-reversible, and do not privilege one process over the other. The direct process, in which the gas mixes to fill the empty container, is consistent with the second law as it increases the entropy or uncertainty about the position and velocity of the gas particles. On the other hand, the inverse process decreases the entropy

by reducing the uncertainty: there are less possible ways of placing particles in the corner of the container than in the whole container.

1.4.2 Non-equilibrium statistical mechanics

Unfortunately, the powerful concept of entropy has only been successfully applied to systems in thermodynamic equilibrium, which are by definition an idealisation of the real world. Most systems in nature are very far from equilibrium: temporal variations of macroscopic quantities are observed; there are net flows of matter, energy and other quantities, and the properties of the system fluctuate in time. The second law of thermodynamics postulates that closed systems out of equilibrium will almost surely tend to equilibrium, and that the final state has maximum entropy, but it does not predict how the system approaches equilibrium, namely, at what rate and how the system produces entropy.

Non-equilibrium statistical mechanics tries to explain and predict the behaviour of non-equilibrium dynamics (NED) by extending the equilibrium approach. The success of equilibrium statistical mechanics and of the second law has tempted researchers into proposing that, also the complex evolution non-equilibrium systems can be described by a set of universal statistical principles.

However, the statistical formalism of NED is still under construction, and its foundations are far from solid. This is mostly a consequence of the features of NED, which renders the approach of equilibrium thermodynamics useless: the complexity of NED cannot be fully disregarded.

1.4.3 Non-equilibrium phenomena: space-time fluctuations, structure and fluxes

Almost all non-equilibrium phenomena share at least three universal characteristics.

First, non-equilibrium phenomena must be described by their time-evolution rather than by single, isolated states. Temporal fluctuations are the principal difference between equilibrium states and non-equilibrium evolutions: the former are characterised by time-independent quantities, while, in the latter, quantities change with time. Non-equilibrium

phenomena must be described in terms of rates of change rather than in terms of static, time-independent variables. Although apparently simple, the inclusion of time-evolution breaks the formulation of classical thermodynamics, leading to inconsistencies in the definition of entropy and entropy production [67].

Second, systems out of equilibrium are known to display organised and coherent dynamics [68]. The organised structure of NED seems to be in contradiction with the postulates that justify the second law. In the context of classical statistical mechanics, the description of maximum-entropy states is based on the unlike probability that a microscopically incoherent equilibrium state is able to spontaneously develop macroscopic structure. However, the organisation of incoherent states into macroscopically coherent states is consistently observed when complex systems are driven out of equilibrium. These evidences enforce the construction of a statistical formalism that is able to explain the organisation of non-equilibrium systems, and the role of coherent structures in the dynamics of complex systems. In turbulent flows, complexity and organisation appears in the form of non-Gaussian statistical distributions, intense intermittency of turbulent quantities, or long-lived coherent structures in the flow. This complexity emerges in the temporal and spatial coordinates of turbulent flows, and imply that turbulence must be studied as a spatially-extended system.

Finally, another principal characteristic common to all systems out of equilibrium is the presence of macroscopic fluxes, which transport either energy, matter or other relevant quantities for the system. Fluxes are related to dissipation and the emergence of coherent structures, which are known to enhance transport at macroscopic levels [69]. Fluxes represent one of the most essential manifestation of NED, and their relation to entropy production is already suggested in the pioneering work of Onsager [70]. The transport of energy toward the small scales in the turbulent cascade is a clear indicator of the out-of-equilibrium nature of turbulence.

1.4.4 Entropy and reproducibility: is there a non-equilibrium 'second principle'?

Natural phenomena are reproducible. The same experimental set-up leads to the same macroscopic results. Although evident for any empirical observer, it is far from obvious that the evolution of complex systems should always lead to the same macroscopic

observables.

The set of rules that govern complex systems are usually simple: conservation of mass, conservation of momentum, conservation of electric charge, etc., and these rules operate over an arbitrarily large number of degrees of freedom, allowing for an inconceivably large number of possible states and evolutions consistent with the dynamics.

Despite the lack of dynamical constrains, complex systems out of equilibrium reproduce the same identifiable, organised macroscopic structure. Any human observer is able to recognise this structure in many natural phenomena such as clouds, bonfires or, perhaps, the anatomy of many living beings. These organised evolutions represent probably only a negligible part of all possible evolutions consistent with the governing laws and the boundary conditions, and it is natural to ask what characteristics make these evolutions more probable.

In equilibrium statistical mechanics, the second law is used to rule out all possible states whose entropy is not maximum. A confined gas in equilibrium is always homogeneously distributed in its container, although many other macroscopic states are also possible. The principle of maximum entropy is necessary to justify the recurrent observation of this state, i.e it is necessary to explain reproducibility.

Reproducibility in NED also suggests that it is necessary to invoke universal statistical principles to explain the recurrent behaviour of out-of-equilibrium systems [71]. These statistical principles would rule the selection of a reduced number of out-of-equilibrium coherent and self-organised states from a much larger set of decorrelated incoherent states. In the spirit of the second law of thermodynamics, many researchers have proposed equivalent extremal principles for NED based on entropy production, such as the law of minimum entropy production [72] or its opposite, the law of maximum entropy production [73]. These principles have been tested in diverse systems out of equilibrium with contradictory results, which surrounds the subject with significant controversy. We must consider that these probabilistic principles, if they exist, might not be variational, i.e. emanate from the maximisation of functional, or, if they were variational, they might not necessary imply the maximisation or minimisation of a particular definition of entropy production.

It can be argued that, in a deterministic universe, the laws of physics univocally determine the future state of any system, and a statistical principle for the selection of future states is not necessary. However chaos imposes essential restrictions on the knowledge of the future. It is not that we choose to disregard relevant information about the system, but that we are forced to: it is intrinsically impossible to capture all the necessary information to reconstruct the detailed evolution of chaotic dynamics.

The chaotic nature of complex systems opposes the extended idea of 'strict' determinism, by which the deterministic laws of physics are enough to predict the observable natural phenomena. This idea can be disproved with a simple thought experiments using reversible dissipative dynamical systems [74], which reproduce the behaviour of dissipative systems but are invariants under a change in the time axis, $t \to -t$. As argued by Loschmidt [75], time reversibility implies that for each direct evolution there exists a corresponding inverse evolution. However these systems always evolve in a well-defined direction in time, leading to an apparent paradox. The introduction of entropy, a probabilistic concept, is necessary to justify the selection of direct evolutions over inverse evolutions Evans and Searles [76], proving that further assumptions, beyond the purely deterministic laws of motion, are necessary to explain the evolution of complex systems.

1.5 Scope and organisation of this thesis

Energy flows in the turbulence energy cascade, on average, from the large to the small scales, but hardly ever the opposite way. This behaviour is not directly encoded in the NS equations but results from the complex and chaotic behaviour of turbulent flows. The goal of this thesis is to understand the origin of the 'arrow of time' in the energy cascade by analysing the physical mechanisms that determine the prevalence of direct over inverse cascades.

This thesis is organised as follows. In chapter 2, we explore microscopic reversibility in the inertial scales of turbulence, and justify statistical irreversibility using two complementary definitions of entropy. In chapter 3 we present numerical experiments on reversible turbulence, and characterise the distribution of inverse cascades in phase space. We explain the preferential direction of the energy cascade by studying the local structure of the energy fluxes in physical space, which reveal the space locality of the

energy cascade. In chapter 4, we compare the structure of the direct and inverse energy cascades using the invariants of the velocity gradient tensor, which allow us to determine the mechanisms responsible for inverse and direct energy transfer. In view of these results, we provide arguments to justify the negligible probability of inverse cascades. Finally, in chapter 5, we study the chaotic structure of the energy cascade, which we relate with entropy production, and identify the mechanisms leading to the generation of chaos and entropy in physical space. A summary of the findings of this thesis and a final discussion are offered in chapter 6.

Chapter 2

Entropy production and irreversibility in the energy cascade

The powerful concept of entropy was originally coined by Clasius in the 1850s to refer to the energy transformed by dissipation and friction, and that could not be used to generate mechanical work. Since then, entropy has become perhaps one of the most complex and widely used concepts in science, with applications spanning diverse fields such as telecommunications, biology, or social sciences. Throughout this work, we will use the term entropy in the context of non-equilibrium phenomena to justify the 'arrow of time', i.e, the empirical evidence that complex systems tend to evolve in a particular direction in time, but not in its opposite.

The concept of entropy is extremely relevant because, as exposed in the example of reversible dissipative systems, the 'arrow of time' is not imposed by the fundamental laws of Newtonian mechanics that govern nature [77]. The naked eye recognises 'direct' processes as natural, for instance, the mixing of ink in water, while the same processes played backwards appear completely unnatural to us. However, both the 'direct' and 'inverse' processes are fully compatible with the laws that describe these phenomena. The question is then obvious: why should we expect complex systems always to evolve in the same direction?

Entropy can be naively defined as a quantity whose evolution distinguishes between the 'direct' and 'inverse' processes. Thus defined, entropy seems intuitive but useless. Unfortunately, the available definitions of entropy for non-equilibrium systems are not useful either: they cannot be easily measured, or they are inconsistent with the equilibrium formalism.

Here we present two complementary definitions of entropy that explain the 'arrow of time' in the turbulence energy cascade. Both definitions are incomplete and do not take into account the fundamental aspects of turbulence dynamics, but offer a fair explanation for the prevalence of direct cascades.

2.1 Microscopic reversibility in the turbulent energy cascade

Turbulence is a highly dissipative and essentially irreversible phenomenon. An intrinsic source of irreversibility appears in the NS equations in the form of viscosity, which accounts for the molecular diffusion of momentum. However at high Reynolds number only the smallest scales, where the local Reynolds number is low, are affected by viscosity. At scales much larger than the Kolmogorov length, viscous effects are negligible and dynamics are driven by inertial forces, which generate time-reversible dynamics. This is clear for the truncated Euler equations, which are known to be time-reversible, and to display features specific to fully developed turbulent flows under certain conditions [64, 65]. Although these equations show invariance under a change in the time axis, statistical irreversibility appears as a pronounced tendency towards preferential evolutions when the system is driven out of equilibrium, being the preferential direction of the energy cascade an important manifestation of this irreversibility. Other evidences of statistical irreversibility in turbulent flows are found in the Lagrangian evolution of perfect tracers [78, 79], or in the structure of the velocity gradients in the inertial range [80].

Intrinsic irreversibility is directly imposed in the equations of motion, e.g molecular diffusion of momentum, while statistical irreversibility is a consequence of the dynamical complexity of highly chaotic systems with many degrees of freedom. In the absence of an intrinsic irreversible mechanism, a dynamical system can be microscopically reversible

and statistically irreversible. This idea, which is widely understood in the study of dynamical systems, has not been sufficiently investigated in the context of the turbulent cascade.

The concept of microscopically reversible turbulence has been already treated in the literature. Gallavotti [81] proposed a reversible formulation of dissipation in an attempt to apply the theory of hyperbolic dynamical systems to turbulence and study fluctuations out of equilibrium. This idea was later applied by Biferale et al. [82] to construct a reversible shell-model of the turbulent cascade to study the system under weak departures from equilibrium. Rondoni and Segre [83] and Gallavotti et al. [84] further extended reversible models to 2D turbulence, proving that reversible dissipative systems can properly represent some aspects of the dynamics of turbulence. Reversibility is also present in some common large eddy simulation (LES) models, which reproduce the odd symmetry of energy fluxes with velocities, yielding fully reversible representations of the sub-grid stresses [85–87].

Despite the statistical irreversibility of the energy cascade, previous investigations show that it is possible to reverse turbulence in time. Carati et al. [88] constructed a reversible turbulent system using a standard dynamic Smagorinsky model for the sub-grid stresses and removing molecular viscosity. When reversed in time after decayed for a while, this system recovers all its lost energy and other turbulent quantities. In the time-backwards evolution, this reversible turbulent system develops a sustained inverse energy cascade towards the large scales.

We will show empirical evidence that spontaneously observing an inverse cascade in this system is extremely unlikely, yet this experiment shows that inverse cascades are possible, exposing the entropic nature of the energy cascade. The direct cascade is not directly enforced by the dynamics but is simply more probable.

2.2 Entropy production as phase-space mixing

Let us consider a dynamical system of n number of degrees of freedom representing turbulence. Each state of the system is represented by an n-dimensional state vector,

$\boldsymbol{\chi} = (\chi_1, \chi_2, \ldots, \chi_n)$. The evolution of $\boldsymbol{\chi}$ is described by a generic equation of the form

$$\frac{\mathrm{d}\boldsymbol{\chi}}{\mathrm{d}t} = \boldsymbol{F}(\boldsymbol{\chi}), \tag{2.1}$$

where, for simplicity, $\boldsymbol{F}$ is assumed to depend only on $\boldsymbol{\chi}$. All possible states of the system are represented in a n-dimensional phase space, where each unique state, $\boldsymbol{\chi}$, is described by a point and, its evolution, by a deterministic trajectory.

Let us consider a definition of entropy related to the theory of dynamical systems. Assuming that this system satisfies a Liouville conservation equation, i.e. the dynamics preserve the infinitesimal phase-space volume, we partition the accessible phase space in $\gamma = 1, 2, \ldots, m$ coarse-grained subsets of volume ω_γ. Let $P(\boldsymbol{\chi})$ be the probability density of the state $\boldsymbol{\chi}$. The probability of finding a state in a subset γ is

$$P_\gamma = \int_{\omega_\gamma} P(\boldsymbol{\chi})\, \mathrm{d}\boldsymbol{\chi}, \tag{2.2}$$

where the integral is taken over ω_γ. We define the information coarse-grained entropy as

$$H = -\sum_\gamma P_\gamma \log\left(P_\gamma \frac{\Upsilon}{\omega_\gamma}\right), \tag{2.3}$$

where $\Upsilon = \sum_\gamma \omega_\gamma$, and the summation is done over all the sub-volumes γ of the partition. This entropy is maximised at the equilibrium distribution of conservative systems with mixing chaotic dynamics, for which the coarse-grained probability distribution is $P_\gamma/\omega_\gamma = \text{const}$. Although (2.3) changes with the geometrical properties of the partition, such as the volume of the subsets, and can only be defined up to a constant, it is always maximised at the equilibrium distribution. Entropy can be connected with the information theory, such that the information on the state of an ensemble of realisations is proportional to minus the entropy [89].

Let us consider the Euler equations projected on a truncated Fourier basis, for which a conservation Liouville equation holds for the Fourier coefficients in a canonical form [90, 91], and an initial ensemble of states far from equilibrium, such as all the velocity fields with a fixed initial Kolmogorov energy spectrum ($k^{-5/3}$, where k is the wavenumber magnitude) and a fixed total kinetic energy. Initially, H has a low value because the distribution is localised in special subsets of phase space. As the ensemble evolves,

the probability density is conserved along each trajectory, $P(\boldsymbol{\chi}(t)) = P(\boldsymbol{\chi}(0))$, and entropy production appears as a chaotic 'mixing' process in which the initial distribution spreads across the accessible phase space, exploring all possible states consistent with the dynamics. Since the Euler equations have only one non-negative invariant of motion, the total kinetic energy, the accessible phase space corresponds to all states with the same total kinetic energy. After some time, the initial distribution is sufficiently mixed that the average probability over each element of the partition tends to $P_\gamma/\omega_\gamma = \text{const}$, which maximises (2.3). In this mixing process, H increases with time until the absolute equilibrium is accomplished.

In Fourier space, absolute equilibrium is represented by an uniform distribution of intensities across all modes (white noise or k^2 spectrum), which stands as the most probable macroscopic state, i.e. the macroscopic state that is represented by the largest number of microscopic realisations. The final equilibrium distribution has more energy in the small scales than the initial out-of-equilibrium distribution. Since in equilibrium energy is uniformly distributed among all modes, this is a consequence of the small scales being represented by a much larger number of deegres of freedom than the large scales. The energy flux towards the small scales and entropy production appear as equivalent representations of the same phenomena, namely the drift of the system towards equilibrium.

An out-of-equilibrium steady states can conceptually imposed by fixing the boundary conditions of the system in phase space. The energy cascade appears as the attempt of the system to reach equilibrium, but this final state is never achieved because the boundary conditions sustain the energy flux and maintain the system out of equilibrium. The definition of entropy in (2.3) is not useful in this case, as entropy production goes to zero in the steady state, but the work of [92] suggests a connection between entropy production, irreversibility and energy fluxes in conservative, boundary-driven systems .

In summary, entropy production and the energy cascade arise in an out-of-equilibrium ensemble of the truncated Euler equations as the consequence of four aspects of inertial dynamics. First, the conservation of phase-space probabilities along trajectories due to Liouville; second, the strong mixing nature of turbulent dynamics in the inertial range; third, the fact that small scales are represented by a much larger number of degrees of freedom than the large scales. Finally, we must also consider that inertial dynamics only conserve one non-negative invariant, the total kinetic energy, which implies that

the probability distribution is mixed in the constant energy sub-space, leading to the equipartition of energy. This is not the case in other chaotic dynamical systems satisfying a Liouville probability-conservation equation, such as the inviscid 2D turbulence [93], or some projections of the Euler equations [47], which have absolute equilibrium spectra different from the equipartition of energy. As opposed to the truncated Euler, in these systems an inverse cascade of energy appears as a process consistent with the evolution of the system towards equilibrium.

In this context, the inverse cascade appears intuitively unlikely, as it implies the concentration of the probability distribution in a set of reduced states that have most energy in the large scales. This is equivalent to the spontaneous organisation of independent small eddies into a large coherent structure. This behaviour is inconsistent with the chaotic nature of the cascade, which results in the spreading of the phase-space probability distribution.

2.3 Entropy production as phase-space volume contraction

The previous example describes the energy cascade as the evolution of a conservative system towards equilibrium. However, the NS equations are not conservative but dissipative. Dissipation implies that phase space volume is continuously contracted and, in the steady state, the probability distribution converges to an attractor of dimension lower than that of phase space.

In this case, the coarse-grained entropy reaches a steady value and $d_t H = 0$, contradicting the intuitive notion that the production of entropy should be positive for dynamical systems out of equilibrium. This inconsistency, which stems from the coarse-graining of phase space, is bypassed by arguing that the internal irreversible entropy production, $d_t H_i$, is balanced with the entropy flux to the environment due to the dissipative field, $d_t H_f$, so that the evolution of the total entropy reads $d_t H = d_t H_i + d_t H_f = 0$ [94]. The second term in the right-hand side is usually related to the phase-space volume contraction rate, although the exact relation of both terms with the evolution of the phase-space probability distribution is not straightforward.

Entropy production has also been related to phase-space volume contraction in the formalism of the fluctuation relations (FR), which constitutes, perhaps, the closest approach to a 'second law' for dynamical systems out of equilibrium.

The FR have received special attention since they quantitatively predict macroscopic irreversibility in microscopically reversible dissipative systems. The original FR by Evans et al. [95] express the probability of observing negative fluctuations of the time-averaged dissipation function, such that

$$\frac{P(\langle\Omega\rangle_t = \quad A)}{P(\langle\Omega\rangle_t = -A)} = \exp(At), \tag{2.4}$$

where $\langle\cdot\rangle_t$ stands for the temporal average over a phase-space trajectory of duration t, Ω is the dissipation function, an extensive state variable related to entropy production, and A is a prescribed valued of $\langle\Omega\rangle_t$. The dissipation function in a state $\boldsymbol{\chi}$ is defined as the instantaneous rate of phase-space volume contraction,

$$\Omega = \sum_{i=1}^{n} \frac{\partial F_i(\boldsymbol{\chi})}{\partial \chi_i}, \tag{2.5}$$

which is usually interpreted as the entropy exported out of the system [96]. Direct trajectories are those in which phase-space volume is contracted, while inverse trajectories imply the expansion of phase-space volume. According to the FR, the probability of inverse phase-space trajectories decays exponentially with the integration time, and with the size of the system through the extensivity of Ω. In the case of the turbulent system of Carati et al. [88], a positive sign of Ω is related to direct energy transfer towards the unresolved scales, and the FR justifies the overwhelming probability of direct cascades.

Although volume contraction plays an important role in the evolution of the phase-space probability distribution, we argue that, due to the conservative properties of the inertial range, which preserves phase-space volume, phase-space mixing is the fundamental source of irreversibility in the cascade. At high Reynolds number the dynamics of the inertial range should be independent of the presence of non-conservative forces in the large and small scales, and locally resemble that of a conservative, volume-preserving system out of equilibrium. The exact structure of the dissipative field in the small scales, which is responsible for phase-space volume contraction, should not be relevant for the inertial dynamics. This idea becomes evident in the study of hyperviscous turbulence by

Borue and Orszag [45], or in the work of She and Jackson [64] and Cichowlas et al. [65]. Their results show that the structure of the inertial range is universal, regardless of the nature of the dissipative mechanisms in the small scales.

This universality indicates that the phase-space structure of the probability distribution of an Euler flow out of equilibrium, and the structure of the turbulent attractor in a steady state should share similar characteristics in the degrees of freedom representing the inertial scales. In the case of the truncated Euler equations only phase-space mixing is present as an entropy source, which suggests that this is the essential entropy-production mechanism of the cascade. In the present frame, the energy cascade is analysed as a boundary-driven conservative system, for which entropy production is directly connected to phase-space mixing.

2.4 From phase space to physical space: what are the entropy-production mechanisms of the cascade?

In this section, we have presented two approaches to justify the negligible probability of inverse cascades. Both approaches are statistical in nature, and are formulated in the frame of probability densities in phase space, disregarding the fundamental dynamics of the cascade. The original contribution of this work is to connect these approaches with the spatio-temporal structure of the turbulent cascade, and to explain irreversibility and entropy production in terms of measurable turbulent quantities and identifiable mechanisms in physical space.

This approach allows us to provide a description of irreversibility and entropy production in the energy cascade, first, by understanding the inertial mechanisms relevant to the cascade, and, second, by providing a probabilistic description that justifies why these mechanisms are more probable than the inverse mechanisms.

Chapter 3

Experiments on time-reversible turbulence

3.1 The reversible sub-grid model

A popular technique to alleviate the huge computational cost of simulating industrial turbulent flows is large-eddy simulation (LES), which filters out the flow scales below a prescribed cutoff length, and only retains the dynamics of the larger eddies. We use it here to generate microscopically reversible turbulence. The equations governing the large scales are obtained by filtering the incompressible NS equations,

$$\begin{aligned} \partial_t \overline{u}_i + \overline{u}_j \partial_j \overline{u}_i &= -\partial_i \overline{p} + \partial_j \tau_{ij}, \\ \partial_i \overline{u}_i &= 0, \end{aligned} \tag{3.1}$$

where the overline ($\overline{\cdot}$) represents filtering at the cutoff length $\overline{\Delta}$, u_i is the i-th component of the velocity vector $\boldsymbol{u} = (u_i)$, with $i = 1 \dots 3$, ∂_i is the partial derivative with respect to the i-th direction, p is a modified pressure, and repeated indices imply summation. We assume that the cutoff length is much larger than the viscous scale, and neglect in (3.1) the effect of viscosity on the resolved scales. The interaction of the scales below the cutoff filter with the resolved ones is represented by the sub-grid stress (SGS) tensor, $\tau_{ij} = \overline{u}_i \overline{u}_j - \overline{u_i u_j}$, which is unknown and must be modelled.

One of the consequences of this interaction is an energy flux towards or from the unresolved scales, which derives from triple products of the velocity field and its derivatives,

and is implicitly time-reversible. However, this flux is often modelled as a dissipative energy sink, destroying time reversibility and the possibility of inverse energy fluxes (backscatter). In an attempt to to yield a more realistic representation of the dynamics of the energy cascade, some SGS models try to reproduce backscatter, which also restores the time-reversibility of energy fluxes. This is the case for the family of dynamic models, which are designed to adapt the effect of the unresolved scales to the state of the resolved flow, eliminating tuning parameters. A widely used reversible model is the dynamic Smagorinsky model of Germano et al. [86], based upon the assumption that the cutoff filter lies within the self-similar inertial range of scales, and that the sub-grid stresses at the filter scale can be matched locally to those at a coarser test filter. This idea is applied to the classical Smagorinsky [97] model in which sub-grid stresses are assumed to be parallel to the rate-of-strain tensor of the resolved scales, $\overline{S}_{ij} = \frac{1}{2}(\partial_i \overline{u}_j + \partial_j \overline{u}_i)$, such that $\tau_{ij}^T \simeq 2\nu_s \overline{S}_{ij}$, where ν_s is referred to as the eddy viscosity, and the 'T' superscript refers to the traceless part of the tensor. Introducing $\overline{\Delta}$ and $|\overline{S}|$ as characteristic length and time scales, respectively, and a dimensionless scalar parameter C, the model is

$$\tau_{ij}^T = 2C\overline{\Delta}^2 |\overline{S}| \overline{S}_{ij}, \tag{3.2}$$

where $\nu_s = C\overline{\Delta}^2|\overline{S}|$, and $|S| = \sqrt{2S_{lm}S_{lm}}$. Filtering (3.1) with a test filter of width $\widetilde{\Delta} = 2\overline{\Delta}$, denoted by $(\widetilde{\cdot})$, we obtain expressions for the sub-grid stresses at both scales, which are matched to obtain an equation for C,

$$C\mathcal{M}_{ij} + \mathcal{L}_{ij}^T = 0, \tag{3.3}$$

where $\mathcal{M}_{ij} = \widetilde{\Delta}^2 |\widetilde{\overline{S}}| \widetilde{\overline{S}}_{ij} - \overline{\Delta}^2 \widetilde{|\overline{S}| \overline{S}_{ij}}$, and $\mathcal{L}_{ij} = \frac{1}{2}(\widetilde{\overline{u}_i \overline{u}_j} - \widetilde{\overline{u}}_i \widetilde{\overline{u}}_j)$. A spatially local least-square solution, C_ℓ, is obtained by contracting (3.3) with $\mathcal{M}_{ij}$,

$$C_\ell(\boldsymbol{x}, t; \overline{\Delta}) = \frac{\mathcal{L}_{ij}^T \mathcal{M}_{ij}}{\mathcal{M}_{ij}\mathcal{M}_{ij}}. \tag{3.4}$$

This formulation occasionally produces local negative dissipation, $C_\ell(\boldsymbol{x}, t) < 0$, which may lead to undesirable numerical instabilities [98, 99]. To avoid this problem, (3.3) is often spatially averaged after contraction to obtain a mean value for the dynamic parameter [100],

$$C_s(t; \overline{\Delta}) = \frac{\langle \mathcal{L}_{ij}^T \mathcal{M}_{ij} \rangle}{\langle \mathcal{M}_{ij}\mathcal{M}_{ij} \rangle}, \tag{3.5}$$

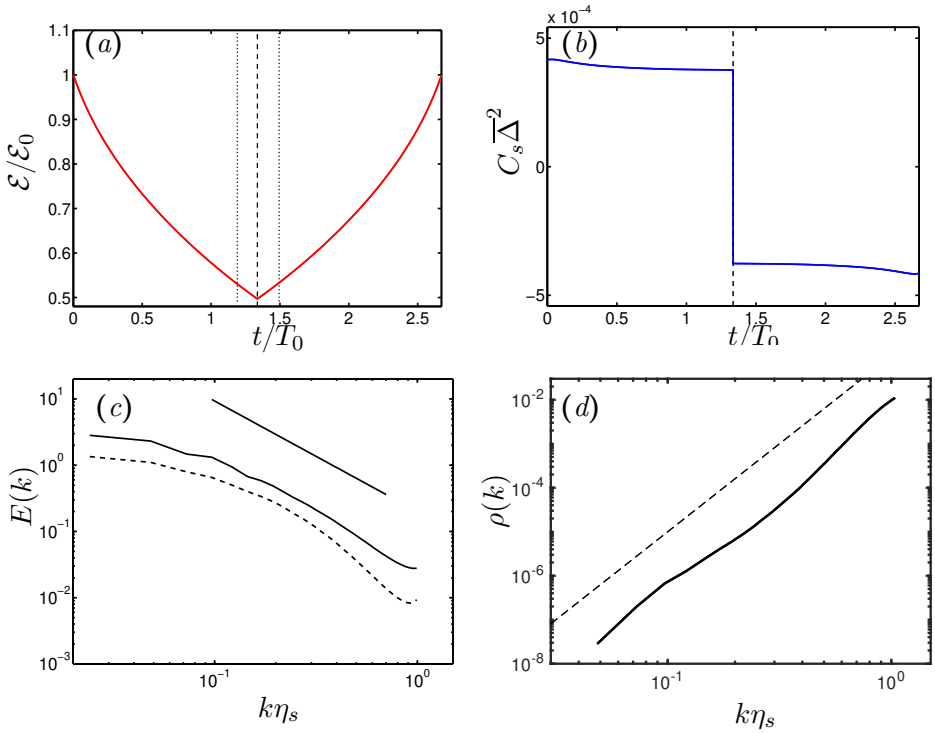

Figure 3.1: Evolution of: (*a*) mean kinetic energy, normalised with the initial energy $\mathcal{E}_0$, and (*b*) $C_s\overline{\Delta}^2$ as a function of time (arbitrary units). The dashed line in (*a*,*b*) is $t = t_{inv}$, and the dotted lines in (*a*) are $t = t_{stats}$, used in §4. (*c*) Energy spectrum $E(k)$. ——, $t = t_0$ and $t = 2t_{inv}$; – – –, $t = t_{inv}$. The diagonal line is $E(k) \propto k^{-5/3}$. (*d*) Spectrum of the error between the velocity fields at $t = 2t_{inv}$ and $t = t_0$, as a function of wavenumber. Dashed line denotes k^4.

where $\langle\cdot\rangle$ denotes spatial averaging over the computational box. A positive C_s implies that energy flows from the resolved to the unresolved scales, and defines a direct cascade. The sign of C_s depends on the velocity field through $\mathcal{M}_{ij}$, which is odd in the strain tensor, so that $C_s(-\boldsymbol{u}) = -C_s(\boldsymbol{u})$. Given a flow field with $C_s > 0$, a change in the sign of the velocities leads to another one with negative eddy viscosity.

This property allows us to construct a reversible turbulent system using the dynamic Smagorinsky model and removing molecular viscosity. The equations for the resolved velocity field, $\overline{\boldsymbol{u}}$, are

$$\begin{aligned} \partial_t u_i + u_j \partial_j u_i &= -\partial_i p + C_s \overline{\Delta}^2 \partial_j |S| S_{ij}, \\ \partial_i u_i &= 0, \end{aligned} \tag{3.6}$$

together with (3.5), where the filtering notation has been dropped for conciseness. The equations (3.6) are invariant to the transformation $t \to -t$ and $\boldsymbol{u} \to -\boldsymbol{u}$, and changing the sign of the velocities is equivalent to inverting the time axis.

3.2 Experiments on turbulence under time reversal

3.2.1 Numerical setup

A standard Rogallo [55] code is used to perform a series of experiments on decaying homogeneous turbulence in a $(2\pi)^3$ triply-periodic box. Equations (3.6) are solved with the dynamic Smagorinsky model described in the previous section. The three velocity components are projected on a Fourier basis, and the non-linear terms are calculated using a fully dealiased pseudo-spectral method with a 2/3 truncation rule [62]. We denote the wave-number vector by $\boldsymbol{k}$, and its magnitude by $k = |\boldsymbol{k}|$. The number of physical points in each direction before dealiasing is $N = 128$, so that the highest fully resolved wave number is $k_{max} = 42$. An explicit third-order Runge-Kutta is used for temporal integration, and the time step is adjusted to constant Courant-Friedrichs-Lewy number equal to 0.2, to keep numerical errors as low as possible. A Gaussian filter, whose Fourier expression is

$$G(k;\Delta) = \exp(-\Delta^2 k^2/24), \tag{3.7}$$

where Δ is the filter width [32], is used to evaluate C_s in (3.5). The equations are explicitly filtered at the cutoff filter $\overline{\Delta}$, and at the test filter $\widetilde{\Delta} = 2\overline{\Delta} = \Delta_g\sqrt{6}$, where $\Delta_g = 2\pi/N$ is the grid resolution before dealiasing. Although the explicit cutoff filter is not strictly necessary, it is used for consistency and numerical stability.

The energy spectrum is defined as

$$E(k;\boldsymbol{u}) = 2\pi k^2 \langle \widehat{u}_i \widehat{u}_i^* \rangle_k, \tag{3.8}$$

where $\widehat{u}_i(\boldsymbol{k})$ are the Fourier coefficients of the i-th velocity component, the asterisk is complex conjugation, and $\langle\cdot\rangle_k$ denotes averaging over shells of thickness $k \pm 0.5$. The kinetic energy per unit mass is $\mathcal{E} = \frac{1}{2}\langle u_i u_i \rangle = \sum_k E(k,t)$, where $\sum_k$ denotes summation over all wave-numbers.

Meaningful units are required to characterise the simulations. The standard reference for the small scales in Navier–Stokes turbulence are Kolmogorov units, but they are not applicable here because of the absence of molecular viscosity. Instead we derive pseudo-Kolmogorov units using the mean eddy viscosity, $\langle \nu_s \rangle = C_s \overline{\Delta}^2 \langle |S| \rangle$, and the mean sub-grid energy transfer at the cutoff scale, $\langle \epsilon_s \rangle = C_s \overline{\Delta}^2 \langle |S|^3 \rangle$. The time and length scale

derived from these quantities are $t_s = (\langle \nu_s \rangle / \langle \epsilon_s \rangle)^{1/2}$ and $\eta_s = (\langle \nu \rangle_s^3 / \langle \epsilon_s \rangle)^{1/4}$, respectively. We find these units to be consistent with the physics of turbulence, such that the peak of the enstrophy spectrum, $k^2 E(k)$, is located at approximately $25\eta_s$. In DNSs, this peak lies at approximately 20η.

The larger eddies are characterised by the integral length and velocity scales [101], respectively defined as

$$L = \pi \frac{\sum_k E(k,t)/k}{\sum_k E(k,t)}, \tag{3.9}$$

and $U = \sqrt{2\mathcal{E}/3}$. The Reynolds number based on the integral scale is defined as $Re_L = UL/\langle \nu_s \rangle$, and the separation of scales in the simulation is represented by the ratio L/η_s.

In the following we study the energy flux both in Fourier space, averaged over the computational box, and locally in physical space.

The energy flux across the surface of a sphere in Fourier space with wave-number magnitude k can be expressed as

$$\Pi(k) = \sum_{q<k} 4\pi q^2 \mathrm{Re} \langle \widehat{u}_i^*(\boldsymbol{q}) \widehat{B}_i(\boldsymbol{q}) \rangle_q, \tag{3.10}$$

where $B_i = u_j \partial_j u_i - \partial_i p$, and a negative Π denotes energy flowing to larger scales.

We use two different definitions of the local inter-scale energy flux in physical space,

$$\begin{aligned} \Sigma(\boldsymbol{x}, t; \Delta) &= \tau_{ij} S_{ij}, \\ \Psi(\boldsymbol{x}, t; \Delta) &= -u_i \partial_j \tau_{ij}, \end{aligned} \tag{3.11}$$

where the velocity field, the rate-of-strain tensor, and τ_{ij} are filtered with (3.7) at scale Δ. Both are standard quantities in the analysis of the turbulence cascade [17, 29, 30, 32], and are related by $\Psi = \Sigma - \partial_j(u_i \tau_{ij})$. The second term in the right-hand side of this relation is the divergence of an energy flux in physical space, which has zero mean over the computational box, so that $\langle \Sigma \rangle = \langle \Psi \rangle$. Positive values of Σ and Ψ indicate that the energy is transferred towards the small scales.

Because the decaying system under study is statistically unsteady, averaging over an ensemble of many realisations is required to extract time-dependent statistics. This is generated using the following procedure. All the flow fields in the ensemble share an initial energy spectrum, derived from a forced statistically-stationary simulation, and an

	N	k_{max}	Re_L	$k_{max}\eta_s$	Δ_g/η_s	t_{inv}/T_0	L/η_s	L/Δ_g	$\epsilon_s L/U^3$	N_s
$t = t_0$	128	42	214	0.94	2.2	1.3	63.3	28.3	1.3	2000
$t = t_{inv}$			248	0.87	2.3		63.1	26.1	1.0	

Table 3.1: Main parameters of the simulation averaged over the complete ensemble at time t_0. See the text for definitions.

initial kinetic energy per unit mass. Each field is prepared by randomising the phases of $\widehat{u}_i$, respecting continuity, and integrated for a fixed time t_{start} up to the $t_0 = 0$, where a fully turbulent state is deemed to have been reached, the experiment begins, and statistics start to be compiled. The initial transient, t_{start}, common to all the elements in the ensemble, is chosen so that t_0 is beyond the time at which dissipation reaches its maximum, and the turbulent structure of the flow is fully developed. Following this procedure, we generate an ensemble of $N_s = 2000$ realisations, which are evolved on GPUs using a CUDA code developed during this thesis.

It is found that both the small- and large-scale reference quantities defined above vary little across an ensemble prepared in this way, with a standard deviation of the order of 5% with respect to their mean.

3.2.2 Turbulence with a reversible model

The basic experiment is conducted as in the paper by Carati et al. [88]. After preparing a turbulent field at $t = t_0 = 0$, the flow is evolved for a fixed time t_{inv}, during which some of the initial energy is exported by the model to the unresolved scales. The simulation is then stopped and the sign of the three components of velocity reversed, $\boldsymbol{u} \rightarrow -\boldsymbol{u}$. The new flow field is used as the initial condition for the second part of the run from t_{inv} to $2t_{inv}$, during which the flow evolves back to its original state, recovering its original energy and the value of other turbulent quantities.

It is found that η_s only changes by 5% during the decay of the flow, while t_s increases by a factor of 1.5 from t_0 to t_{inv}. On the other hand, the large-scale quantities, L and U vary substantially as the flow decays. The main parameters of the simulations, and the relation between large- and small-scale quantities, are given in table 3.1.

Figure 3.1(a, b) presents the evolution of the kinetic energy $\mathcal{E}$ and of C_s as a function of time for a representative experiment. We observe a clear symmetry with respect to

t_{inv} in both quantities, and we have checked that this symmetry also holds for other turbulent quantities, such as the sub-grid energy fluxes and the skewness of the velocity derivatives. Quantities that are odd with respect to the velocity display odd symmetry in time with respect to t_{inv}, and even quantities display even symmetry. In particular we expect $\boldsymbol{u}(2t_{inv}) \simeq -\boldsymbol{u}(t_0)$

Figure 3.1(c) shows the energy spectrum $E(k)$ at times t_0, t_{inv} and $2t_{inv}$. Although there are no observable differences between the initial and final spectra, we quantify this difference in scale using the spectrum of the error between the velocity field at t_0 and minus the velocity field at $2t_{inv}$,

$$\rho(k) = \frac{2E(k; \boldsymbol{u}(t_0) + \boldsymbol{u}(2t_{inv}))}{E(k; \boldsymbol{u}(t_0)) + E(k; \boldsymbol{u}(2t_{inv}))}, \tag{3.12}$$

which is presented in figure 3.1(d). The spectrum of the error is of the order of 0.01 in the cutoff wavenumber and decreases as k^4 with the wavenumber, confirming that the flow fields in the forward and backward evolution are similar, except for the opposite sign and minor differences in the small scales. This suggests that the energy cascade is microscopically reversible in the inertial scales. Sustained reverse cascades are possible in the system, even if only direct ones are observed in practice, suggesting that the one-directional turbulence cascade is an entropic (probabilistic) effect, unrelated to the presence of an energy sink at the small scales.

3.2.3 The reverse cascade without model

The validity of the conclusions in the previous section depends on the ability of the model system to represent turbulence dynamics. In particular, since the object of our study is the turbulence cascade rather than the SGS model, it is necessary to asses whether the reversibility properties of the system, and the presence of a sustained backwards energy cascade, stem from the SGS model, or whether intrinsic turbulent mechanisms are involved. In this subsection, we show that the model injects energy at the smallest resolved scales, but that that the energy travels back to the large scales due to inertial mechanisms. In the next subsection, we further demonstrate that the inverse cascade can exist for some time even for irreversible formulations of the dissipation.

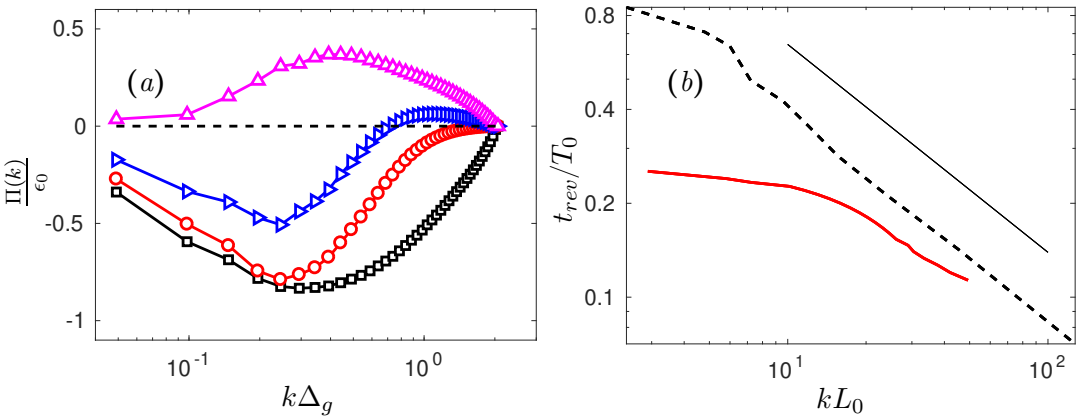

Figure 3.2: (a) Energy flux $\Pi(k)$ as a function of the time after removing the SGS model t/T_0: —□—, 0; —●—, 0.1; —▶—, 0.15; —▲—, 0.25. Energy flux normalised with $\epsilon_0 = {U_0}^3/L_0$. (b) Reversal time t_{rev}/T_0 at which $\Pi = 0$ as a function of wave-number kL_0. ———, Reversible SGS model ($N = 128$); – – –, irreversible spectral SGS model ($N = 512$). Solid black line $t_{rev}/T_0 \propto {kL_0}^{-2/3}$.

If the SGS model contributed substantially to the presence of a sustained inverse cascade, the removal of the model during the backward leg of the simulation would have an immediate effect on the system, resulting in the instantaneous breakdown of the reverse cascade. This is shown not to be the case by an experiment in which the model is removed at t_{inv} by letting $C_s = 0$. The system then evolves according to the Euler equations

$$\begin{aligned} \partial_t u_i + u_j \partial_j u_i &= -\partial_i p, \\ \partial_i u_i &= 0, \end{aligned} \tag{3.13}$$

which are conservative and include only inertial forces. The resulting evolution of the inertial energy flux across Fourier scales, $\Pi(k,t)$, defined in (3.10), is displayed in figure 3.2(a) as a function of wavenumber and time.

At t_{inv}, energy fluxes are negative at all scales and energy flows towards the large scales. Shortly after, at $t - t_{inv} = 0.1T_0$, the inverse cascade begins to break down at the small scales, while it continues to flow backwards across most wavenumbers. This continues to be true at $t = 0.15T_0$, where the direct cascade at the smallest scales coexists with a reverse one at the larger ones. The wavenumber separating the two regimes moves progressively towards larger scales, and the whole cascade become direct after $t \simeq 0.25T_0$. Figure 3.2(b) shows the dependence on the wavenumber of the time $t_{rev}(k)$ at which $\Pi(k, t_{rev}) = 0$. It is significant that, for wavenumbers that can be considered inertial, $kL_0 \gg 1$, it follows $t_{rev}/T_0 \sim (kL_0)^{-2/3}$, which is consistent with the Kolmogorov [9]

self-similar structure of the cascade. Cardesa et al. [17] found a similar trend in the propagation of energy-transfer fluctuations across the inertial range.

The simplest conclusion is that the model just acts as a source to provide the small scales with energy as they are being depleted by the flux towards larger eddies. If this source is missing, the predominant forward cascade reappears, but the inertial mechanisms are able to maintain the reverse cascade process as long as energy is available.

3.2.4 The effect of irreversible models

We have repeated the same experiment for an irreversible spectral SGS model [102] with a higher resolution ($N = 512$). Results of $t_{rev}(k)$ for this experiment are shown by the dashed line in figure 3.2(b). The behaviour is similar to the experiment in the previous section, but the wider separation of scales in this simulation allows the preservation of an inverse cascade for times of the order of the integral time. This experiment confirms that the microscopic reversibility of the inertial scales is independent of the type of dissipation, and holds as long as the information of the direct cascade process is not destroyed by the LES model. This experiment suggests that microscopic reversibility should also hold in the inertial range of fully developed NS turbulence.

3.3 Phase- and physical-space characterisation of the energy cascade

3.3.1 The geometry of phase space

In the first place we confirm, by perturbing the inverse cascade, that in the neighbourhood of each inverse evolution there exist a dense distribution of phase-space trajectories that also display inverse dynamics. Each inverse trajectory is 'unstable', in the sense that it is eventually destroyed when perturbed, but inverse dynamics are easily found considerably far from the original phase-space trajectories, even for distances of the order of the size of the accessible phase space, suggesting that inverse and direct trajectories lie in separated regions of phase space, rather than mostly being intertwined in the same neighbourhood.

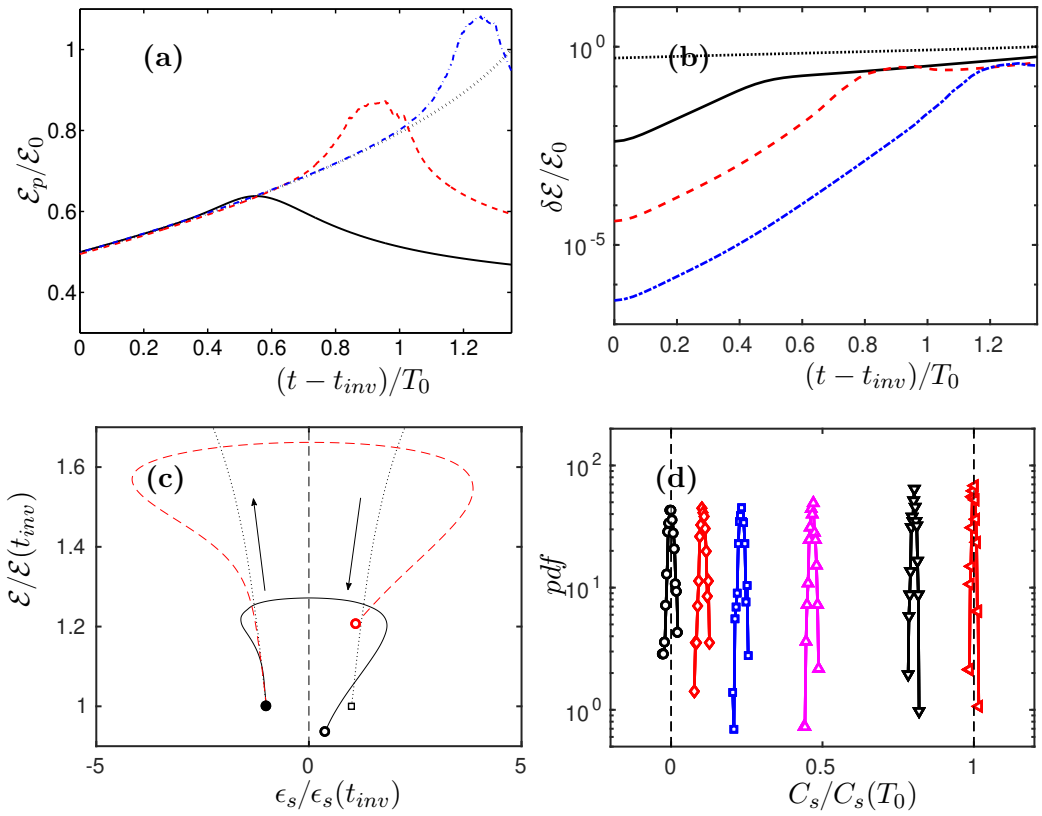

Figure 3.3: (a) Evolution of the energy of the perturbed fields $\mathcal{E}_p$ and (b) of $\delta\mathcal{E} = 1/2\langle\delta\boldsymbol{u}^2\rangle$, normalised with $\mathcal{E}_0$, for: ———, 0.1; – – –, $\mu = 0.01$; – · – ·, $\mu = 0.001$; ·····, energy of the unperturbed trajectory, $\mathcal{E}/\mathcal{E}_0$. (c) Perturbed trajectories for $\mu = 0.1$ and $\mu = 0.01$, represented in the energy-dissipation space. Symbols as in (a). The solid circle represents the beginning of the inverse trajectory at t_{inv}, the empty circles the end of the perturbed trajectories at $2t_{inv}$, and the solid square the end of the direct trajectory at time t_{inv}. The dotted lines and the arrows represent the direct (right) and the inverse (left) trajectories. (d) Evolution of the probability density function of C_s as a function of time starting from random initial conditions at t_{start}. From left to right: $(t - t_{start})/T_0$=: 0.0; 0.008; 0.017; 0.033; 0.067; 1.0. C_s normalised with the ensemble average at T_0.

In this experiment we generate a backward initial condition by integrating the equations of motion until t_{inv}, changing the sign of the velocities $\boldsymbol{u}^\iota = -\boldsymbol{u}(t_{inv})$, and introducing a perturbation, $\delta\boldsymbol{u}$. The perturbed flow field, $\boldsymbol{u}^p = \boldsymbol{u}^\iota + \delta\boldsymbol{u}$, is evolved and compared to the unperturbed trajectory, $\boldsymbol{u}^\iota(t)$. We choose the initial perturbation field in Fourier space as,

$$\delta\widehat{u}_i(\boldsymbol{k}) = \widehat{u}_i^\iota(\boldsymbol{k}) \cdot \mu \exp(\mathrm{i}\phi), \tag{3.14}$$

where ϕ is a random angle with uniform distribution between 0 and 2π and μ is a real parameter that sets the initial energy of the perturbation. The same ϕ is used for the three velocity components, so that incompressibility also holds for $\boldsymbol{u}^p$.

Figures 3.3(a,b) show the evolution of the mean kinetic energy of the perturbed field, $\mathcal{E}_p = \frac{1}{2}\langle(\boldsymbol{u}^p)^2\rangle$, and of the perturbation field, $\delta\mathcal{E} = \frac{1}{2}\langle\delta\boldsymbol{u}^2\rangle$, for $\mu = 0.1$, 0.01 and 0.001. The energy of the perturbed fields increases for a considerable time in the three cases, demonstrating the presence of inverse energy transfer and negative mean eddy-viscosity, $C_s < 0$. Even under the strongest initial perturbation, $\mu = 0.1$, the inverse cascade is sustained for approximately $0.5T_0$. As shown in figure 3.3(b), by the time the inverse cascade is destroyed and the energy of the perturbed fields has evolved to a maximum and $C_s = 0$, the energy of the perturbation is comparable to the total energy in all cases, $\delta\mathcal{E} \sim \mathcal{E}$, which indicates that the states that separate inverse and direct dynamics are considerably far in phase space from the unperturbed trajectories.

If we estimate distances as the square-root of the energy (L_2 norm of the velocity field), the maximum of $\mathcal{E}_p$ is located approximately at $\delta\mathcal{E}^{1/2} \simeq 0.4\mathcal{E}_0^{1/2}$ from the unperturbed phase-space trajectory. In figure 3.3(c) we represent the evolution of the perturbed trajectories in the dissipation-energy space. This plot intuitively shows that a typical direct trajectory is located far apart in phase space from inverse trajectories, and that perturbed inverse trajectories must first cross the set of states with zero dissipation, $C_s = 0$, before developing a direct cascade.

In figure 3.3(d) we show the evolution of the probability density function of C_s in the direct evolution of the ensemble, starting at t_{start}, when the initial condition is a random field with prescribed energy spectrum. The initial probability distribution of C_s is symmetric and has zero mean, because the probabilities of direct and inverse evolutions are similar. As the system evolves in time towards the turbulent attractor, the probability of finding a negative value of C_s decreases drastically. At $t - t_{start} = 0.008T_0$, we do not observe any negative values of C_s in the ensemble. The standard deviation of C_s is small compared to the mean at $t - t_{start} = T_0$, which indicates the negligible probability of observing negative values of C_s after a time of the order of an eddy-turnover time.

Inverse evolutions sustained in time are almost only accessible from forward-evolved flow fields with changed sign. These trajectories lie in the antiattractor, which is constructed by applying the transformation $u \to -u$ to the turbulent attractor. However, we have shown in this analysis that inverse trajectories exist in a larger set of states outside the antiattractor, which can be escaped by perturbing the reversed flow fields. The destruction of the inverse cascade under perturbations, and the small standard deviation

of C_s in the turbulent attractor, reflect the negligible probability of inverse evolutions, and indicate that they can only be accessed temporarily.

The reversible turbulent system under study provides access to trajectories outside the turbulence attractor, which is characterised almost exclusively by direct cascades. These trajectories allow us to study the physical mechanisms by which direct energy transfer prevails over inverse energy transfer.

3.3.2 The structure of local energy fluxes in physical space

Up to now we have only dealt with the mean transfer of energy over the complete domain. In this section we characterise the energy cascade as a local process in physical space. We study here two markers of local energy transfer in physical space, $\Sigma(\boldsymbol{x}, t; \Delta)$ and $\Psi(\boldsymbol{x}, t; \Delta)$, previously defined in (3.11), calculated at filter scales $\Delta = 5\Delta_g$ and $\Delta = 10\Delta_g$. Figures 3.4(a,b) show the probability distribution of these quantities in the direct evolution. We observe wide tails in the probability distribution of the two quantities, and skewness towards positive events, which is more pronounced for Σ than for Ψ. Energy fluxes change sign under $\boldsymbol{u} \to -\boldsymbol{u}$, and, as shown in figure 3.4, their odd-order moments are in general non-zero and have a definite sign in turbulent flows. This sign denotes statistical irreversibility, i.e, the privileged temporal direction of the system in an out-of-equilibrium evolution. The spatial average, which marks the direction of the cascade, is an important example, $\langle\Sigma\rangle = \langle\Psi\rangle > 0$.

To characterise the non-local spatial properties of the local energy fluxes, we define the correlation coefficient between two scalar fields, ψ and ζ, as

$$\mathcal{S}_{\psi,\zeta}(\Delta\boldsymbol{x}) = \frac{\langle\psi'(\boldsymbol{x}+\Delta\boldsymbol{x})\zeta'(\boldsymbol{x})\rangle}{\sqrt{\langle\psi'^2\rangle\langle\zeta'^2\rangle}}, \tag{3.15}$$

where we subtract the spatial average from quantities marked with primes. Due to isotropy, $\mathcal{S}$ only depends on the spatial distance, $\Delta x = |\Delta\boldsymbol{x}|$. We also define the auto-correlation coefficient $\mathcal{S}_{\psi,\psi}(\Delta x)$ and the auto-correlation length as

$$\ell_\psi = \int_0^\infty \mathcal{S}_{\psi,\psi}(\xi)\,\mathrm{d}\xi, \tag{3.16}$$

	'All'	'+'	'−'		'All'	'+'	'−'
$\mathcal{R}_\Sigma(5\Delta_g, 10\Delta_g)$	0.74	0.73	0.2	$\mathcal{R}_\Sigma(5\Delta_g, 20\Delta_g)$	0.33	0.34	−0.01
$\mathcal{R}_\Psi(5\Delta_g, 10\Delta_g)$	0.70	0.60	0.4	$\mathcal{R}_\Psi(5\Delta_g, 20\Delta_g)$	0.24	0.29	−0.09

Table 3.2: Auto-correlation coefficient among scales of Σ and Ψ, evaluated for: 'All', the complete field; '+', conditioned to positive energy transfer events at $5\Delta_g$; '−', conditioned to negative energy transfer events at $5\Delta_g$.

which measures the typical length over which ψ decorrelates, and is related to the typical size of events in ψ. The correlation lengths of Σ and Ψ are proportional to the filter size Δ, $\ell_\Sigma \sim 0.47\Delta$ and $\ell_\Psi \sim 0.51\Delta$.

We use $\langle\Sigma\rangle_V$ and $\langle\Psi\rangle_V$ to study the spatial structure of energy fluxes, where $\langle\cdot\rangle_V$ represents the volume-averaging operation over a sphere of volume V. The standard deviation of the probability distribution of the volume-averaged fields,

$$\sigma_V = \sqrt{\langle\big(\langle\psi\rangle_V - \langle\psi\rangle\big)^2\rangle}, \tag{3.17}$$

is shown in figure 3.5(a) as a function of the averaging volume, where $\sigma_0 = (\langle\psi^2\rangle - \langle\psi\rangle^2)^{1/2}$ is the standard deviation of the test field without volume averaging. When the averaging volume is sufficiently large, $V/\ell^3 \gtrsim 10^3$, the standard deviation becomes inversely proportional to the square-root of $\mathcal{N} = V/\ell^3$ in all cases, where $\mathcal{N}$ is a measure of the number of independent energy transfer events within the averaging volume. These results suggest statistical independence of the events within the averaging volumes and, some degree of space locality in the energy cascade.

Despite this locality, the pointwise differences between Σ and Ψ might suggest that local energy fluxes cannot be uniquely defined, and that only global averages are robust with respect to the particular definition of fluxes, $\langle\Sigma\rangle = \langle\Psi\rangle$. The correlation between Σ and Ψ for $\Delta x = 0$ is low, $\mathcal{S}_{\Sigma,\Psi} \sim 0.05$, at both filter scales, $5\Delta_g$ and $10\Delta_g$. However, when these quantities are averaged, the correlation coefficient increases rapidly with the averaging volume. In figure 3.5(b), we show the dependence of $\mathcal{S}_{\langle\Sigma\rangle_V,\langle\Psi\rangle_V}$ on V. Henceforth we consider correlations without spatial offset, $\Delta x = 0$. For averaging volumes $V \sim (4\ell)^3$, the correlation increases to approximately 0.7 for both filter widths, indicating that Σ and Ψ are similar when averaged over volumes of the order of the their cubed correlation length.

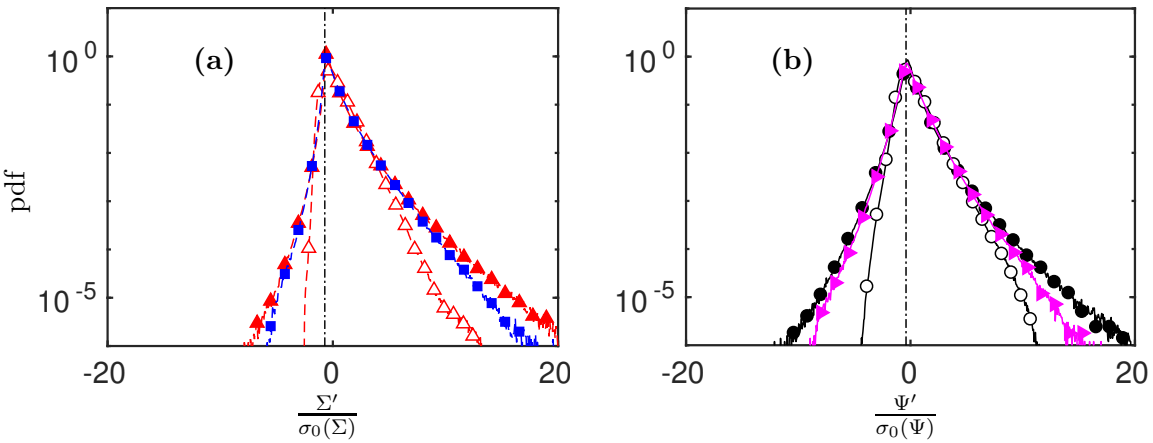

Figure 3.4: (a,b) Probability density function of local markers of the energy cascade without volume averaging: (a) Σ; (b) Ψ. Symbols in correspond to: - -▲- -, $\Sigma(5\Delta_g)$; - -■- -, $\Sigma(10\Delta_g)$; —▶—, $\Psi(5\Delta_g)$; —●—, $\Psi(10\Delta_g)$. The dashed-dotted lines represent $-\langle\psi\rangle/\sigma_V$ for quantities calculated at $5\Delta_g$, and the open symbols represent the probability density function of $\langle\Sigma(5\Delta_g)\rangle_V$ and $\langle\Psi(5\Delta_g)\rangle_V$ for $V = (16\Delta_g)^3$.

3.3.3 The structure of local energy fluxes in scale space

We extend this analysis to scale space by considering the correlation of the energy fluxes at different scales, defined as

$$\mathcal{R}_\psi(\Delta_1, \Delta_2) = \frac{\langle \psi'(\boldsymbol{x}; \Delta_1)\psi'(\boldsymbol{x}; \Delta_2)\rangle}{\sqrt{\langle(\psi'(\Delta_1))^2\rangle\langle(\psi'(\Delta_2))^2\rangle}}. \tag{3.18}$$

We also calculate the same quantity conditioning the averages to positive or negative energy transfer events at scale Δ_1. We denote the conditional correlations by $\mathcal{R}^+$ when conditioning to $\psi(\Delta_1) > 0$, and $\mathcal{R}^-$ when conditioning to $\psi(\Delta_1) < 0$. The values of these interscale auto-correlation coefficients are presented in table 3.2. We find correlation values of approximately 0.7 for scale increments of 2 in both quantities. In this analysis we have also included scale $20\Delta_g$ to show that energy fluxes decorrelate substantially when their scales differ by a factor of 4, $\mathcal{R}(5\Delta_g, 20\Delta_g) \sim 0.3$. These values remain similar when conditioning to positive energy transfer events, but are reduced substantially in all cases when conditioning to local backscatter.

In figure 3.5(c), we show the dependence of $\mathcal{R}_{\langle\Sigma\rangle_V}(5\Delta_g, 10\Delta_g)$ and $\mathcal{R}_{\langle\Psi\rangle_V}(5\Delta_g, 10\Delta_g)$ with the averaging volume V. The interscale auto-correlation increases with the averaging volume when we consider all events and direct energy transfer events (not shown). On the other hand, the interscale auto-correlation of the averaged fluxes conditioned

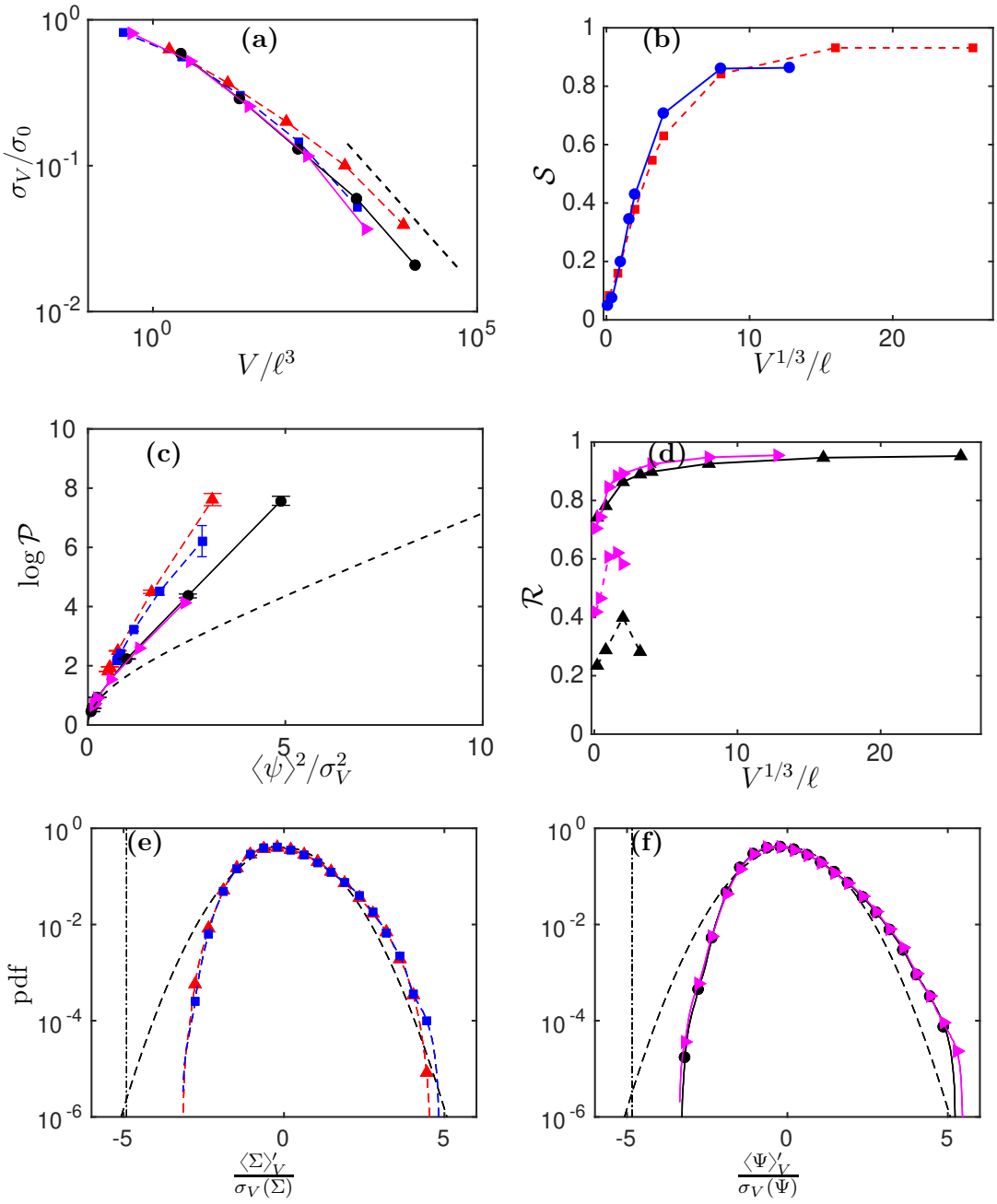

Figure 3.5: (a) σ_V as a function of V/ℓ^3, where the dashed line represents $\sigma_V \sim \mathcal{N}^{-1/2}$. Symbols correspond to: - -▲- -, $\Sigma(5\Delta_g)$; - -■- -, $\Sigma(10\Delta_g)$; —►—, $\Psi(5\Delta_g)$; —●—, $\Psi(10\Delta_g)$. (b) Correlation coefficient between Σ and Ψ as a function of the averaging volume: - -■- -, $\mathcal{S}_{\langle\Sigma\rangle_V,\langle\Psi\rangle_V}$ at $5\Delta_g$; —●—, $\mathcal{S}_{\langle\Sigma\rangle_V,\langle\Psi\rangle_V}$ at $10\Delta_g$. (c) Asymmetry function, $\mathcal{P}$, as a function of $\langle\psi\rangle^2/\sigma_V^2$. The dashed line is the exact solution of $\mathcal{P}$ for a Gaussian, which approaches $\log\mathcal{P} = 1/2\langle\psi\rangle^2/\sigma_V^2$ for large $\langle\psi\rangle^2/\sigma_V^2$. Error bars are calculated from the average standard deviation of $\log\mathcal{P}$ when partitioning the complete data-set in 4 subsets. (d) Interscale auto-correlation coefficient as a function of the averaging volume: —▲—, $\mathcal{R}_{\langle\Sigma\rangle_V}(5\Delta_g, 10\Delta_g)$; —►—, $\mathcal{R}_{\langle\Psi\rangle_V}(5\Delta_g, 10\Delta_g)$; - -▲- -, $\mathcal{R}^-_{\langle\Sigma\rangle_V}(5\Delta_g, 10\Delta_g)$; - -►- -, $\mathcal{R}^-_{\langle\Psi\rangle_V}(5\Delta_g, 10\Delta_g)$. (e,f) Probability density function of local markers of the energy cascade averaged at scale $V^{1/3} = 1.2L_0 = 32\Delta_g$: (e) Σ; (f) Ψ. The dashed-dotted lines represent $-\langle\psi\rangle/\sigma_V$ for quantities calculated at $5\Delta_g$. Symbols as in (a).

to backscatter increases until volumes of the order of $V^{1/3} \sim 2\ell$, and then decreases. Beyond $V^{1/3} \sim 4\ell$, the number of averaged inverse energy transfer events available are not enough to compute reliable correlations.

3.3.4 Physical-space estimates of the probability of inverse cascades

Figure 3.3(d) indicates that the probability of spontaneously observing an inverse cascade over extended regions of a turbulent flow is negligible, making it impractical to quantify the probability of such evolutions by direct observation. However, as shown in the previous section, we frequently observe local inverse energy transfer events over restricted regions of physical space. We estimate the probability of observing an inverse cascade using the integral asymmetry function,

$$\mathcal{P} = \frac{P(\langle\psi\rangle_V > 0)}{P(\langle\psi\rangle_V < 0)}, \tag{3.19}$$

which compares the probability of observing a direct to an inverse cascade on a volume V. This approach follows the methodology of the fluctuation relations [76] and its local versions [103, 104].

We evaluate the integral asymmetry function of Σ and Ψ for different averaging volumes, and show $\mathcal{P}$ as a function of $\langle\psi\rangle^2/\sigma_V^2$ in figure 3.5(d). We find that the probability of average inverse energy transfer decreases considerably with the averaging volume. Results in §3.3.2 suggest that, when the averaging volume is large enough, the integral asymmetry function might behave as that of a Gaussian distribution with non-zero mean and large $\langle\psi\rangle^2/\sigma_V^2$, $\log\mathcal{P} \simeq 2\langle\psi\rangle^2/\sigma_V^2$. In this scenario $\log\mathcal{P} \sim \mathcal{N} = V/\ell^3$ and the probability of direct over inverse cascades increases exponentially with the number of independent energy transfer events considered. However we find that $\log\mathcal{P} \sim 3\langle\psi\rangle^2/\sigma_V^2$. This deviation is a consequence of the strong dependence of $\mathcal{P}$ on the negative tails of the statistical distributions of Σ and Ψ. These tails decrease considerably with spatial averaging. In figure 3.4(a,b), we show that the probability density function of $\langle\Sigma(5\Delta_g)\rangle_V$ and $\langle\Sigma(5\Delta_g)\rangle_V$ averaged over a volume of $V = (16\Delta_g)^3$. They do not collapse with the distributions of $\Sigma(10\Delta_g)$, and $\Psi(10\Delta_g)$, due to the effect that averaging has on the tails, which is specially pronounced for the negative values. While the asymmetry function of Σ without volume averaging is $\log\mathcal{P} \sim 2$ across the inertial range [17], our results show that it increases to $\log\mathcal{P} \sim 4$ when Σ or Ψ are averaged over a volume twice the filter width

cubed. Moreover, the strong departure from Gaussianity of the tails persists for large averaging volumes. In figures 3.5(e,f), we display the probability distribution of $\langle\Sigma\rangle_V$ and $\langle\Psi\rangle_V$ for a volume of the order of the integral scale of the flow $V^{1/3} = 1.2L_0 = 32\Delta_g$. Neither of the two probability distributions are Gaussian. For this averaging volume, we do not find any average negative energy transfer event in the database.

Although energy transfer events are approximately local in physical and scale space, inverse and direct energy transfer events do not behave equally. As shown in §3.3.3, direct energy transfer events are correlated with events at larger scales, while backscatter events are not. These results corroborate that the direct cascade is a consequence of a multiscale process, and reveal that energy backscatter is local in scale space. As illustrated by simple cascade models [21, 105, 106], the interscale interactions responsible for the direct energy transfer produce intermittent direct energy transfer events, which dominate the statistics of the volume-averaged energy fluxes, and lead to the persistence of non-Gaussianity even for large averaging volumes. Although the multiscale nature of turbulence leads to non-trivial forms of the asymmetry function, our results suggest that the probability of inverse cascades decreases exponentially with the number of independent energy transfer events, indicating that the low probability of inverse cascades can be traced to the low probability of inverse energy transfer events.

Chapter 4

The structure of the inverse and direct cascades

The velocity gradients constitute a convenient descriptor of the fundamental structure of turbulent flows and some of their statistics reflect the out-of-equilibrium nature of turbulence. Although the velocity gradients describe only the structure of the small scales, the statistical distributions of the filtered velocity gradients are invariant across scales and reveal the self-similar structure of the inertial range [30, 80, 107, 108]. Some investigations suggest a connection between the velocity gradients in the inertial scales and the energy cascade [30, 40, 109], and common SGS models rely on the assumption that energy transfer towards the unresolved scales can be reproduced using the velocity gradients of the resolved scales [85, 97, 110]. The structure of the velocity gradients is compactly represented by the invariants of the velocity gradient tensor. Supported on the space-locality of the energy cascade reported in §3.3.2, we will relate these invariants, which are strictly local in space, with local energy fluxes, connecting the energy cascade in physical space to the local structure of the flow.

4.1 Dynamics of the invariants of the velocity gradient tensor

Let $\mathcal{A}_{ij} = \partial_j u_i$ be the velocity gradient tensor of an incompressible flow. The second and third invariants of $\mathcal{A}_{ij}$ are

$$Q = -\frac{1}{2}\mathcal{A}_{ij}\mathcal{A}_{ji} = \frac{1}{4}\omega_i\omega_i - \frac{1}{2}S_{ij}S_{ij}, \tag{4.1}$$

$$R = -\frac{1}{3}\mathcal{A}_{ij}\mathcal{A}_{jk}\mathcal{A}_{ki} = -\frac{1}{3}S_{ij}S_{jk}S_{ki} - \frac{1}{4}\omega_i S_{ij}\omega_j, \tag{4.2}$$

where ω_i is the i-th component of the vorticity vector. Considering R and the discriminant $D = 27/4R^2 + Q^3$, the flow can be classified in four different topological types: positive D corresponds to rotating topologies and negative D to saddle-node topologies; negative R accounts for topologies with a stretching principal direction, and positive R for topologies with a compressing principal direction. These invariants are also related to the vorticity vector and the rate-of-strain tensor, such that Q indicates the balance between enstrophy and strain, denoted by $|S|^2 = 2S_{ij}S_{ij}$ and $|\omega|^2 = \omega_i\omega_i$, and R represents the balance between vortex stretching and strain auto-amplification, $\omega_i S_{ij}\omega_j$ and $S_{ij}S_{jk}S_{ki}$. These terms appear in the evolution equations of $|S|^2$ and $|\omega|^2$,

$$\frac{1}{4}D_t|S|^2 = -S_{ij}S_{jk}S_{ki} - \frac{1}{4}\omega_i S_{ij}\omega_j - S_{ij}\partial_{ij}p, \tag{4.3}$$

$$\frac{1}{2}D_t|\omega|^2 = \quad \omega_i S_{ij}\omega_j, \tag{4.4}$$

where $D_t = \partial_t + u_j\partial_j$ is the substantial derivative along a Lagrangian trajectory and we have considered the evolution of an inviscid flow for simplicity.

The statistical distribution of Q and R in turbulent flows has a typical teardrop shape, which is shown in figure 4.1(e). For ease of reference we have divided the Q-R plane in four quadrants, where q_1 corresponds to $Q > 0$ and $R > 0$, q_2 to $Q > 0$ and $R < 0$, q_3 to $Q < 0$ and $R < 0$, and q_4 to $Q < 0$ and $R > 0$. The teardrop shape is characterised by a lobe in q_2, where the enstrophy is dominant over the strain and vortex stretching over strain auto-amplification, and a tail in q_4, which is known as the Vieillefosse [111] tail, and represents dominant strain auto-amplification over vortex stretching in strain-dominated regions. The high absolute values of Q in the Vieillefosse tail and in the upper semiplane indicate the spatial segregation of $|S|$ and $|\omega|$. Low absolute values of Q do

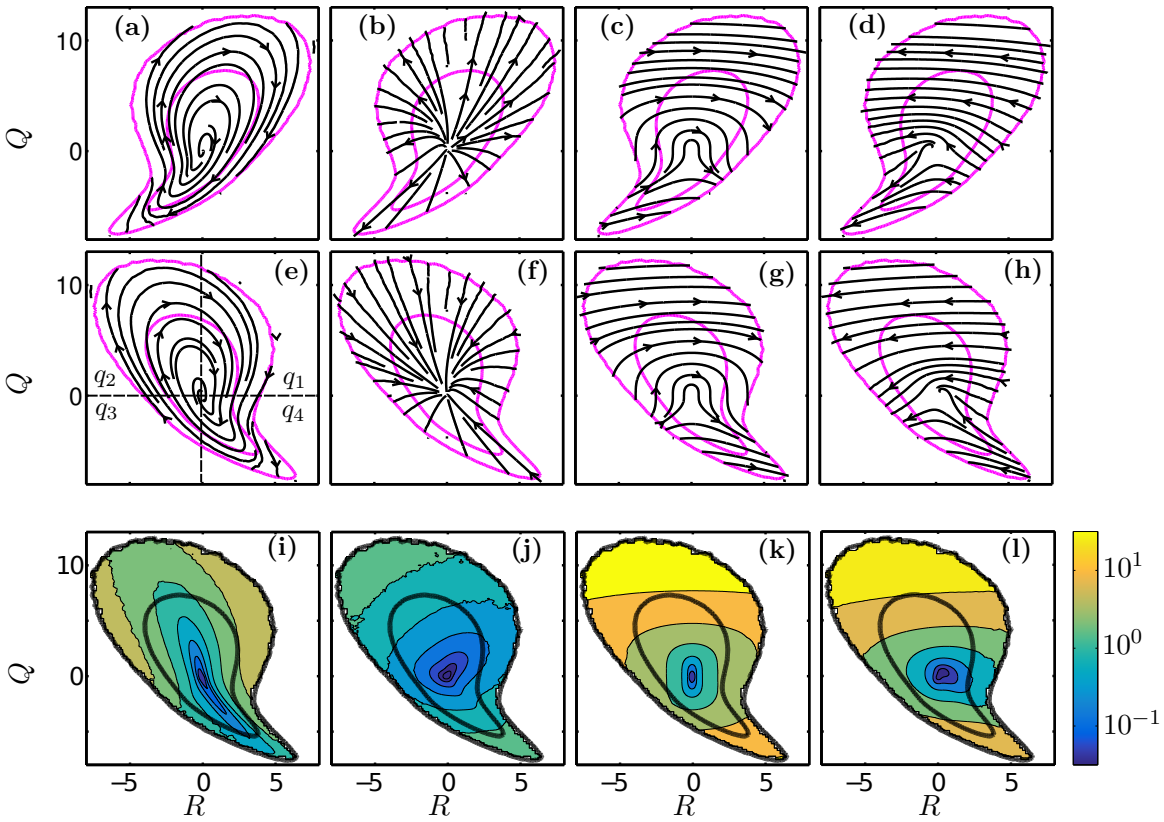

Figure 4.1: ⟶, conditional mean trajectories in the Q–R plane for the inverse (a-d) and direct (e-h) evolutions due to different contributions. (i-l) Modulus of the probability transport velocities $|\boldsymbol{\Phi}|$ in the Q–R plane in the direct evolution due to the different contributions. (a,e,i) All contributions $\boldsymbol{\Phi}_T$, (b,f,j) SGS model $\boldsymbol{\Phi}_M$, (c,g,k) restricted Euler $\boldsymbol{\Phi}_E$ and (d,h,l) non-local component of the pressure Hessian $\boldsymbol{\Phi}_P$. Contours of the probability density function of Q and R contain 0.9 and 0.96 of the total data. All quantities are normalised using $t_Q = \langle Q^2 \rangle^{1/4}$.

not in general imply low values of $|S|$ or $|\omega|$, but rather that $|S| \sim |\omega|$. We actually find that $|S| \sim \langle |S| \rangle$ in regions where $Q \sim 0$ and $R \sim 0$. For a detailed interpretation of the Q-R plane refer to Tsinober [42].

The dynamics of the velocity gradients can be statistically represented by the probability transport velocities in the Q–R plane, which are obtained from the average Lagrangian evolution of Q and R [112]. Taking spatial derivatives in the evolution equations of the velocity field described by (3.6) and considering (4.1, 4.2), the Lagrangian evolution of the invariants reads

$$D_t Q = -3R + \mathcal{A}_{ij}\mathcal{H}_{ji}, \tag{4.5}$$

$$D_t R = \frac{2}{3}Q^2 - \mathcal{A}_{ij}\mathcal{A}_{jk}\mathcal{H}_{ki}, \tag{4.6}$$

where $\mathcal{H}_{ij} = \mathcal{H}^P_{ij} + \mathcal{H}^M_{ij}$ comprises the contribution of the non-local component of the pressure Hessian and the SGS model, $\mathcal{H}^P_{ij} = \partial_{ij}p - \frac{1}{3}(\partial_{kk}p)\delta_{ij}$ and $\mathcal{H}^M_{ij} = \partial_j M_i$. Here, M_i stands as the i-th component of the SGS model in the momentum equation, and δ_{ij} is the Kronecker's delta. The total probability transport velocity is defined as

$$\mathbf{\Phi}_T = \{\langle D_t Q\rangle_C t_Q^3, \langle D_t R\rangle_C t_Q^4\}, \tag{4.7}$$

where $\langle\cdot\rangle_C$ stands as the probability conditioned to Q and R and $t_Q = 1/\langle Q^2\rangle^{1/4}$ is the characteristic time extracted from the standard deviation of Q. Let us note that the probability density flux in the Q-R plane is $P(Q,R)\mathbf{\Phi}_T$, where $P(Q,R)$ is the joint probability density of Q and R. The probability transport velocities are integrated to yield conditional mean trajectories (CMTs) in the Q–R plane [112], which are shown also in figure 4.1(e).

In order to analyse the dynamics of the invariants, we decompose the CMTs into the contribution of the different terms in the evolution equation of Q and R,

$$\mathbf{\Phi}_E = \{-3R, 2/3Q^2\}, \tag{4.8}$$

$$\mathbf{\Phi}_P = \{\langle \mathcal{A}_{ij}\mathcal{H}^P_{ji}\rangle_C, \langle -\mathcal{A}_{ij}\mathcal{A}_{jk}\mathcal{H}^P_{ki}\rangle_C\}, \tag{4.9}$$

$$\mathbf{\Phi}_M = \{\langle \mathcal{A}_{ij}\mathcal{H}^M_{ji}\rangle_C, \langle -\mathcal{A}_{ij}\mathcal{A}_{jk}\mathcal{H}^M_{ki}\rangle_C\}, \tag{4.10}$$

where $\mathbf{\Phi}_T = \mathbf{\Phi}_E + \mathbf{\Phi}_P + \mathbf{\Phi}_M$, and the normalisation with t_Q has been dropped for simplicity. First, we have the contribution of the restricted Euler (RE) [113], $\mathbf{\Phi}_E$, which depends exclusively on Q and R, and includes advection and the local action of the pressure Hessian. The non-local action of the pressure Hessian and the SGS model are included in $\mathbf{\Phi}_P$ and $\mathbf{\Phi}_M$ respectively. This decomposition is not unique, but serves to separate the strictly local dynamics of the restricted Euler from the non-local action of the pressure Hessian and the SGS model, allowing us to determine the dynamical origin of the CMTs and to analyse the differences between the direct and inverse evolutions. In order to compare the importance of the different terms, we consider the norm of the probability transport velocities,

$$|\mathbf{\Phi}| = \sqrt{(t_Q^3\langle D_t Q\rangle_C)^2 + (t_Q^4\langle D_t R\rangle_C)^2}. \tag{4.11}$$

Statistics of Q and R and their CMTs have been compiled for two different times in

the ensemble of realisations, $t_{stats} = (1 \pm 0.12)t_{inv}$, which correspond to the direct and inverse evolutions and are marked in figure 3.1(a). If we assume that the decay of the system is self-similar, conclusions drawn from this analysis should be independent of t_{stats}. The total probability transport velocity, $\mathbf{\Phi}_T$, has been calculated directly from the expression of the substantial derivative, computing separately the temporal and convective derivative. Appropriate numerical methods have been used in all the computations [114]. Results show that the number of realisations in our database is sufficient to converge the statistics.

The different contributions to the CMTs and the norm of the probability transport velocities in the inverse and direct evolutions are shown in figures 4.1(a-h) and 4.1(i-l). In the direct evolution, the CMTs develop an average rotating cycle characteristic of turbulent flows, which exposes causality between the different configurations of the flow in an average sense. The CMTs rotate clockwise: from vortex stretching to vortex compression in the upper semiplane, to the Vieillefosse tail in q_4, and again to vortex stretching in enstrophy-dominated regions.

The CMTs move from negative to positive R, and finally to the Vieillefosse tail, due to the effect of the RE dynamics. This trend would cause the appearance of infinite gradients in a finite time [111], but the non-local effect of the pressure Hessian and the SGS model, or viscosity in the case of DNSs, prevent it by bringing the CMTs back to q_3 and restarting the cycle. For closed steady states, CMTs describe a closed cycle [108], while in our decaying flow they spiral inwards due to the action the SGS model, which contracts the probability distribution, resembling the action of viscous terms in DNSs [115]. The CMTs of the non-local component of the pressure Hessian evolves from positive to negative values of R, following the same behaviour observed in Chevillard et al. [116] and Meneveau [115]. The norms of the probability transport velocity reveal that the RE dynamics are mostly counteracted by the non-local component of the pressure Hessian in regions where Q and R are large. These observations are in agreement with Luethi et al. [117], and evidence a secondary role of the model in the dynamics of intense gradients.

In the inverse evolution we identify substantial changes. As explained in §3.2.1, time-reversal changes only the sign of quantities which are odd with the velocity: Q remains unaltered while R changes sign, leading to an inverse teardrop shape. The Vieillefosse

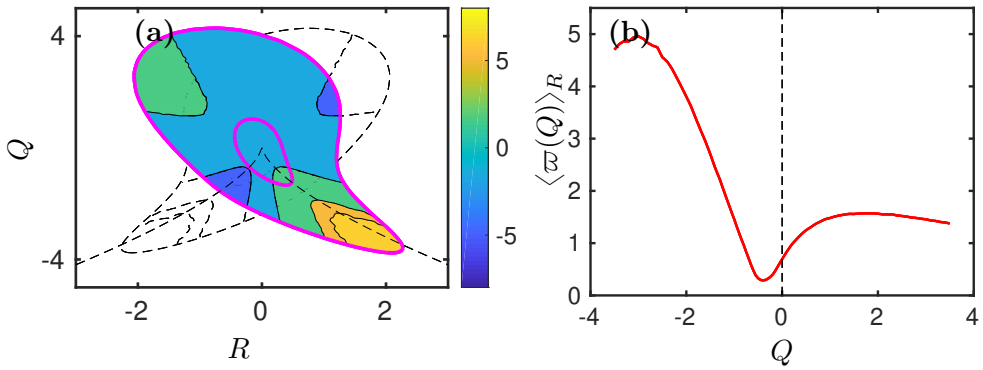

Figure 4.2: (a) Colour plot of the asymmetry function $\varpi(Q, R)$. Isocontours contain 0.4 and 0.7 of the total data. Dashed lines represents the contours of the asymmetry function for the change $R \to -R$. (b) Asymmetry function averaged along the R axis, $\langle \varpi(Q) \rangle_R$, for R in the interval $(-2, 2)$. Quantities are normalised using $t_Q = \langle Q^2 \rangle^{1/4}$.

tail lies now in q_3, forming an antitail, and a higher probability of vortex compression appears in enstrophy-dominated regions. This transformation also affects the CMTs, and is most relevant in the effect of the SGS model, which now expands the probability distribution and leads to an average outward spiralling. The behaviour of $\mathbf{\Phi}_E$ and $\mathbf{\Phi}_P$ is similar to the direct evolution in the upper semiplane, but undergoes fundamental changes in the lower semiplane. In the direct evolution, the non-local component of the pressure Hessian counteracts the RE dynamics, preventing the formation of intense gradients in the Vieillefosse tail. Conversely, in the inverse evolution, $\mathbf{\Phi}_P$ favours the growth of intense gradients in the antitail, which is contracted by the RE dynamics.

This analysis compares the structure of the attractor with that of the antiattractor and can be simply derived by considering the effect that the transformation $\boldsymbol{u} \to -\boldsymbol{u}$ has on the dynamics of the velocity gradients. However, in 3.3.1 we have identified inverse trajectories outside the antiattractor. We will show that, for these trajectories, this analysis yields non-trivial results.

4.2 Asymmetry in the Q–R space

In this section we quantify the differences in the structure of the flow between the turbulent attractor and the antiattractor. We use an asymmetry function defined in the Q-R plane

$$\varpi(Q, R) = \log \frac{P^+(Q, R)}{P^-(Q, R)}, \tag{4.12}$$

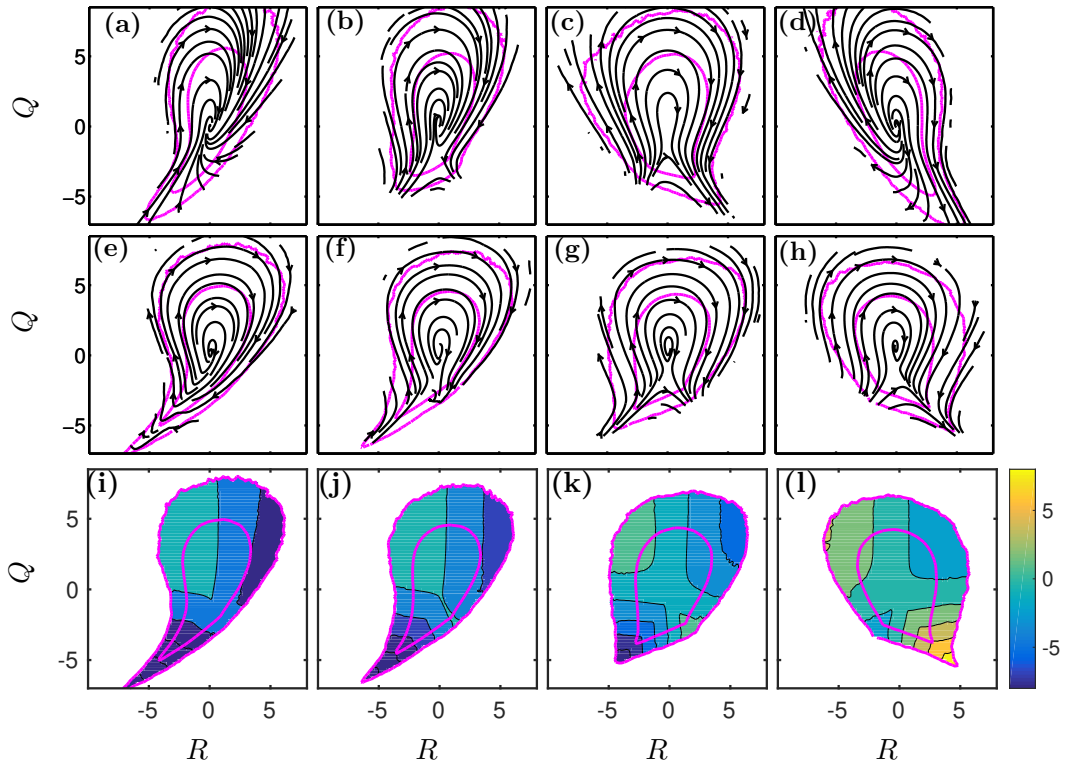

Figure 4.3: Conditional mean trajectories in the Q–R plane of the inverse evolution without model (see §3.2.3) for (a-d) the unfiltered case and (e-h) filtered at $\breve{\Delta} = 5\Delta_g$, and (i-l) conditional average of Σ at scale $\breve{\Delta} = 5\Delta_g$, at different times: (a,e) $t/T_0 = 0$; (b,f) $t/T_0 = 0.1$; (c,g) $t/T_0 = 0.15$; (d,h) $t/T_0 = 0.25$. ——, contours of the probability density function of Q and R containing 0.9 and 0.96 of the data. Q and R normalised with $t_Q = \langle Q(t_{inv})^2 \rangle^{1/4}$. Conditional-averaged energy fluxes in (i-l) are normalised with the absolute value of $\langle \Sigma \rangle$ at each time.

where P^+ and P^- denote the probability density of Q and R in the direct and inverse evolutions respectively. In figure 4.2(a) we show the distribution of $\varpi(Q,R)$ and in 4.2(b) the absolute values of the asymmetry function averaged along the R axis,

$$\langle \varpi(Q) \rangle_R = \frac{\int |\varpi(Q,R)| \, \mathrm{d}R}{\int \mathrm{d}R}. \tag{4.13}$$

Most of the temporal asymmetry of the velocity gradients is related to $Q < 0$, suggesting that the dynamics of enstrophy-dominated regions are statistically less affected by a time reflection than the dynamics of strain-dominated regions. Vortex stretching is on average dominant in the direct evolution, but the probability of vortex compression is not negligible. Both processes are shared by the inverse cascade, in which vortex compression is dominant but coexists with vortex stretching. On the other hand, the structure of strain-dominated regions depends strongly on the direction of the system

in time. Intense velocity gradients in $Q < 0$ are either in q_3 or q_4, depending on the direction of the cascade, but not simultaneously in both quadrants, which suggests that the dynamics of strain-dominated regions are more fundamentally related to the direction of the system in time than the dynamics of enstrophy-dominated regions.

4.3 Energy fluxes in the Q–R space

4.3.1 Inverse evolutions outside the antiattractor

In this section we analyse the relation between the structure of the flow and the energy cascade by conditioning the statistics of the local energy fluxes to the invariants of the filtered velocity gradients. First, we study the experiments on the inverse cascade without model, which are presented in §3.2.3. These experiments provide inverse evolutions outside the turbulent attractor, for which this analysis identifies the relevant mechanisms that support the inverse energy cascade.

We calculate the invariants of the filtered velocity gradients and their CMTs at scale $\breve{\Delta} = 5\Delta_g$. We use a Gaussian filter (3.7) and calculate the CMTs using the substantial derivative of the filtered field, $\breve{D}_t = \partial_t + \breve{u}_i\partial_i$. We analyse the temporal evolution of these quantities in the inverse evolutions when the model is removed, and connect them to the evolution of local energy fluxes in physical space, $\Sigma(\boldsymbol{x}, t)$, and in scale space, $\Pi(k, t)$. The analysis of Ψ yields qualitatively similar results and is excluded for simplicity.

Figure 4.3 shows the probability distribution of the invariants of the unfiltered (a-d), and filtered (e-h) velocity gradients and the their CMTs in the inverse evolution without model. In (i-l) we show the average of $\Sigma(5\Delta_g)$ conditioned to the invariants of the filtered velocity gradients. Initially, the invariants of the filtered and unfiltered velocity gradients form an inverse teardrop, and the average Σ conditioned to Q and R is predominantly negative and most intense in q_3 and q_1, suggesting a relevant role of the antitail and of vortex compression in the inverse cascade.

At time $0.1T_0$ after the inversion, the antitail of the unfiltered gradients contracts, while the antitail of the filtered gradients remains unaltered. The probability distribution in $Q > 0$ remains similar to the initial state in both cases. According to $\Pi(k, t)$ in figure

	All				‘+’				‘−’			
	q_1	q_2	q_3	q_4	q_1	q_2	q_3	q_4	q_1	q_2	q_3	q_4
$\langle\Sigma\rangle_{q_i}/\langle\Sigma\rangle$	0.11	**1.05**	0.81	**1.54**	0.37	**0.89**	0.85	**1.3**	**1.16**	0.72	0.91	0.89
$\{\Sigma\}_{q_i}/\langle\Sigma\rangle$	0.01	**0.28**	0.17	**0.54**	0.03	**0.27**	0.16	**0.52**	**0.56**	0.11	0.17	0.16

Table 4.1: Conditional averages of energy transfer and contributions to the total energy fluxes of each quadrant in the Q–R plane during the direct evolution. In the first table we have considered all data, in the second only direct energy transfer events, and in the last only backscatter events. Quantities are normalised with the average Σ in the first case, and with the averages conditioned to positive and negative fluxes in the other two cases.

3.2(a), the direct cascade has not yet regenerated at the small scales. At the filter scale, $\Pi(k,t)$ and $\langle\Sigma\rangle$ are still negative and similar in magnitude to the initial state.

At $0.15T_0$, the unfiltered velocity gradients start developing dominant vortex stretching, represented by a prominent lobe in q_2, and a regular Vieillefosse tail. The antitail, although reduced, is still observable in the filtered gradients and $\langle\Sigma\rangle < 0$. At this stage, as shown in 3.2(a), an inverse cascade at the filter scale and a direct cascade in the small scales coexist.

Finally, at $0.25T_0$, when the filtered velocity gradients develop structures in the Vieillefosse tail, the direct cascade recovers at the filter scale and $\langle\Sigma\rangle > 0$.

These results indicate a strong connection between the direction of the cascade and the orientation of the Vieillefosse tail. First, the conditional averages of Σ in the Q-R plane show that, at $0.25T_0$, when the energy cascade starts to regenerate at the filter scale, direct local energy fluxes are most intense in the q_4 quadrant. Second, the differences in the invariants of the filtered velocity gradients between $0.1T_0$ and $0.15T_0$ are only significant in the Vieillefosse tail, but the inverse energy fluxes are reduced by a half, $\langle\Sigma(0.15T_0)\rangle \simeq 0.5\langle\Sigma(0.1T_0)\rangle$.

The temporal symmetry between the statistics of enstrophy dominated regions in the attractor and antiattractor reported in §4.2 also holds during the transition from inverse to direct phase-space trajectories. We do not find substantial differences in the evolution of Q and R, or the CMTs, in the upper semiplane during the reconstruction of the direct energy cascade at the filter scale.

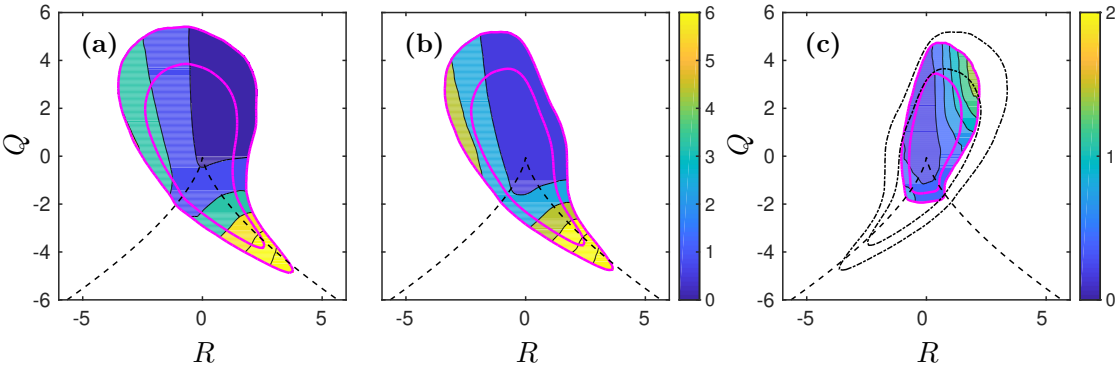

Figure 4.4: (a) Conditional average of Σ at scale $\breve{\Delta} = 5\Delta_g$ in the Q–R plane of the filtered velocity gradients for the direct evolution with model. (b) Average Σ over Q and R conditioned to $\Sigma > 0$. (c) Absolute value of the average Σ over Q and R conditioned to $\Sigma < 0$. Values of Σ normalised with $\langle\Sigma\rangle$ at t_{stats}. ——, contours of the probability density function of Q and R containing 0.85 and 0.9 of the data. In (c), – · – marks isocontours of Q and R conditioned to negative Σ for the inverse cascade. The dashed line corresponds to $D = 0$. Q and R normalised with $t_Q = \langle Q^2\rangle^{1/4}$.

4.3.2 Direct evolutions in the turbulent attractor

We perform the same analysis for the direct evolutions with SGS model, which reside within the turbulent attractor. Figure 4.4(a) shows the average Σ conditioned to Q and R. In order to discriminate between direct and inverse energy transfer, we also condition the probability distribution of Q and R to the sign of the local energy fluxes and present the results in figures 4.4(b-c). We quantify the relevance of each quadrant to the energy cascade by calculating the average of Σ conditioned each quadrant in the Q–R plane, $\langle\Sigma\rangle_{q_i} = \langle\Sigma|(Q,R) \in q_i\rangle$, and the total contribution of each quadrant to the energy fluxes, $\{\Sigma\}_{q_i} = \langle\Sigma\rangle_{q_i} P_{q_i}$, where P_{q_i} is the probability that Q and R belong to q_i and $\langle\Sigma\rangle = \sum_{i=1,4}\{\Sigma\}_{q_i}$. We have also calculated these quantities conditioning the averages to the direction of the energy fluxes, being

$$\langle\Sigma\rangle^+_{q_i} = \langle\Sigma|\Sigma > 0, (Q,R) \in q_i\rangle, \tag{4.14}$$

the average energy transfer conditioned to the quadrant q_i and to $\Sigma > 0$. Accordingly $\{\Sigma\}^+_{q_i} = \langle\Sigma\rangle^+_{q_i} P^+_{q_i}$ is the total contribution of the quadrant q_i to the positive energy fluxes. Here $P^+_{q_i}$ is the probability that Q and R belongs to q_i and that $\Sigma > 0$. Statistics conditioned to negative fluxes are denoted by $\cdot^-$. The value of these quantities are gathered in table 4.1.

Most intense direct energy transfer events are related to the Vieillefosse tail and to q_4, which has the highest average energy transfer, $\langle\Sigma\rangle_{q_4} \sim 1.5\langle\Sigma\rangle$, and contributes with approximately 50% of the total energy transfer. Also structures in q_2 are relevant to the cascade, with contributions of around 20-30% to the total fluxes. Conversely, the contribution of q_1 to direct energy transfer is negligible. When we condition the statistics to direct energy fluxes we obtain similar results. The statistics of Q and R conditioned to positive Σ yield almost a complete teardrop, except for a lower probability of events in q_1.

When conditioning to negative energy transfer events we find that the average backscatter is roughly similar in the four quadrants, but that the q_1 quadrant contributes the most to energy backscatter, with a 56% percent of the total. This is a consequence of inverse energy transfer events being mostly located in q_1. As shown in figure 4.4(c), the statistics of Q–R conditioned to backscatter resemble an inverse teardrop without an antitail. In the same figure we also plot Q and R conditioned to backscatter in the inverse cascade. By time symmetry, the anti-tail in q_3 contributes the most to backscatter in the inverse cascade, but this tail is absent in the direct evolution.

4.4 An entropic argument for the prevalence of direct energy fluxes

Topologies in the antitail are strongly connected to intense backscatter, but they have negligible probability in the direct cascade. Here we provide arguments that account for the low probability of these topologies, and consequently, of inverse cascades.

We consider the evolution of R in regions where the strain is dominant over the enstrophy, $|S|^2 \sim \langle|S|^2\rangle \gg |\omega|^2$, $R \sim -\frac{1}{3}S_{ij}S_{jk}S_{ki} = -\alpha_1\alpha_2\alpha_3$, and $\alpha_1 < \alpha_2 < \alpha_3$ are the eigenvalues of the rate-of-strain tensor. This is a good approximation to the dynamics in the Vieillefosse tail and the antitail, where we find that $|S|^2 \sim 100|\omega|^2$. Due to compressibility $\alpha_1 + \alpha_2 + \alpha_3 = 0$ and the sign of R is determined by the sign of the intermediate eigenvalue of the rate-of-strain tensor, such that $\alpha_2 > 0$ corresponds to $R > 0$ and topologies in the Vieillefosse tail, and $\alpha_2 < 0$ to $R < 0$ and to the antitail. We describe the evolution of R in terms of the evolution of α_2, whose equation reads

$$D_t\alpha_2 = -\alpha_2^2 - (\frac{1}{3}\partial_{kk}p + \upsilon_2). \tag{4.15}$$

Here $\partial_{kk}p = -\frac{1}{2}|S|^2 = -\alpha_1^2 - \alpha_2^2 - \alpha_3^2$ is the trace of the pressure Hessian, which is local, and υ_2 is the contribution of $\mathcal{H}_{ij}^P = \partial_{ij}p - \frac{1}{3}\partial_{kk}p\delta_{ij}$ to the evolution of α_2, which is non-local. We have discarded quadratic terms of the vorticity and the action of the SGS model, which has been shown to have a negligible contribution to the dynamics of intense gradients. See Nomura and Post [118] for the complete equations. Let us remove the action of the non-local component of the pressure Hessian, υ_2, which yields

$$D_t\alpha_2 = \frac{1}{3}(\alpha_1^2 + \alpha_3^2 - 2\alpha_2^2) > 0. \tag{4.16}$$

By definition $\alpha_1^2 > \alpha_2^2$ and $\alpha_3^2 > \alpha_2^2$, and the evolution of any initial value of α_2 results in the growth of the intermediate eigenvalue, leading to positive values of R. This is the effect of the RE dynamics, which depletes the antitail in the direct cascade, and generates intense strain in the Vieillefosse tail. The only inertial mechanism capable of preventing the rate-of-strain tensor from developing a positive intermediate eigenvalue is the non-local action of the pressure Hessian through υ_2. This analysis is consistent with the results presented in §4.1, where we observe that the non-local action of the pressure Hessian sustains the antitail in the inverse cascade.

The non-local component of the pressure Hessian depends on the complete flow field: in the absence of boundaries it can be expressed as a singular integral, which depends on all points of the domain [119, 120]. As a consequence, the pressure Hessian is in general decorrelated from the local dynamics of the velocity gradients [121]. In figure 4.5, we show the joint probability distribution of the of the two components of $\mathbf{\Phi}_P = \{\mathcal{A}_{ij}\mathcal{H}_{ji}^P, -\mathcal{A}_{ij}\mathcal{A}_{jk}\mathcal{H}_{ki}^P\}$ in the centre of the the Q–R plane, and in the Vieillefosse tail during the inverse and direct evolution. In regions where gradients are weak and enstrophy and strain are not segregated, the contributions of the non-local pressure Hessian to Q and R appear decorrelated, with a large scatter of the data with respect to the mean. In the Vieillefose tail, the non-local component of the pressure Hessian counteracts the RE dynamics, and its contributions to Q and R are correlated against the RE dynamics. When time is reversed, these correlations are necessary to sustain the anti-tail. As shown in 4.3.1, the contraction of the antitail is the first identifiable process in the transition from the inverse to the direct cascade, which indicates that these correlations are quickly destroyed when the inverse cascade is perturbed.

While the generation of topologies in the Vieillefose tail is a direct consequence of the

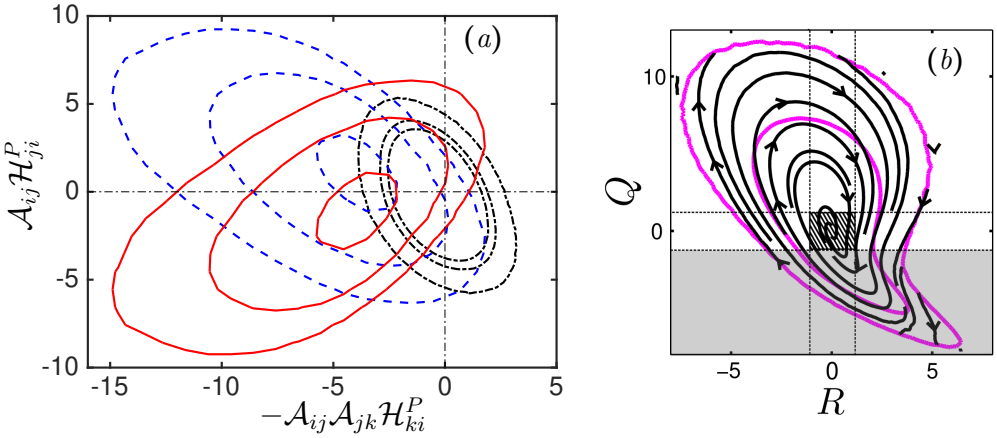

Figure 4.5: (a) Joint probability density function of the components of the probability transport velocities due to the non-local part of the pressure Hessian, $\{\mathcal{A}_{ij}\mathcal{H}^P_{ji}, -\mathcal{A}_{ij}\mathcal{A}_{jk}\mathcal{H}^P_{ki}\}$, conditioned to different areas in the Q-R plane: — · —, $|Q| < 1$ and $|R| < 1$, dashed region in (b); – – –, $Q < -1$ in the direct evolution, shaded region in (b); ——, $Q < -1$ in the inverse evolution, shaded region in (b). Quantities normalised with t_Q.

local autoamplification of the rate-of-strain tensor, the generation of topologies in the antitail requires a global configuration of the complete flow field that counteracts this amplification through the nonlocal action of the pressure Hessian. This scenario appears intuitively unlikely, suggesting that only specially organised flows are able to produce such action. This is the case of the initial conditions used for the inverse evolutions, which conserve all the information of the direct cascade process, in particular, the correlations between the rate-of-strain tensor and non-local component of the pressure Hessian in the Vieillefosse tail, which prevent the breakdown of the antitail in the inverse cascade.

Chapter 5

The phase-space mixing mechanisms of the cascade

5.1 Phase-space mixing and Lyapunov exponents

In §2.2, we have argued that phase-space mixing is the fundamental mechanism of entropy production in the energy cascade. Phase-space mixing takes place due to the chaotic nature of the system, which can be quantified by the average separation rate of nearby trajectories. The faster nearby trajectories diverge, the faster new unexplored regions of phase space can be occupied by the probability distribution, thus increasing entropy as measured by (2.3).

The rate of separation of nearby trajectories is measured by the Lyapunov exponents (LEs), which represent an essential tool in the characterization of dynamical systems, and quantify important properties, such as chaos or predictability. An extensive literature has been produced on the topic of Lyapunov exponents. We point to Eckmann and Ruelle [56], and references therein, for a review on the topic.

The LEs are defined as follows. We consider an initial base state in phase space, $\boldsymbol{\chi}(t_0)$, which follows a base trajectory, and a perturbed state, $\boldsymbol{\chi}^p(t_0)$, which is separated from the base state by an infinitesimal perturbation, $\delta\boldsymbol{\chi}(t_0) = \boldsymbol{\chi}^p(t_0) - \boldsymbol{\chi}(t_0)$. In the limit $t \to \infty$ and $|\delta\boldsymbol{\chi}(t_0)| \to 0$, the largest LE is defined as,

$$\lambda = \lim_{t\to\infty} \frac{1}{t} \log \frac{|\delta\boldsymbol{\chi}(t)|}{|\delta\boldsymbol{\chi}(t_0)|}, \tag{5.1}$$

where, under conditions of ergodicity [122], this limit exists and does not depend on t_0, $\boldsymbol{\chi}(t_0)$ or $\delta\boldsymbol{\chi}(t_0)$. Here $|\cdot|$ denotes a prescribed norm in phase space.

Similarly, let us consider the evolution of an infinitesimal spherical volume, $\delta\boldsymbol{\chi}^n$, along $\boldsymbol{\chi}(t)$, where n is the dimension of the phase space. As the spherical volume evolves, it is deformed into an ellipsoid, whose principal axes are $\delta\boldsymbol{\chi}_1, \delta\boldsymbol{\chi}_2, ..., \delta\boldsymbol{\chi}_n$. The average contraction or expansion of these axes defines the set of all Lyapunov exponents, known as the Lyapunov spectrum. In the limit of $\delta\boldsymbol{\chi}^n \to 0$ and $t \to \infty$,

$$\lambda_i = \lim_{t\to\infty} \frac{1}{t} \log \frac{|\delta\boldsymbol{\chi}_i(t)|}{|\delta\boldsymbol{\chi}_i(t_0)|}, \tag{5.2}$$

where $\lambda_1 > \lambda_2 > \cdots > \lambda_n$, and $\lambda_1 = \lambda$.

The amount of information produced in a chaotic system is defined, under certain conditions, as the sum of all positive Lyapunov exponents [123], known as the Kolmogorov-Sinai (KS) entropy

$$h_{KS} = \sum_{\lambda_i > 0} \lambda_i. \tag{5.3}$$

Positive KS entropy is characteristic of systems evolving under the action of chaotic dynamics. Althought the KS entropy quantifies information, it is related to the temporal derivative of H defined in (2.3). Latora and Baranger [89] identified a regime in the evolution of time dependent statistical ensembles of conservative systems in which

$$\mathrm{d}_t H = h_{KS}, \tag{5.4}$$

where h_{KS} is evaluated as the sum of the positive time-local LEs. The results of Latora and Baranger [89] support the intuitive idea that chaos is related to phase-space mixing, and evidence that the LEs can be used as quantify entropy production by phase-space mixing.

However, the calculation of the KS entropy for a highly dimensional system is a complex task beyond the current numerical techniques, and the available computer resources, even for moderate Reynolds numbers. This limitation imposes that we restrict our analysis to the most positive LE, rather than to the whole spectrum of positive exponents. The largest Lyapunov exponent can be readily computed, and provides an order-of-magnitude estimation of the KS entropy.

Following the general spirit of this work, we present a space- and time-local characterisation of the Lyapunov exponents, which connects the statistical formalism of phase-space with the complex spatio-temporal structure of turbulence. This approach is based on the study of the spatial structure of the so-called Lyapunov vectors (LVs). After a sufficiently long integration time, the perturbation fields used to calculate the LE approach a unique phase-space vector, which depends only the base flow field [124]. The LVs contain information on the processes that lead to the LEs in time, scale and space, and we use them to track and identify the mechanisms responsible for the generation of phase-space mixing in physical space.

This analysis also provides an insight into the Lyapunov characteristics of turbulent flows. As we will show, time-reversible turbulence offers the possibility to calculate and compare the largest and lowest Lyapunov exponents of the flow using standard procedures. Although, the negative LEs do not directly produce entropy through the spreading of the probability distribution, they play an essential role in the phase-space mixing process, which is described as the successive stretching and folding of the phase-space probability distribution, as depicted by the Baker's map or the Smale [125]'s horse shoe map. While stretching is associated with positive exponents, the folding process is related to the negative exponents.

5.2 The extreme Lyapunov exponents of a reversible turbulent flow

In this section, we calculate the highest Lyapunov exponent (HLE) of reversible LES turbulence in the direct and inverse evolutions. According to (5.1), the transformation $t \rightarrow -t$ is equivalent to changing the sign of the LE, which entails that the time-backwards HLE is equal to the time-forward lowest or most contractive Lyapunov exponent (LLE) with changed sign. That is $\lambda^+(-t) \rightarrow -\lambda^-(t)$, where λ^+ and λ^- denote the HLE and LLE respectively.

5.2.1 Algorithm

The extreme LEs are calculated for the reversible turbulent flow described in §3.1, whose evolution equations are revisited for clarity,

$$\begin{aligned} \partial_t u_i + u_j \partial_j u_i &= -\partial_i p + C_s \overline{\Delta}^2 \partial_j |S| S_{ij}, \\ \partial_i u_i &= 0. \end{aligned} \qquad \text{(3.6 revisited)}$$

The method used to estimate the extreme LEs is adapted from the standard procedure of Wolf et al. [126], which has already been applied to statistically stationary turbulence [127–129]. We modify this algorithm to account for the decaying nature of the system, and the impossibility of performing ergodic averages.

The calculations start with an initial velocity field $\boldsymbol{u}(t_0)$, and a small perturbation, $\delta\boldsymbol{u}$, which also fullfils continuity. The perturbed flow field is $\boldsymbol{u}^P(t_0) = \boldsymbol{u}(t_0) + \delta\boldsymbol{u}(t_0)$. Both the main and the perturbed flow fields are advanced a time Δt in parallel simulations, and a short-time approximation of the LEs is calculated,

$$\lambda_{st} = \frac{1}{\Delta t} \log \frac{\mathfrak{D}(t_0 + \Delta t)}{\mathfrak{D}(t_0)}, \tag{5.5}$$

where $\mathfrak{D}(t) = |\delta\boldsymbol{u}(t)|$ is the norm of the perturbation field at time t, to be defined later, and λ_{st} depends on t_0, $\delta\boldsymbol{u}(t_0)$, and Δt. We impose that the initial perturbation is small enough to evolve under the linearised dynamics of (3.6).

In order to approximate the HLE, $\delta\boldsymbol{u}$ must be linearly evolved for a sufficiently long time. We prevent non-linearity in the evolution the perturbation due to its exponential growth by applying an iterative re-scaling procedure. After each time-interval Δt, the distance between both trajectories, $\mathfrak{D}(t_0 + \Delta t)$, is evaluated and the perturbation field is re-scaled to its original distance,

$$\delta\boldsymbol{u} \leftarrow \delta\boldsymbol{u} \frac{\mathfrak{D}(t_0)}{\mathfrak{D}(t_0 + \Delta t)}. \tag{5.6}$$

The process is repeated for m number of iterations, resulting in a set of m short-time approximations of the LE along a trajectory, $\lambda_{st}(i\Delta t)$, where $i = 1, \ldots, m$. This procedure is applied to $N_s = 2000$ different trajectories in the direct and inverse evolutions, and the

short-time approximations of the LE are ensemble-averaged to yield a time-dependent LE.

We will show that, for $i\Delta t$ and N_s sufficiently large, the ensemble average of $\lambda_{st}(i\Delta t)$ converges to a well-defined value in the direct and inverse evolutions. We also find that the perturbation vectors along each trajectory evolve towards fields with common and well-defined characteristics, indicating the convergence of $\delta\boldsymbol{u}$ to the LVs, which we denote by $\delta\boldsymbol{u}^+$ for the HLE and $\delta\boldsymbol{u}^-$ for the LLE. The short-time approximations to the LE and the ensemble-averaging are necessary due to the decaying nature of the base system.

5.2.2 Implementation

The HLE is approximated along the forward evolutions starting with an initial random perturbation field, $\delta\boldsymbol{u}(t_0)$. When t_{inv} is reached, and the sign of the flow field is inverted, $\boldsymbol{u}^\iota = -\boldsymbol{u}$, a new random perturbation is used for the backward trajectory starting at t_{inv}. Distances in phase space are calculated using the L_2 norm in Fourier space, $\mathfrak{D}^2 = \sum \delta\widehat{u}_i \delta\widehat{u}_i^*$, where the summation is taken over all Fourier modes. This norm is convenient given that a conservation Liouville equation holds in a canonical form for the truncated Euler equations in Fourier space [91]. The initial perturbation is chosen in the form of (3.14), which we revisit here for clarity

$$\delta\widehat{u}_i(\boldsymbol{k}) = \widehat{u}_i(\boldsymbol{k}) \cdot \mu \exp(\mathrm{i}\phi), \qquad \text{(3.14 revisited)}$$

where ϕ is a random angle with uniform distribution between 0 and 2π, and μ is a real parameter that sets the initial energy of the perturbation. The same ϕ is used for the three velocity components, so that incompressibility holds also for $\hat{\boldsymbol{u}}^P$. This form of the initial perturbation is chosen for convenience, as it allows to set the energy of the initial perturbation proportional to the energy of the flow field through the parameter μ, controlling numerical issues derived from finite precision arithmetic, while keeping $\delta\boldsymbol{u}$ small enough to evolve linearly.

In order to check the dependence of the LEs on μ and Δt, we have calculated the LEs for values in the range $\mu = 10^{-2} - 10^{-6}$ and $\Delta t = 0.007 - 0.1398 T_0$. In all cases, we have obtained similar values of the LEs. All values of μ and Δt in this range are adequate

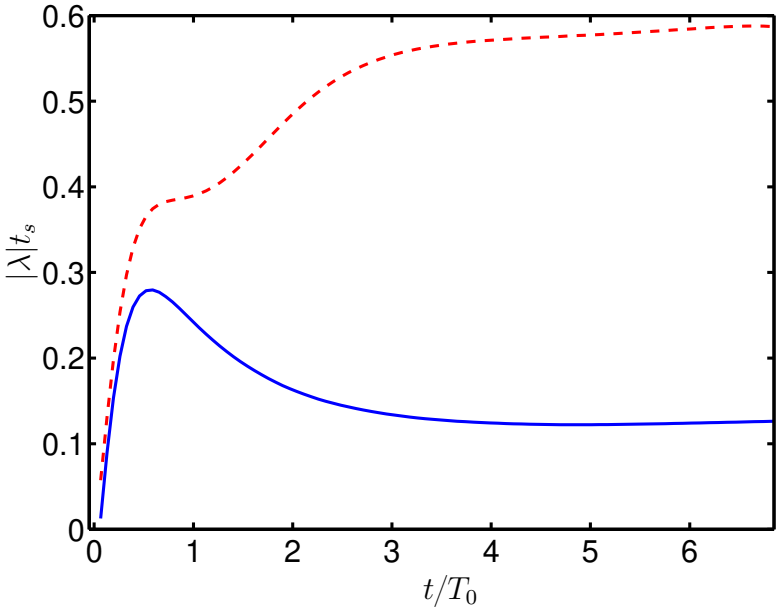

Figure 5.1: Evolution of the ensemble-averaged extreme LEs, $\lambda^{\pm}t_s$ as a function of time in the forward evolution of the system. ——, HLE; – – – LLE. The origin of the time axis is t_0 for the HLE and t_{inv} for the LLE. t_s is the pseudo-Kolmogorov time scale defined in §3.2.

to keep the evolution of the perturbation in the linear regime, while ensuring that the system has not changed substantially between evaluations of the short-time LE.

Different tests have been conducted to ensure the linear evolution of $\delta\boldsymbol{u}$, and to check that the final value of the LEs is independent of the initial form of the perturbation field. The evolution of two parallel initial perturbations with different initial norm , $|\delta\boldsymbol{u}_1|$ and $|\delta\boldsymbol{u}_2|$, have been compared for the same trajectory. The ratio of the two norms, $|\delta\boldsymbol{u}_1|/|\delta\boldsymbol{u}_2|$, holds during the computation of the Lyapunov exponent, proving that the evolution of the perturbations is linear.

In order to test convergence, short-time estimations of the LE have been calculated for the same trajectory starting with two different random initial perturbations, $\delta\boldsymbol{u}_1$ and $\delta\boldsymbol{u}_2$, with different initial norms. The LE obtained from the evolution of $\delta\boldsymbol{u}_1$, $\delta\boldsymbol{u}_2$, and $\delta\boldsymbol{u}_3 = \delta\boldsymbol{u}_1 - \delta\boldsymbol{u}_2$, converge to the same value as $i\Delta t$ becomes of the order of a few T_0.

5.2.3 Results

The ensemble-averaged evolutions of the short-time estimations of the HLE and the LLE are shown in figure 5.2(a). For ease of comparison, the HLE, which is obtained in the

inverse evolution, is presented with positive sign. Results show that the ensemble-average of short-time evaluations of the LE converges to an approximately constant value after an initial transient for both LEs. We consider this transient as an artefact of the particular structure of the initial perturbation field, and we discard it for statistical analysis.

The values obtained for the HLE, $\lambda^+ t_s = 0.125$, are in agreement with the HLE normalised with Kolmogorov units calculated in a direct numerical simulation of a turbulent channel flow by Keefe et al. [129]. In our case, we normalise the LEs with the pseudo-Kolmogorov time scale at each time. The standard deviation of $\lambda^\pm$ in the ensemble of realisations is less than 5% of the mean of the ensemble. The weak dependence of the LEs on the microscopic details of each different realisation in the ensemble indicates that the they are homogeneous characteristics of the turbulent attractor, and that they can be estimated by substituting a temporal average by an ensemble-average of short time evaluations.

The LLE is negative, and its absolute value is considerably higher than the HLE, $|\lambda^-| t_s = 0.58$. Further analysis of the structure of the LVs shows that these differences arise from the different nature of chaotic and dissipative dynamics: while the HLE is related to inertial dynamics, the LLE is connected to the dissipative mechanisms of the flow.

5.3 The structure of the Lyapunov vectors in scale space

The differences between the absolute value of λ^+ and λ^- can be explained by analysing their Lyapunov vectors. We define the general co-spectra of two vector fields $\boldsymbol{\psi}$ and $\boldsymbol{\zeta}$ as

$$E_{\boldsymbol{\phi\zeta}}(k) = 4\pi k^2 \mathrm{Re}\langle \widehat{\psi}_i \widehat{\zeta}_i^* \rangle_k, \tag{5.7}$$

where, in particular, the standard energy spectrum is $E = E_{\boldsymbol{uu}}$, and the energy spectrum of the Lyapunov vector is $E_{\boldsymbol{\delta u \delta u}}(k,t)$. The latter represents how the energy of the LV is distributed across scales, and is useful to determine the typical length scale of the processes that lead to the LEs.

By considering the evolution equation of $\boldsymbol{\delta u}$, we derive an equation for the evolution of $E_{\boldsymbol{\delta u \delta u}}(k,t)$. This equation is constructed by particularising (3.6) for the main trajectory,

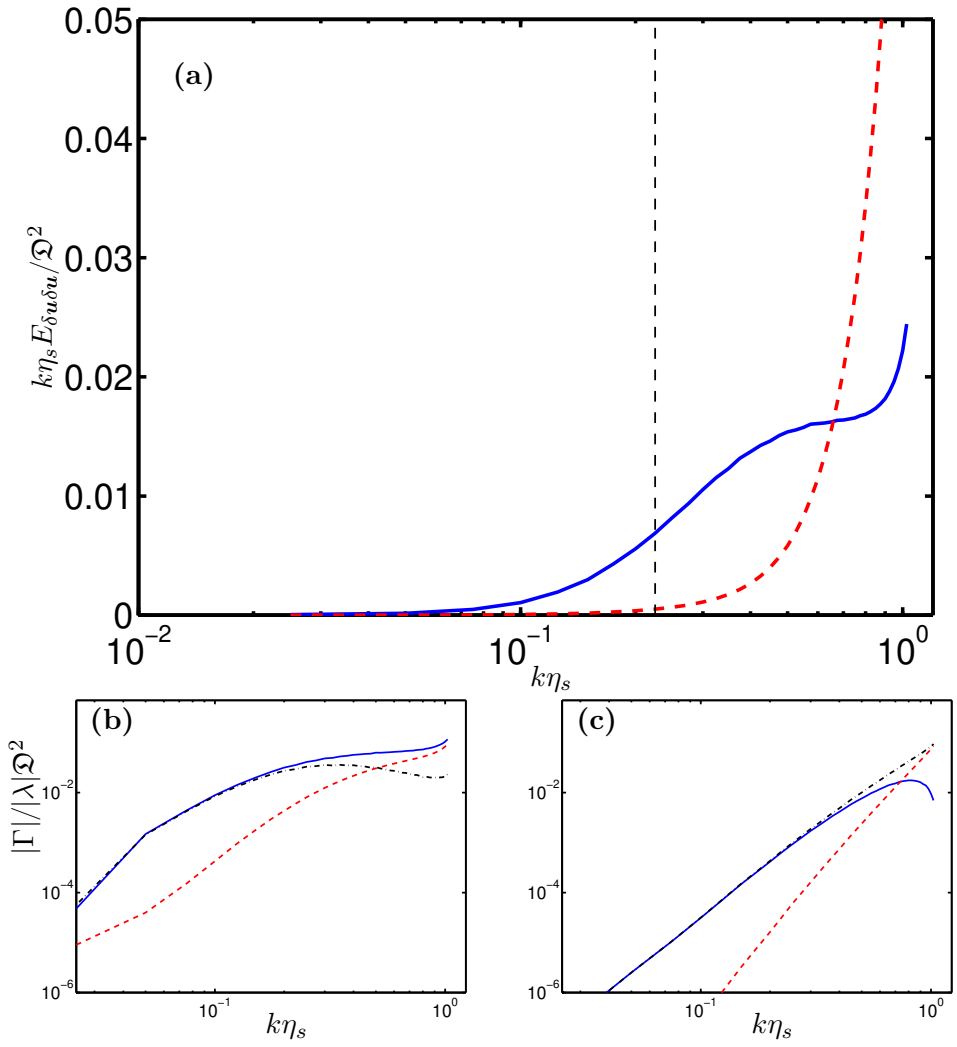

Figure 5.2: (a) Premultiplied time- and ensemble-average spectrum of the LV, $k\eta_s E_{\delta\boldsymbol{u}\delta\boldsymbol{u}}$, for: ——, HLE; – – – LLE. Spectra normalised with $\mathfrak{D}^2$. Horizontal dashed line marks the beginning of the model-dominated scales: $k\eta_s = 0.25$. (c,d) Absolute value of the time- and ensemble-averaged production spectra for the different contributions. (c) HLE: ——, $\Gamma_{\boldsymbol{B}}$; – – –, $|\Gamma_{\boldsymbol{M}}|$; – · – $|\Gamma_{\boldsymbol{B}} + \Gamma_{\boldsymbol{M}}|$. (d) LLE: ——, $|\Sigma_{\boldsymbol{B}}|$; – – –, $|\Gamma_{\boldsymbol{M}}|$; – · – $|\Gamma_{\boldsymbol{B}} + \Gamma_{\boldsymbol{M}}|$. Production spectra normalised with the ensemble- and time-averaged LE and $\mathfrak{D}^2$.

$\boldsymbol{u}(t)$, and for the perturbed trajectory, $\boldsymbol{u}^P(t)$, and subtracting both equations. Projecting this equation on a Fourier basis leads to,

$$\mathrm{d}_t \delta\hat{u}_i = \delta\widehat{B}_i + \delta\widehat{M}_i, \tag{5.8}$$

where $B_i = -u_j\partial_j u_i - \partial_i p$ are the non-linear terms of the NS equations, $M_i = C_s\Delta^2\partial_j|S|S_{ij}$ represents the SGS model, and δ denotes the difference between terms in the main and the perturbed trajectory to order $\delta\boldsymbol{u}$. Contracting (5.8) with $\delta\hat{\boldsymbol{u}}^*$ and taking averages

over wave-number shells, $4\pi k^2 \mathrm{Re}\langle\cdot\rangle_k$, we arrive to an equation for the evolution of the spectra of the LV,

$$\frac{1}{2}\,\mathrm{d}_t E_{\delta\boldsymbol{u}\delta\boldsymbol{u}} = \Gamma_{\boldsymbol{B}} + \Gamma_{\boldsymbol{M}}, \tag{5.9}$$

where $\Gamma_{\boldsymbol{B}} = E_{\delta\boldsymbol{u}\delta\boldsymbol{B}}$ and $\Gamma_{\boldsymbol{M}} = E_{\delta\boldsymbol{u}\delta\boldsymbol{M}}$ represent the contribution in scale-space to the amplification of the perturbations due to the non-linear terms and to the SGS model. Considering that $\sum_k E_{\delta\boldsymbol{u}\delta\boldsymbol{u}}(k) = \mathfrak{D}^2$ and that $\log\phi = \int \phi^{-1} d_t\phi \,\mathrm{d}t$, we express (5.5) as the time average of (5.9) over a time interval Δt,

$$\lambda(t_0+\Delta t) = \frac{1}{\Delta t}\log\frac{\mathfrak{D}(t_0+\Delta t)}{\mathfrak{D}(t_0)} = \frac{1}{\Delta t}\int_{t_0}^{t_0+\Delta t}\frac{\sum_k(\Gamma_{\boldsymbol{B}}+\Gamma_{\boldsymbol{M}})}{\sum_k E_{\delta\boldsymbol{u}\delta\boldsymbol{u}}}\,\mathrm{d}t, \tag{5.10}$$

connecting the production terms, $\Gamma_{\boldsymbol{B}}$ and $\Gamma_{\boldsymbol{M}}$, to the sign and absolute value of the LEs.

5.3.1 Results

The ensemble-averaged spectra of the LVs for both LEs are shown in figure 5.2(a). The spectra of the LVs and production terms have been ensemble- and time-averaged using data in the time interval in which the LEs reach a plateau, and $\delta\boldsymbol{u}$ has converged to the LV. These intervals correspond to ($t_{inv}/2$, t_{inv}) for the forward evolutions and ($3t_{inv}/2$, $2t_{inv}$) for the backward evolutions. The standard deviation of the spectra in the ensemble is small compared to the ensemble-averaged spectrum, and does not change considerably in the analysed time-interval, indicating that also the structure of the LVs is similar across the turbulent attractor.

The spectra of the LV of the HLE grows with decreasing scale until it reaches a plateau, while the LV of the LLE yields a steep spectra, with energy concentrated mostly on the smallest resolved scale. A slight tendency towards a power law, with exponent between 1 and 2, is observed in the large scales of the spectra of $\delta\boldsymbol{u}^+$, while in the case of $\delta\boldsymbol{u}^-$, a clear k^3 behaviour is identified for all wave-numbers.

The differences between both LEs and the spectra are also reflected in the production terms in scale space, which are shown in figure 5.2(c,d). In the HLE, we find that $\Gamma_{\boldsymbol{B}} > 0$ and that $\Gamma_{\boldsymbol{M}} < 0$, indicating that the chaotic behaviour of the system arises only, as expected, from non-linear interactions. The total amplification is most intense around $k\eta_s \sim 0.3$, and is lower at higher wavenumbers due to the effect of the SGS model, which

acts as a damping term, and limits the growth of perturbations in the smallest resolved scales.

Below $k\eta_s \sim 0.3$, inertial dynamics, which are the only source of chaos, appear constrained by the LES model. This phenomenon has been previously documented in the work of Yoshida et al. [50] and Lalescu et al. [51], who observed that perturbations introduced in scales below $k\eta = 0.25$ are damped by viscosity, indicating that, below this scale, the dynamics are enslaved to the interaction with larger scales.

A different picture emerges in the analysis of the production terms of the LLE. Due to negative eddy-viscosity, the model acts in the backward evolution as an amplifying term, $\Gamma_{\boldsymbol{M}} > 0$ ($\Gamma_{\boldsymbol{M}} < 0$ in the forward evolution), and is more intense in the large wavenumbers, where gradients are stronger. Most of the amplification of $\delta\boldsymbol{u}^-$ (contraction in the forward trajectory) is concentrated close to the resolution limit, where the effect of sub-grid dissipation is dominant over the non-linear terms. These results are in agreement with the work of Yamada and Ohkitani [130], who observed that the LV of the lowest LE in a shell model of turbulence peaks intensely at the smallest resolved scales. Production due to the non-linear terms also aids the overall amplification, $\Gamma_{\boldsymbol{B}} > 0$, ($\Gamma_{\boldsymbol{B}} < 0$ in the forward trajectory), but its contribution is marginal compared to that of the model in the resolution limit. The LV of the LLE represents the perturbation that is damped the fastest, which agrees well with the reported connection between the dynamics of the LV and the dissipative mechanisms of the flow.

To summarise, the HLE reflects chaos generated by non-linear interactions at the smallest inertial scale of the flow, whereas the LLE is strictly related to the sub-grid energy transfer at the resolution limit. Since the focus of this investigation is the turbulent cascade, and the SGS model represents only a necessary tool, we will isolate the inertial scales from dissipative mechanisms, allowing to study the Lyapunov structure of the inertial range.

5.4 The Lyapunov exponents in the inertial scales

A new procedure is devised to calculate the extreme LEs in scales where the dynamics are not affected by the SGS model. The new LEs are computed following, with some modifications, the procedure in §5.2. In order to avoid the effect of the SGS model, the

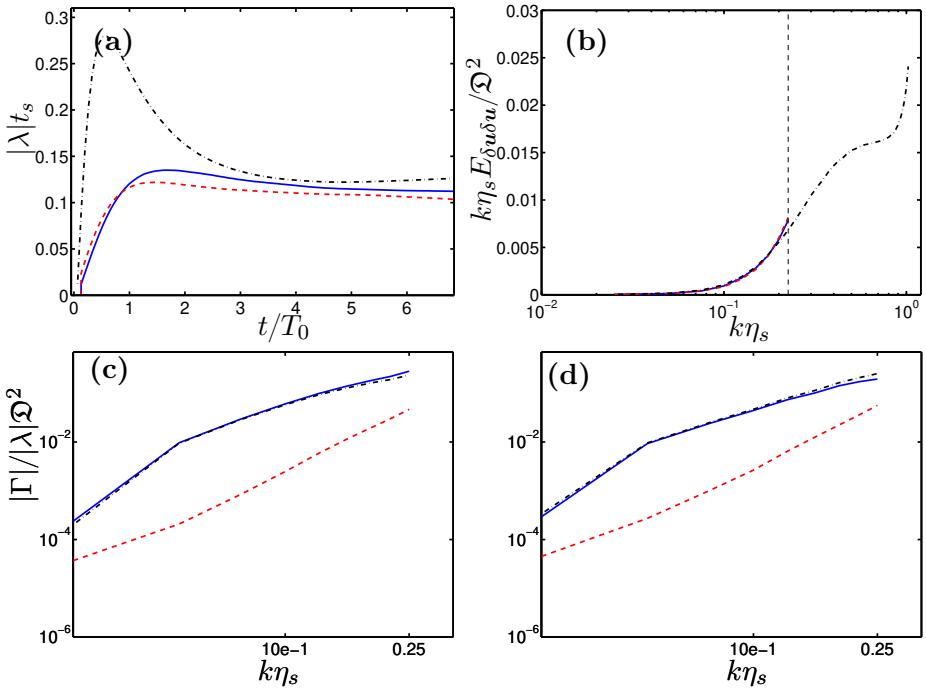

Figure 5.3: (a) Absolute value of the ensemble-averaged extreme LEs in the inertial range, $\lambda^{\pm}t_s$, as a function of time in the forward evolution of the system. ——, HILE; – – –, LILE; – · –, HLE. (b) Premultiplied perturbation spectra $E_{\boldsymbol{uu}}$. —— HILE; – – – LILE; – · –, HLE. Spectra normalised with $\mathfrak{D}^2$. Horizontal line marks the beginning of the model-dominated scales: $k\eta_s = 0.25$. Spectrum of the HLE normalised so that $\Sigma E_{\boldsymbol{uu}} = 1$. Spectra of HILE and LILE normalised to match the energy HLE spectrum for $k\eta_s < 0.25$. (c,d) Absolute value of the production spectra of the inertial LEs for different contributions. (c) HILE. ——, $|\Gamma_{\boldsymbol{B}}|$ (—); – – –, $|\Gamma_{\boldsymbol{B}}|$; – · –$|\Gamma_{\boldsymbol{B}}+\Gamma_{\boldsymbol{M}}|$. (d) LILE.——, $|\Gamma_{\boldsymbol{B}}|$ (—);– – –, $|\Gamma_{\boldsymbol{M}}|$; – · –$|\Gamma_{\boldsymbol{B}}+\Gamma_{\boldsymbol{M}}|$. Production of the HILE with positive sign.

perturbation field, $\delta\boldsymbol{u}$, is forced to remain confined in modes with wavenumber smaller than $k\eta_s = 0.25$, and the interactions which yield components outside this set are inhibited. To ensure that this condition is fulfilled during the evolution of $\delta\boldsymbol{u}$, an assimilation process of the main trajectory to the perturbed trajectory is applied [50], and

$$\hat{\boldsymbol{u}}(\boldsymbol{k}) = \hat{\boldsymbol{u}}^P(\boldsymbol{k}) \text{ if } k\eta_s > 0.25 \tag{5.11}$$

is imposed at every time step. This operation is equivalent to forcing that $\delta\boldsymbol{u}(\boldsymbol{k}) = \boldsymbol{0}$ if $k\eta_s > 0.25$, which is similar to a filtering operation applied on the perturbation field with a sharp-Fourier filter at scale $\Delta_\lambda = 25\eta_s$. The experimental set-up is in all other aspects similar to §5.2. This procedure is used to calculate the highest and lowest inertial Lyapunov exponents, HILE and LILE, which are denoted by λ_ι^+ and λ_ι^- respectively. Their corresponding LVs are denoted by $\delta\boldsymbol{u}_\iota^+$ and $\delta\boldsymbol{u}_\iota^-$,

The ensemble-averaged time-evolution of the inertial LEs is displayed in figure 5.3(a), which shows that λ_ι^+ converges to a value similar to the HLE when the effect of the dissipative scales is removed. Surprisingly, also the absolute value of λ_ι^- reaches a similar value to λ_ι^+ and to λ^+. The similar values of $|\lambda_\iota^+|$ and $|\lambda_\iota^-|$ suggests a potential symmetry of the Lyapunov spectrum in the inertial scales, which is characteristic of conservative dynamics.

Figure 5.3(b), shows the ensemble-averaged premultiplied spectra of the LVs in the inertial scales, which are similar and match the spectrum of the highest LV for $k\eta_s < 0.25$. Most of the energy is concentrated towards $k\eta_s = 0.25$, where the boundary for the perturbations is imposed by the assimilation process.

Figures 5.3(c,d) shows the production spectra of the inertial LEs, which are similar and are both dominated by the amplification due to the non-linear terms. In the case of the HILE, non-linear terms produce chaos, $\Gamma_{\boldsymbol{B}} > 0$, while, in the case of the LILE, they produce contraction of the perturbations, $\Gamma_{\boldsymbol{B}} < 0$. In both cases, $|\Gamma_{\boldsymbol{M}}|$ is only around 15% of $|\Gamma_{\boldsymbol{B}}|$, evidencing that the modes below $k\eta_s \sim 0.25$ are mostly driven by inertial mechanisms.

5.5 A space-local measure of chaos and phase-space mixing

The complex spatio-temporal structure of turbulent flows demands analytical procedures that are able to capture the distribution of relevant dynamics in the temporal and spatial coordinates. However, the analytical framework of statistical mechanics has not been yet fully adapted to consider these ideas.

We address this limitation by extending the definition of the LEs to the spatio-temporal coordinates of turbulent flows, where the spatial and temporal information is extracted from the analysis of the LVs. Following the approach used to derive (5.8), we define the Lyapunov exponent as the temporal average of the short-time LE,

$$\lambda = \lim_{\Delta t \to \infty} \frac{1}{\Delta t} \int_{t_0}^{t_0+\Delta t} \lambda_{st} \, \mathrm{d}t, \tag{5.12}$$

which is equivalent to (5.1). The short-time Lyapunov exponents is defined as the local amplification rate of the norm of $\delta\boldsymbol{\chi}$,

$$\lambda_{st} = \frac{1}{|\delta\boldsymbol{\chi}|}\,\mathrm{d}_t|\delta\boldsymbol{\chi}|. \tag{5.13}$$

This approach, which has been previously used by Vastano and Moser [128] or van Veen et al. [131] among others, serves to characterise the temporal structure of the LEs and their relation to the temporal dynamics of turbulent flows. The Lyapunov vectors are complete flow fields with spatial structure, and a similar decomposition of the LE is also possible in space.

5.5.1 The local amplification rate as a space-local Lyapunov exponent

We consider the LVs, $\delta\boldsymbol{u}^{\pm}(\boldsymbol{x},t)$, as flows field in physical space, where $\boldsymbol{x}$ has been purposefully introduced to indicate the dependence of $\delta\boldsymbol{u}$ on the spatial coordinates. We redefine the LEs as the spatial and temporal average of a scalar,

$$\lambda = \lim_{\Delta t\to\infty}\frac{1}{\Delta t}\int_{t_0}^{t_0+\Delta t}\langle\lambda_\ell(\boldsymbol{x},t)\rangle\,\mathrm{d}t, \tag{5.14}$$

where λ_ℓ is a space- and time-local decomposition of λ. Although this decomposition is not unique, and many forms of λ_ℓ fulfil (5.14), the evolution equations of $\delta\boldsymbol{u}$ provides a physically meaningful definition of λ_ℓ.

First, we subtract the evolution equation of $\boldsymbol{u}^P(\boldsymbol{x},t)$ from the evolution equation of $\boldsymbol{u}(\boldsymbol{x},t)$. Neglecting quadratic terms in $\delta\boldsymbol{u}$, we obtain an equation for the evolution of $\delta\boldsymbol{u}$ in physical space,

$$D_t\delta u_i = -\delta u_j\partial_j u_i - \partial_i\delta p + \partial_j(\nu_s\delta S_{ij} + \delta\nu_s S_{ij}), \tag{5.15}$$

where δp is the pressure field that enforces incompressibility on $\delta\boldsymbol{u}$, δS_{ij} is the rate-of-strain tensor of the perturbation field, and $\delta\nu_s$ is the difference between the eddy-viscosity of the main and the perturbed velocity field. The contraction of (5.15) with $\delta\boldsymbol{u}$ yields an equation for the evolution of the kinetic energy of $\delta\boldsymbol{u}$, denoted by $\Lambda(\boldsymbol{x},t) = \frac{1}{2}\delta u_i\delta u_i$,

$$D_t\Lambda = -\delta u_i S_{ij}\delta u_j - \delta S_{ij}(\nu_s\delta S_{ij} + \delta\nu_s S_{ij}) - \partial_j(\delta u_i\delta p_i - \delta u_i(\nu_s\delta S_{ij} + \delta\nu_s S_{ij})). \tag{5.16}$$

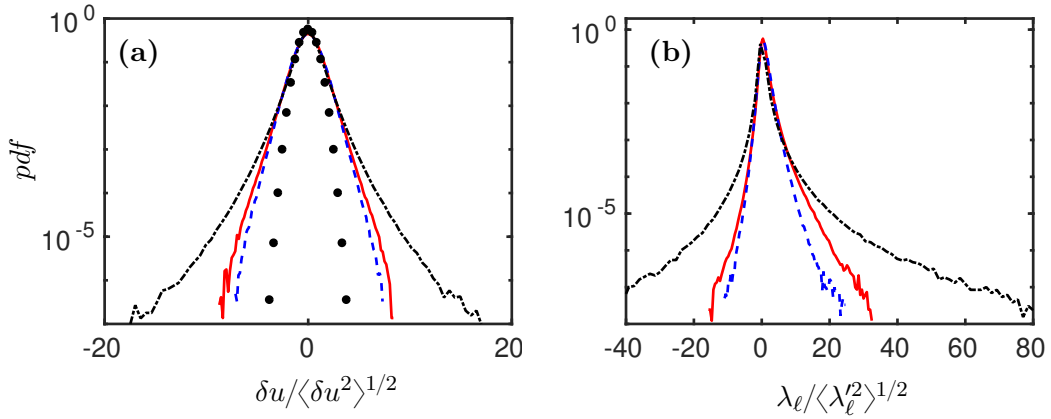

Figure 5.4: Probability density function of (a) $\delta u = \sqrt{2\Lambda}$ and (b) λ_ℓ of ——, HILE. – – –, LILE, – · –, HLE, •, Gaussian distribution. λ_ℓ for the LILE with positive sign.

Following a similar procedure as the one used to derive (5.9), and considering that $\mathfrak{D}^2 = 2\langle\Lambda\rangle$, we obtain

$$\lambda(t_0, \Delta t) = \frac{1}{2\Delta t} \log \frac{\langle\Lambda\rangle(t_0 + \Delta t)}{\langle\Lambda\rangle(t_0)} = \frac{1}{2\Delta t} \int_{t_0}^{t_0+\Delta t} \mathrm{d}_t \log\langle\Lambda\rangle \, \mathrm{d}t. \tag{5.17}$$

This equation can be further decomposed by considering that $\mathrm{d}_t\langle\Lambda\rangle = \langle D_t\Lambda\rangle$,

$$\lambda(t_0, \Delta t) = \frac{1}{\Delta t} \int_{t_0}^{t_0+\Delta t} \frac{\mathrm{d}_t\langle\Lambda\rangle}{2\langle\Lambda\rangle} \mathrm{d}t = \frac{1}{\Delta t} \int_{t_0}^{t_0+\Delta t} \frac{\langle D_t\Lambda\rangle}{2\langle\Lambda\rangle} \mathrm{d}t, \tag{5.18}$$

where the local amplification rate is defined as

$$\lambda_\ell(\boldsymbol{x}, t) = \frac{1}{2\langle\Lambda\rangle} D_t\Lambda(\boldsymbol{x}, t). \tag{5.19}$$

This decomposition is supported on the existence of an evolution equation for Λ, which allows to interpret λ_ℓ as the local amplification rate of the energy of the LV.

We focus on λ_ℓ, and not on Λ, because it contains dynamic information of the active amplification processes that lead to the LEs. This novel definition is original of this thesis, and we will use it to characterise the local structure of chaos and phase-space mixing in the inertial range. Results show that this quantity has potential applications for the characterisation of chaos in turbulent flows and other spatially extended chaotic systems.

5.6 Statistical analysis of the local amplification rate

We calculate λ_ℓ using the LVs of the HLE, the HILE and the LILE. We exclude from the analysis the LLE, which is mostly connected to the dynamics of the SGS model. In figure 5.4(a,b), we show the probability density function of the magnitude of the perturbation field, $\delta u = \sqrt{2\Lambda}$, and of λ_ℓ for the HLE, and for both inertial LEs, where λ_ℓ for the HILE is considered with positive value. Results show that δu is not specially intermittent, whereas λ_ℓ displays wide tails towards intense positive and negative values.

Although the sign of the LEs is well defined, λ_ℓ takes negative values in approximate 25% of the volume, and the average of $\lambda_\ell(\boldsymbol{x}) > 0$ is roughly $1.5\langle\lambda_\ell\rangle$ in the three cases. From the statistical analysis of λ_ℓ, we find that $\langle\lambda_\ell'^2\rangle^{1/2} \sim 3\langle\lambda_\ell\rangle$ for the inertial LEs and $\langle\lambda_\ell'^2\rangle^{1/2} \sim 6\langle\lambda_\ell\rangle$ for the HLE, which implies that λ_ℓ reaches positive and negative values an order or two of magnitude grater than the average. The positive tails of the probability distribution of λ_ℓ for the HLE approximate a power law with probability proportional to λ_ℓ^{-4}, whereas for the inertial LEs this trend is not observed.

The weighed probability distribution of λ_ℓ, $\lambda_\ell P(\lambda_\ell)$ indicates that the most important contributions to the mean come from events with an intensity close to the mean, $\lambda_\ell \sim \langle\lambda_\ell\rangle$. We will show that these events are related mostly to rather quiescent and featureless regions of the flow. The intermittent distribution of λ_ℓ suggests that the intense amplification events are localised in a small fraction of the volume, where λ_ℓ is several times larger than in the background. The statistical analysis of λ_ℓ reveals that intense positive events of λ_ℓ are connected to distinct events of the base flow, while negative events of λ_ℓ are not.

5.6.1 The spatial structure of the local amplification rate

We characterise the spatial distribution of intense events of Λ and λ_ℓ by studying the degree of clustering of these fields. We apply a procedure used in the analysis of coherent eddies in turbulent flows [41, 132, 133]. A test scalar field ϕ is thresholded at $a(\beta;\phi) = \langle\phi\rangle + \beta\langle\phi'^2\rangle^{1/2}$ and connected structures such that $\phi(\boldsymbol{x}) > a(\beta;\phi)$ are extracted. This procedure allows to estimate the typical size of regions where Λ or λ_ℓ are intense.

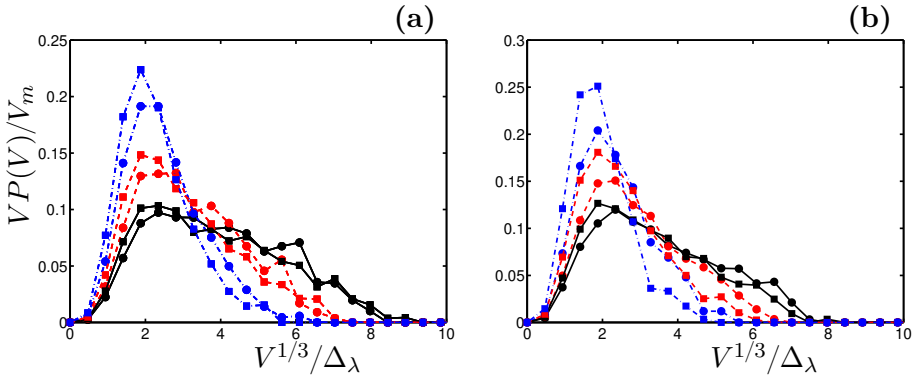

Figure 5.5: Probability density function of the fraction of the total volume $VP(V)/V_m$ contained in structures of size $V^{1/3}/\Delta_\lambda$ for (a) Λ and (b) λ_ℓ and for •, HILE; ■, LILE, where the mean volume is $V_m = \int VP(V)\,\mathrm{d}V$. Threshold $\beta =$: ———, 1.5; – – – 2.0; – · – , 3.0.

Figure 5.5(a,b) shows the probability density function of the fraction of the total volume that is contained in structures of a given size $V^{1/3}$ for Λ and λ_ℓ. The three different thresholds used are $\beta = 1.5$, 2 and 3. Results show that intense events of Λ and λ_ℓ are contained in structures with a typical size of approximately $2\Delta_\lambda = 50\eta_s$. The lowest threshold $\beta = 1.5$ contains approximately 20% of the energy of $\delta\boldsymbol{u}$ and 25% of the total positive λ_ℓ. Similar results where obtained for the LVs of the highest LE of the complete system (not shown), except that the clustering happens at scales of the order of $10\eta_s$.

5.6.2 The local amplification rate and the velocity gradients

By analysing the different terms that contribute to λ_ℓ in (5.16), we obtain a first evidence of the connection between the dynamics of the LVs and the dynamics of the base flow. The first term in right-hand side of (5.16) is the amplification associated with the stretching or compression of the perturbation field by the rate-of-strain tensor of the flow, $-\delta u_i S_{ij} \delta u_j$, which is the only term able to produce mean positive amplification in the forward evolutions. The second term is the dissipation of the perturbation field, $-\delta S_{ij}(\nu_\epsilon \delta S_{ij} + \delta\nu_\epsilon S_{ij})$, which is related to the gradients of $\delta\boldsymbol{u}$ and to $\delta\nu_\epsilon$, and can be neglected for the inertial LEs. The sign of this term depends on the sign of C_s, which is always negative for the forward trajectories. Finally, the third term, which represents the divergence of a flux and has zero average, describes the effect of the pressure and the diffusion of the SGS-model. This term rotates the perturbation vector in phase space, but its mean contribution to the total amplification is strictly zero. It follows from this

analysis that only the production due to the non-linear terms, and the dissipation due to the SGS model are responsible for the growth or decay of the norm of the LVs.

In §5.3, we have shown that the energy spectrum of the LVs of the extreme LEs peaks at the small scales of the flow, which suggests that the velocity gradients of the base flow play an important role in the amplification of the perturbations. This relation is directly extracted from (5.16), which shows the relation between the amplification of $\delta\boldsymbol{u}$ and the rate-of-strain tensor.

5.6.3 Conditional statistics of the local amplification rate

Following this analysis, we study the statistical connection of intense events of λ_ℓ for the inertial LEs with the local structure of the velocity gradients. The constrain imposed on $\delta\boldsymbol{u}$ to calculate the inertial LEs limits the smallest scale of the LVs. Consequently, we study the velocity gradients filtered at scale $\check{\Delta} = \Delta_\lambda = 25\eta_s$ with a Gaussian filter (3.7). Quantities calculated from the filtered gradients at scale $\check{\Delta}$ are marked with $\check{\cdot}$. We consider data in the temporal interval $(t_{inv}/2, t_{inv})$ for the forward evolutions and $(3t_{inv}/2, 2t_{inv})$ for the backward evolutions. Statistics are normalised with average values at each time.

We condition the statistics of λ_ℓ to the invariants of the filtered velocity gradient tensor, $\check{Q}$ and $\check{R}$, defined in (4.1) and (4.2), and to vortex stretching and strain production, $\check{\omega}_i S_{ij} \check{\omega}_j$ and $\check{S}_{ij}\check{S}_{jk}\check{S}_{ki}$. Figures 5.6(a,c) show the average of the positive events of λ_ℓ conditioned to $\check{Q}$ and $\check{R}$. We observe that strong local amplification of the HILE is mostly located in the tip of the Vieillefosse tail ($\check{Q} < 0$ and $\check{R} > 0$), where strain production is dominant over vortex stretching, and the strain is dominant over the enstrophy. The rate-of-strain tensor has in this quadrant two positive and one negative eigenvalue. Some intense amplification is also found in the $\check{Q} > 0$ and $\check{R} < 0$ quadrant. In the case of the LILE, amplification (contraction in the forward trajectory) is also more intense in the $Q < 0$ semi-plane but displaced towards $\check{R} \sim 0$. In this case we do not observe intense events in the upper semi-plane.

The conditional average of negative events of λ_ℓ are shown in figure 5.6(b,d). We observe some relation between negative events of λ_ℓ and vorticity-dominated regions of the flow. For the HILE, these events seem to be related with vortex compression, while for the

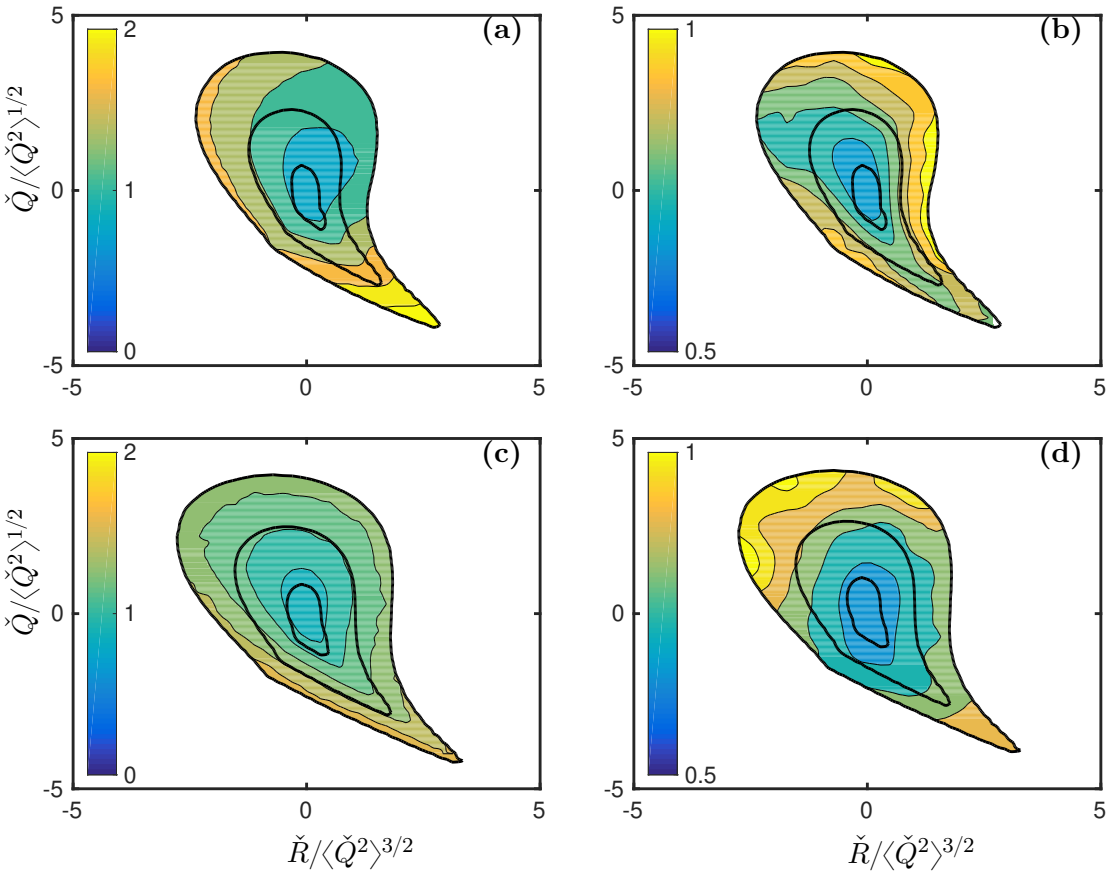

Figure 5.6: Average of positive local amplification rate λ_ℓ conditioned to $\check{Q}$ and $\check{R}$ for (a) HILE and (c) LILE. λ_ℓ for the HILE is considered with positive average value. Absolute value of the average of negative local amplification rate λ_ℓ conditioned to $\check{Q}$ and $\check{R}$ for (b) HILE and (d) LILE. Conditional averages normalised with the absolute value of $\langle\lambda_\ell\rangle$. ——, contours of the probability density function contain $\check{Q}/\langle\check{Q}^2\rangle^{1/2}$ and $\check{R}/\langle\check{Q}^2\rangle^{3/2}$ that contain 0.4, 0.6 and 0.8 of the data.

LILE there is a predominant relation of intense λ_ℓ with vortex stretching. However, the conditional averages of negative λ_ℓ events are closer to the mean than the averages of positive events, indicating that these events do not depend strongly on the local structure of the flow. These results evidence that weak and negative events of λ_ℓ are not associated with particularly intensente events of the base flow, but seem the consequence of weak background turbulence.

In figure 5.7(a-d), we present the average of positive events of λ_ℓ of the HILE and LILE conditioned, first, to the square of the rate-of-strain tensor and the square of the vorticity vector, and second, to vortex stretching and strain auto-amplification. For the HILE, the average amplification is larger for large values of $\check{S}_{ij}\check{S}_{ij}$ and large negative values of $\check{S}_{ij}\check{S}_{jk}\check{S}_{ki}$, which describes regions where the rate-of-strain tensor is strong, and

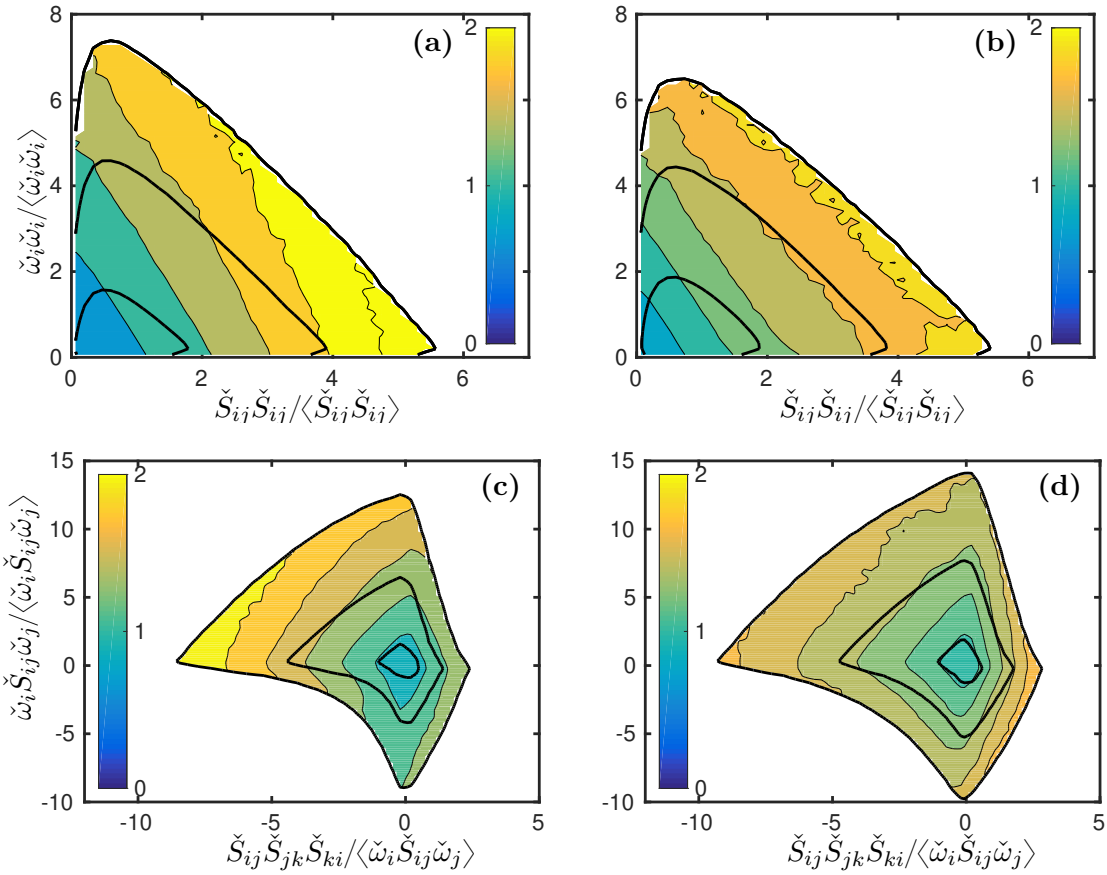

Figure 5.7: Average of positive local amplification rate λ_ℓ conditioned to (a,b) the square of the vorticity vector and the square of the rate-of-strain tensor and to (c,d) vortex stretching $\check{\omega}_i\check{S}_{ij}\check{\omega}_j$ and strain auto-amplification $\check{S}_{ij}\check{S}_{jk}\check{S}_{ki}$ for (a,c) HILE and (b,d) LILE. λ_ℓ for the HILE is considered with positive average value. Conditional averages normalised with the absolute value of $\langle\lambda_\ell\rangle$. ——, contours of the probability density function contain 0.6, 0.8 and 0.9 of the data.

has a negative intermediate eigenvalue. Intense amplification events of the HILE are related to a strong magnitude of the rate-of-strain tensor, but not to the sign of $\check{\omega}_i\check{S}_{ij}\check{\omega}_j$. In accordance to the conditional analysis in the $\check{Q}$ and $\check{R}$ space, intense λ_ℓ appears to be more correlated to the rate-of-strain tensor and the strain auto-amplification, than to the vorticity vector and vortex stretching.

5.6.4 The local amplification rate and the rate-of-strain tensor

We have presented statistical evidence of a strong connection between intense events of λ_ℓ and an intense magnitude of the rate-of-strain tensor. We further characterise this relation by analysing the local configuration of $\delta\boldsymbol{u}(\boldsymbol{x},t)$ with respect to the principal

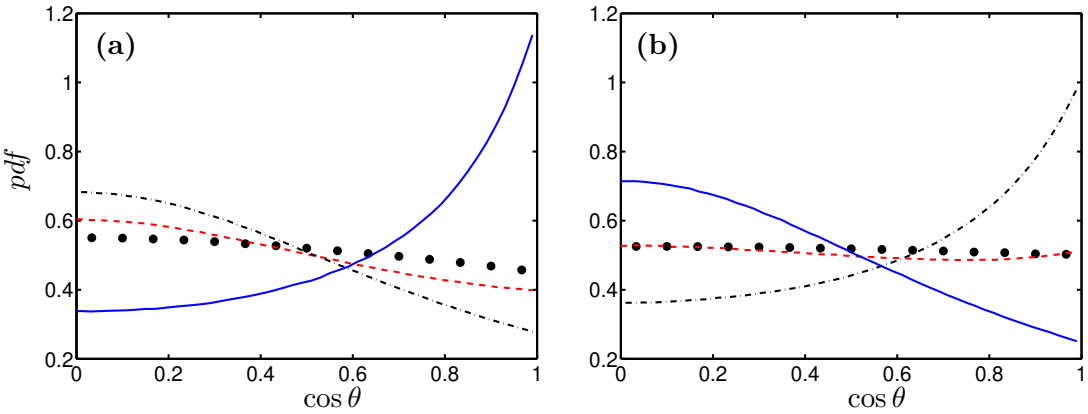

Figure 5.8: Cosine of the angle of alignment of the local perturbation field $\delta\boldsymbol{u}$ with the eigenvectors of the rate-of-strain tensor and with the vorticity vector for (a) HILE and (b) LILE. – · –, $\boldsymbol{v}_1$; – – –, $\boldsymbol{v}_2$; ——, $\boldsymbol{v}_3$; •, $\boldsymbol{\omega}$.

directions of the rate-of-strain tensor, which determines the sign and intensity of the production term.

We unfold $-\delta u_i S_{ij} \delta u_j$ in the projection of $\delta\boldsymbol{u}(\boldsymbol{x}, t)$ into each of the three eigenvectors of the rate-of-strain tensor, denoted by $\boldsymbol{v}_1$, $\boldsymbol{v}_2$ and $\boldsymbol{v}_3$, leading to

$$-\delta u_i S_{ij} \delta u_j = -2\Lambda(\alpha_1 \cos^2(\theta_1) + \alpha_2 \cos^2(\theta_2) + \alpha_3 \cos^2(\theta_3)), \tag{5.20}$$

where $\alpha_1 > \alpha_2 > \alpha_3$ are the eigenvalues of the respective eigenvectors and θ_1, θ_2 and θ_3 are the angles of $\delta\boldsymbol{u}(\boldsymbol{x}, t)$ with $\boldsymbol{v}_1, \boldsymbol{v}_2$ and $\boldsymbol{v}_3$. This analysis is similar to the analysis of the alignment between the vorticity vector and the eigenvalues of the rate-of-strain tensor [134].

Figure 5.8(a,b) shows the probability density functions of θ_1, θ_2 and θ_3 for the inertial LEs. We observe a clear alignment of $\delta\boldsymbol{u}^+(\boldsymbol{x}, t)$ with the most contracting direction, $\boldsymbol{v}_3$. Results also show that $\delta\boldsymbol{u}^+(\boldsymbol{x}, t)$ and $\delta\boldsymbol{u}^-(\boldsymbol{x}, t)$ are predominantly configured perpendicular to $\boldsymbol{v}_1$ and to $\boldsymbol{v}_3$ respectively. There is no significant alignment of the perturbation field with the intermediate eigenvector, $\boldsymbol{v}_2$, or with the vorticity vector. The alignment of $\delta\boldsymbol{u}^\pm$ with the filtered vorticity vector at different scales has been computed to discard potential interscale alignment, such as that present between vorticity and the rate-of-strain tensor at different scales [41, 108].

From incompressibility follows that $\alpha_1 + \alpha_2 + \alpha_3 = 0$, and the relative magnitude between α_1 and α_3 is given by the sign of the intermediate eigenvalue α_2. Positive α_2

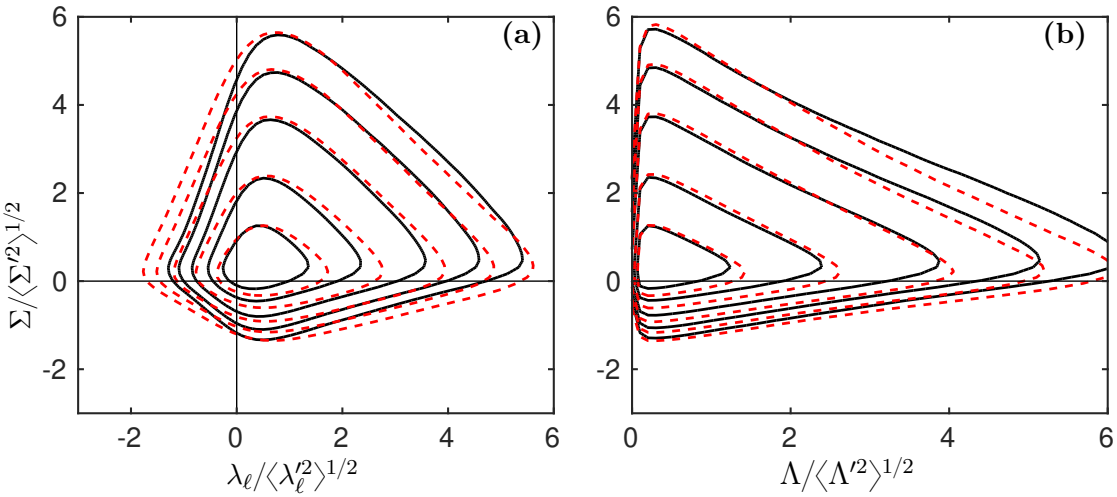

Figure 5.9: Joint probability density of the local energy transfer $\Sigma = \tau_{ij}S_{ij}$ at scale Δ_λ and: (a) the local amplification rate λ_ℓ; (b) the energy of the LV, Λ, for: ——, HILE; – – –, LILE. Contours at 0.9, 0.5, 0.1, 0.05 and 0.01 of the maximum of the probability distribution.

implies that $|\alpha_3| > |\alpha_1|$, while when $\alpha_2 < 0$ leads to $|\alpha_1| > |\alpha_3|$. We expect strong positive events of λ_ℓ for the HILE to take place near configurations of the rate-of-strain tensor with $\alpha_2 > 0$. This is the case as shown in figure (5.6), where intense λ_ℓ is located in the Vieillefosse tail. Furthermore, we find that the average of λ_ℓ conditioned to $\alpha_2 > 0$ is three times larger than in regions where $\alpha_2 < 0$. Conversely, events of the λ_ℓ for the LILE should be stronger when $\alpha_2 < 0$, but the average of λ_ℓ is approximately similar whether conditioned to sign of α_2 or not.

5.6.5 The local amplification rate and the energy fluxes

The conditional probability of λ_ℓ in the Q–R plane resembles the one found for the local energy fluxes in physical space, shown by figure 4.4(a). Most of the intense events of Σ and λ_ℓ are located in the Vieillefosse tail, where strain and strain auto-amplification is dominant over enstrophy and vortex stretching. The connection between energy fluxes and phase-space mixing, as described in §2, suggest that there might be some local correlation between λ_ℓ or Λ, and Σ. In figure 5.9(a,b), we display the joint probability density function of Σ with λ_ℓ, and of Σ and Λ, which shows that these fields are not strongly correlated. The correlation coefficient, defined in (3.18), between λ_ℓ, or Λ, and Σ are low, $\mathcal{S}_{\Sigma,\lambda_\ell} = 0.25$ and $\mathcal{S}_{\Sigma,\Lambda} = 0.163$. This is probably a consequence of considering

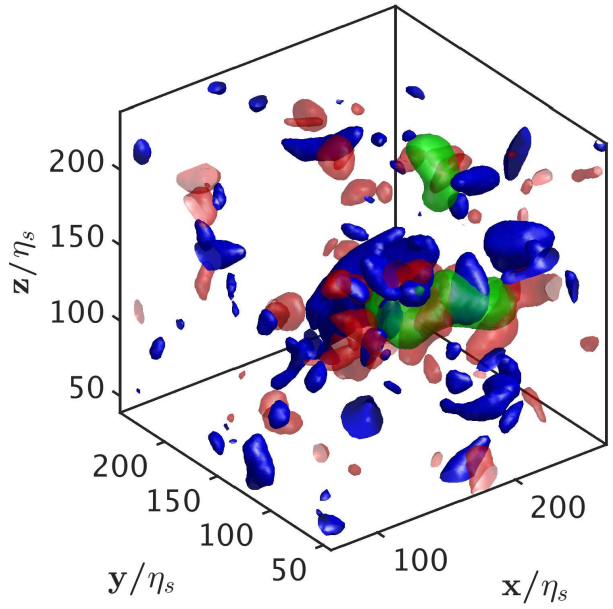

Figure 5.10: Visualisation of the field of intense λ_ℓ. Isosurfaces of: (blue) intense vortical regions, $\check{Q}/\langle\check{Q}^2\rangle^{1/2} = 2\check{R}/\langle\check{Q}^2\rangle^{3/2} + 2$; (red) intense strain, $\check{Q}/\langle\check{Q}^2\rangle^{1/2} = 2\check{R}/\langle\check{Q}^2\rangle^{3/2} - 2$; (green) intense amplification of the HILE, $\lambda_\ell(\boldsymbol{x}) > 8\langle\lambda_\ell\rangle$.

only the extreme LEs, which are not able to cover all the chaotic events in the spatial coordinates. We expect this analysis to yield more complete results when more LEs are available.

5.6.6 Conditional 3D statistics of intense local amplification events

Visualisation of structures of strong velocity gradients and of high positive λ_ℓ suggest that intense amplification events take place in regions where structures of intense strain and intense enstrophy interact closely. An example of this type of configuration is displayed in figure 5.10, where an intense amplification event develops close to a knot of intense gradients formed by structures from the Vieillefosse tail and from the $Q > 0$ and $R < 0$ quadrant. In this section we will show that, although intense λ_ℓ is not locally related to the dynamics of the vorticity vector, it is non-locally connected to the dynamics of stretched vortices.

We characterise the structures that originate strong amplification events of λ_ℓ by considering 3D averages of relevant turbulent quantities conditioned to the intense maxima

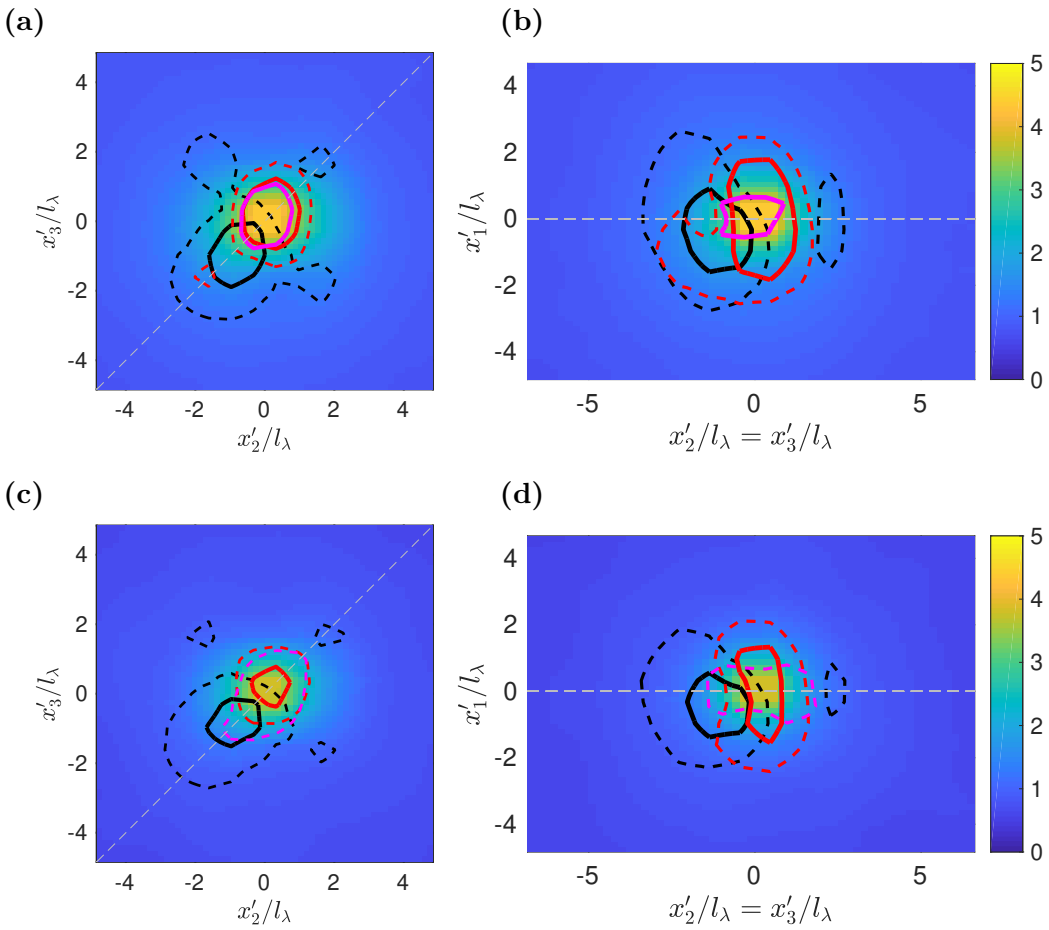

Figure 5.11: Conditional 3D average of enstrophy, strain and energy transfer around maxima of λ_ℓ, where $\lambda_\ell > 4\langle\lambda\rangle$, for the (a,b) HILE and (c,d) LILE. Views of plane (a,c) $x_1' = 0$ and of plane (b, d) $x_2' - x'3 = 0$. Color field corresponds to $\langle\lambda_\ell\rangle_m$ normalised with $\langle\lambda_\ell\rangle$. Isocontours correspond to: ——— $\langle|\tilde{\omega}|\rangle_m = 1.5\langle|\tilde{\omega}|\rangle$; – – – $\langle|\tilde{\omega}|\rangle_m = 1.2\langle|\tilde{\omega}|\rangle$; ——— $\langle\Sigma\rangle_m = 2.4\langle\Sigma\rangle$; – – – $\langle\Sigma\rangle_m = 1.7\langle\Sigma\rangle$; ——— $\langle|\check{S}|\rangle_m = 1.4\langle|\check{S}|\rangle$; – – – $\langle|\check{S}|\rangle_m = 1.2\langle|\check{S}|\rangle$.

of the λ_ℓ field. This approach has been previously used to characterise the dynamics of turbulent flows [133, 135, 136].

The procedure used to obtain 3D averages is as follows. First, we find all the local maxima of λ_ℓ in different flow fields of the ensemble, and select those local maxima at which $\lambda_\ell > \beta\langle\lambda\rangle$, where β is a threshold. The spatial coordinates of the maxima is denoted by $\boldsymbol{x}_m$. The maxima are defined as points where λ_ℓ is larger than in any of the surrounding points in the mesh. We have checked that λ_ℓ is sufficiently smooth for this approach to yield appropriate results. Second, we calculate relevant turbulent quantities around each maximum, and extract these fields to perform a 3D average considering the local maxima as the origin of spatial coordinates, such that the spatial coordinates for the average are $\boldsymbol{x}' = \boldsymbol{x} - \boldsymbol{x}_m$. The conditional 3D average of a turbulent quantity, ϕ,

around the set of maxima is denoted by $\langle\phi\rangle_m(\boldsymbol{x}')$.

Due to the statistical isotropy of the flow field, the resulting average field is also isotropic. In order to orient the extracted fields prior to averaging, we use the three eigenvalues of the rate-of-strain tensor, $\boldsymbol{v}_i$, at $\boldsymbol{x}_m$. This election of the reference frame is supported on the strong connections between λ_ℓ and the rate-of-strain tensor. Since we are analysing λ_ℓ in the inertial scales, we consider the filtered rate-of-strain tensor at scale $\check{\Delta} = \Delta_\lambda = 25\eta_s$. We orient the extracted fields before averaging by rotating them around the origin, such that x_1' corresponds to the direction of the most stretching eigenvector, $\boldsymbol{v}_1$, and x_3' to the direction of the most compressing eigenvector, $\boldsymbol{v}_3$. This configuration automatically satisfies that x_2' corresponds to the direction of the intermediate eigenvector. This arrangement, however, is still symmetric with respect to the three planes perpendicular to the principal directions. In order to remove this symmetry, the extracted fields are reflected in each direction so that the maxima of the enstrophy of each field is located in the $x_1' < 0, x_2' < 0$ and $x_3' < 0$ octant of the average field. To avoid considering maxima which are far away from the origin, which are unrelated to the dynamics of the local maxima of λ_ℓ, we weigh the enstrophy field with a Gaussian function, $\mathcal{G}(\boldsymbol{x}') = \exp(-|x'|^2/\varphi\check{\Delta}^2)$, where φ is a parameter that sets the width of the Gaussian. We only apply this weight to find the maxima of the enstrophy, but not for averaging. We have checked that the results obtained using this procedure do not depend strongly on φ for values of φ of order unity, and choose $\varphi = 2$.

The conditional statistics have been constructed from 100 fields, each extracted from a different realisation of the ensemble at a fixed time, $t - t_0 = 0.9T_0$ for the HILE, and $t - t_{inv} = 0.9T_0$ for the LILE. From these fields we have extracted approximately 3000 different maxima of λ_ℓ for each LE, which fulfil that $\lambda_\ell > 4\langle\lambda_\ell\rangle$. The qualitative picture is similar for higher threshold of λ_ℓ. Results show that this number of individual maxima is enough to converge the conditional statistics.

We have calculated the conditional 3D average of the intensity of the vorticity vector, $\langle|\omega|\rangle_m(\boldsymbol{x}')$, of the intensity of the rate-of-strain tensor, $\langle|\check{S}|\rangle_m(\boldsymbol{x}')$, and of the energy transfer in physical space, $\langle\Sigma\rangle_m(\boldsymbol{x}')$. The 3D structure of these conditional-averaged quantities for the HILE and LILE are shown in figure 5.11(a-d). In figure 5.11(a,d) we show a cut normal to $\boldsymbol{v}_1$, at $x_1' = 0$, and in figure 5.11(b,c) a cut in the plane $x_3' = x_2'$. For both LEs, we observe that the maxima of the conditional-averaged strain and energy

transfer are located in the centre of the volume, where, by construction, we also find the maxima of $\langle \lambda_\ell \rangle_m$.

Around the origin, we identify the presence of average vortical structures characterised by a value of $\langle |\check{\omega}| \rangle_m$ larger than the average. We observe a large vortex with three smaller, weaker vortices located in the surroundings of intense conditional-averaged strain. These vortical structures are located 45° from $\boldsymbol{v}_2$ and $\boldsymbol{v}_3$. While the strongest vortex is imposed by the reflection operation applied to remove symmetries, the appearance of the weaker vortices is not trivial and suggest that intense events of λ_ℓ are a product of the close interaction of a strong vortex with, at least, a weaker vortex.

The average quantities around the maxima of λ_ℓ are higher for the HILE than for the LILE. The maxima of the conditional averages are $\langle |\check{\omega}| \rangle_m^{max} = 1.8 \langle |\check{\omega}| \rangle$, $\langle \check{S} \rangle_m^{max} = 1.5 \langle \check{S} \rangle$ and $\langle \Sigma \rangle_m^{max} = 2.7 \langle \Sigma \rangle$ for the HILE, and $\langle |\check{\omega}| \rangle_m^{max} = 1.6 \langle |\check{\omega}| \rangle$, $\langle \check{S} \rangle_m^{max} = 1.4 \langle \check{S} \rangle$ and $\langle \Sigma \rangle_m^{max} = 2.0 \langle \Sigma \rangle$ for the LILE. The low values of $\langle S \rangle_m$ and of $\langle |\check{\omega}| \rangle_m$ suggests that intense events λ_ℓ often take place in regions where either the strain or the enstrophy are not substantially larger than the average, but where both quantities are segregated. This picture is consistent with the conditional averages of λ_ℓ in the Q-R space, and indicates that, not only the magnitude of the strain, but also the orientation of $\delta \boldsymbol{u}$ with respect to the rate-of-strain tensor determines the space-local amplification of the LV. The similarities in the conditional averages obtained for both LEs suggest that the fundamental difference between the local amplification of the HILE and LILE resides in the local orientation of the perturbation field with respect to the rate-of-strain tensor, as shown in §5.5.

Chapter 6

Discussion and conclusions

In this chapter, we summarise and discuss the original results presented in this work, and their future implications for the characterisation of the energy cascade.

This thesis hinges on a reversible turbulence system constructed using a reversible LES model for the sub-grid stresses. In this system, the transformation $\boldsymbol{u} \to -\boldsymbol{u}$ is equivalent to $t \to -t$, and changing the sign of the velocity field leads to inverse turbulent evolutions which display a sustained inverse energy cascade towards the large scales.

6.1 The conservative nature of the energy cascade

Throughout this thesis, we have presented strong evidences of the nature of the energy cascade as a conservative, volume-preserving process in phase space, in which the breaking of the temporal symmetry, i.e the 'arrow of time', is not a consequence of the dissipation.

In §3.2, we have conducted different experiments on reversible LES turbulence. In particular, we have shown that the sustained inverse cascade in the inverse evolutions is a consequence of inertial mechanisms only, while the SGS model acts as a necessary source of energy. By reversing the energy cascade of a system with an irreversible SGS model, we have proven that microscopic reversibility is a fundamental property of inertial dynamics, regardless of the particular nature of the dissipative mechanisms. This experiment proves that our conclusions are applicable to the inertial range of fully developed turbulence,

and offers further evidence of the similarities between the behaviour of the NS equations in the inertial range and the Euler equations.

In §5.4, we have analysed the Lyapunov structure of the inertial range by restricting the calculation of the LEs to modes where inertial forces are dominant. Results show that when inertial mechanisms are isolated, the most positive and most negative LEs have similar absolute value. These results suggest a potential symmetry of the Lyapunov spectrum in the inertial scales, which is characteristic of Hamiltonian systems. The inverse and direct cascades are effectively driven by microscopically time-reversible dynamics, and the inertial range behaves as a conservative out-of-equilibrium Hamiltonian system, which preserves phase-space volume.

A similar procedure as the one used to calculate the inertial Lyapunov exponents might be used to obtain partial Lyapunov spectra in fully developed turbulence. By conveniently choosing and varying the number and distribution of the targeted degrees of freedom, it could be possible to obtain novel information to characterise chaos and predictability in the energy cascade. We suggest that these partial spectra could be used to, at least approximately, reconstruct the complete Lyapunov spectrum of fully developed turbulence, allowing to further test the Hamiltonian structure of the inertial range.

6.2 The attractor *vs* the antiattractor

Reversible turbulence provides access by a change in the sign of the velocities to the antiattractor, which is composed of the set of turbulent states in the attractor with inverse sign. The analysis of phase-space trajectories in the attractor and antiattractor serves to characterise and explain the origin of the time-symmetry breaking and the prevalence of direct energy cascades.

6.2.1 Time-symmetry breaking in phase space

In §3.3.1, we have characterised the distribution of inverse trajectories in phase space. By perturbing inverse phase-space trajectories within the antiattractor, we have shown that inverse evolutions exist in a wide region of phase-space, and that they lie separated

from the direct evolutions. The perturbed inverse phase-space trajectories diverge from the original trajectories due to the chaotic nature of the system, and eventually evolve towards the turbulent attractor, which is composed almost exclusively by trajectories with a direct energy cascade.

These experiments prove that the antiattractor is 'unstable' and that inverse cascades can only be observed for a finite time. Moreover, the fluctuations of the spatially-averaged sub-grid dissipation in the turbulent attractor are much smaller than the phase-space average, indicating that there is a extremely low probability that the system spontaneously escapes the attractor and develops an average inverse cascade.

In §5.2 we have shown that the absolute value of the most negative LE is larger that the value of the most positive LE, $|\lambda^-| > |\lambda^+|$, which reflects the contraction of phase-space volume due to the dissipative nature of the system. The direct trajectories are less repelling than the inverse trajectories, and, therefore, we might expect the system to spend longer times close to a direct than to an inverse trajectory. In the formalism of the fluctuation relations, Evans and Searles [76] used a similar argument to justify the low probability of inverse trajectories in reversible dissipative systems.

6.2.2 Time-symmetry breaking in physical space

In the spirit of the local formulation of the fluctuation relations [104], we have traced the low probability of inverse phase-space trajectories to the low probability of intense backscatter events. We have estimated the probability of inverse cascades by using the statistics of volume-averaged space-local energy transfer events. We quantify the probability of direct over inverse cascades using the asymmetry function $\mathcal{P}$ to quantify the probability of observing a direct cascade in a volume V, over the probability of observing an inverse cascade over the same volume.

In the range of large volume sizes, $V \sim L^3$, in which volume-averaged inverse fluxes are observable, we find that $\log \mathcal{P} \sim \mathcal{N}$, where $\mathcal{N}$ is a measure of the number of independent energy transfer events consider in the volume average. Although we have proved that the statistical distribution of the addition of decorrelated energy transfer events approaches a normal distribution around the mean, $\log \mathcal{P}$ is dominated by the negative tails of the probability distribution of the locally-averaged energy fluxes, which remain non-Gaussian

even for large averaging volumes. This strong non-Gaussianity is a consequence of the multiscale nature of the cascade process, as illustrated by simple cascade models [21, 106], and precludes the direct application of local versions of the fluctuation relations to predict energy backscatter. Neither are the global fluctuation relations of any use: turbulence is too far from equilibrium.

Supported on the physical-space locality of the cascade reported in §3.3, we have explained the low probability of inverse cascades by, first, identifying the mechanisms responsible for ineverse energy transfer, and, by, second, justifying their negligible probability. In §4.3.1, we have shown that, in the antiattractor and in the transition from the antiattractor to the attractor, intense inverse energy transfer events occur in regions where the strain is dominant over the enstrophy, and where the rate-of-strain tensor has a jet topology, i.e one positive, and two negative eigenvalues. This configuration corresponds to topologies in the antitail of the Q–R space, which have negligible probability within the attractor. The conditional mean trajectories in the Q–R space show that the low probability of topologies in the antitail is a consequence of the inability of the non-local component of the pressure Hessian to counteract the restricted Euler dynamics.

In view of these results, we propose that the low probability of inverse cascades is a consequence of the negligible probability of topologies in the antitail, and suggest an entropic argument to explain this fact. The generation of topologies along the Vieillefosse tail is encoded in the point-wise interaction of the velocity gradients and is strictly local. Any possible organisation of the vorticity vector and the rate-of-strain tensor will generate topologies in the Vieillefosse tail under the action of the RE dynamics. On the other hand, the formation and sustenance of the antitail requires the global action of the non-local component of the pressure Hessian to generate intense strain with a negative intermediate eigenvalue. Due to non-locality, the dynamics of the pressure Hessian depend on a large number of degrees of freedom. While the dynamics of any flow field, even random fields, lead to the generation of a Vieillefosse tail due to RE dynamics, only very special flow fields are sufficiently organised so as to counteract the RE dynamics and form an antitail. This argument would explain, not only why the direct energy cascade in the attractor is more probable than the inverse energy cascade in the antiattractor, but why, in general, direct cascades are more probable than inverse cascades.

6.3 The energy cascade in physical space

6.3.1 Locality of the energy cascade in physical space

In order to connect the statistical formalism of phase space with the dynamics of the energy cascade, we have started by studying the spatial structure of the local energy fluxes in physical space in §3.3.

We have shown that the local energy fluxes have a finite correlation length, which scales with the filter width. The statistical behaviour of the volume average of the energy transfer field indicates that the cascade is an approximately local process in physical space, which complies well with the classical picture proposed by Richardson [8], and the recent work of Cardesa et al. [28].

In this analysis, we have also dealt with the arbitrariness of the energy fluxes, proving that the direct energy cascade is, on an a locally average sense, robust to two different definition of the fluxes. We have studied Σ and Ψ, which differ by the divergence of a flux in physical space and have equal spatial average, $\langle\Sigma\rangle = \langle\Psi\rangle$. Although locally very different, both quantities are strongly correlated when volume-averaged over volumes of their correlation length cubed. These results suggest that the differences between both definitions are highly local, and that both markers are reasonable quantifiers of the intensity of the cascade in a local average sense.

We have only tested two different definitions of the energy fluxes, and further research is necessary to determine whether better definitions are possible, and whether these definitions provide different insights into the dynamics of the cascade. In view of these results, we hypothesise that, although differences might be arbitrarily large on a strictly local sense, they should not be on a locally average sense.

This analysis is of special relevance for some LES tools, which model the sub-grid stresses to reproduce the energy fluxes across the cutoff scale. Although the correlation between the modelled sub-grid stresses and the *a priori* stresses is known to be quite low, at least for the classical Smagorinsky model [30, 137], these models predict well the energy spectrum and the dissipation rate in decaying homogeneous turbulence [98, 138]. This is probably a consequence of the indeterminacy of fluxes: it is possible to find

infinitely many different representations of the sub-grid stresses which yield a similar local sub-grid dissipation.

6.3.2 Is backscatter dynamically relevant for the cascade?

A relevant difference between Σ and Ψ is the frequency and intensity of backscatter events, which are stronger and more probable for Ψ than for Σ. When we apply a volume-average operation, the differences between both markers in the probability and intensity of backscatter events are greatly diminished. This seems to be a consequence of the significant reduction of backscatter events after the volume-averaging operation.

The correlation between the local energy fluxes at scales separated by a factor of 2 is significant and decreases when scales are separated by a factor of 4, corroborating the reported scale locality of the cascade [28, 139–141]. When conditioning these correlations to the local direction of the cascade, we find that they are equally strong for direct energy fluxes. However, we find that for backscatter this correlations are weak even between scales separated by a factor of 2.

Backscatter is highly local in scale, and strongly depends on the definition of the fluxes. This phenomenon seems not a consequence of interscale interactions, as the direct cascade, but rather of strictly scale-local dynamics.

This picture suggest that the dynamical significance of backscatter to the energy cascade is limited. Evidences are again provided by the good agreement between LESs and DNSs, despite the inability of available sub-grid model to reproduce backscatter. Although the present work strongly emphasises the bidirectionality of the cascade, our results indicate that turbulent flows are sufficiently far from equilibrium as to preclude the observation of local inverse cascades.

This might not be the case under different conditions, such as in wall-bounded flows, where the energy containing-scales are larger than the energy-producing scales, and backscatter must exist to feed the former [142]. Our results suggests that this average inverse cascade could be related to the presence of strong anisotropies in these flows.

6.4 The structure of the inertial range and the energy cascade

6.4.1 The rate-of-strain tensor as a marker of statistical irreversibility

We have compared the structure of the direct and inverse cascades through the study of the invariants of the filtered velocity gradient tensor, Q and R, and its conditional mean trajectories (CMTs). We find that the statistics of Q and R differ substantially from direct evolutions in the attractor, to inverse evolutions in the antiattractor. At variance with the classical teardrop shape, Q and R form an inverse teardrop in the inverse evolutions, with dominant vortex compression in $Q > 0$ and an 'antitail' in $Q < 0$.

We have quantified these differences using an asymmetry function in the Q–R plane, which reveals that most of the asymmetry between the structure of the attractor and the structure of the antiattractor is reflected in the $Q < 0$ semiplane. These results suggest an important connection between the structure of the rate-of-strain tensor, and the direction of the system in time. In the attractor, the rate-of-strain tensor has predominantly one negative and two positive eigenvalues (layer topology), while in the antiattractor, it has two negative and one positive eigenvalues (jet topology). Intense events of the rate-of-strain tensor with these topologies are not shared between the two cascades. On the other hand, it is more challenging to distinguish the inverse from the direct cascade by fixing on the statistics of regions where enstrophy is dominant over the strain: vortex stretching and compression in enstrophy dominated regions are common in both the attractor and antiattractor.

These results emphasise the importance of the rate-of-strain tensor in the dynamics of the energy cascade. We have shown that a change in the sign of the velocity field is much more relevant to the dynamics of the system in regions where the strain is dominant than in regions where vorticity is dominant. A change in the sign of vorticity only changes the sense of rotation of a vortex but not its fundamental dynamics, as illustrated for instance in the Burgers [143]'s model. On the other hand, a change in the sign of the rate-of-strain tensor has fundamental implications, as it reverses the evolution of both the enstrophy and the strain in the inviscid case. The different nature of the rate-of-strain tensor and the vorticity vector is evident in the evolution equations of the strain and the enstrophy, (4.3, 4.4), which are odd with the former and even with the latter.

However, we must consider that the two quantities are not independent, and that changing the sign of the vorticity changes the sign of the strain, and *vice versa*. Both quantities are strongly coupled through kinematic relations [144], and must be consider simultaneously, but it is the rate-of-strain tensor that reflects most of the statistical irreversibility of turbulent flows. If we were a local observer in the inertial scales of turbulence, and we were to establish the space-local direction of the energy fluxes, we should focus on the dynamics of regions where the filtered rate-of-strain tensor is dominant, rather than on the dynamics of regions where the filtered vorticity vector is dominant.

6.4.2 The direct and inverse cascades and the geometry of the rate-of-strain tensor

On §4.3 we have studied the statistical correlation between the local energy fluxes and the local topology of the flow by using conditional statistics in the Q–R space. This analysis shows that the direction and intensity of the local energy fluxes are strongly related to the dynamics of the filtered rate-of-strain tensor.

First, we have analysed inverse phase-space trajectories which evolve from the antiattractor to the attractor. The transition from an average inverse to an average direct cascade is marked by the disappearance of the anti-tail, and the appearance of a regular Vieillefosse tail. The statistics of enstrophy-dominated regions seem to remain unaltered in this transition. While an average inverse energy cascade holds, the antitail is responsible for most inverse energy transfer, both in the antiattractor, and in the transition to the attractor.

The strong connection between the structure of the flow in strain-dominated regions and the energy cascade is also supported by the same analysis in the attractor. Conditional statistics show that the most intense energy transfer events are participated by structures in the Vieillefosse tail, and these structures contribute the most to the total energy fluxes.

In the turbulent attractor, the intensity of backscatter does not depend strongly on the underlying structure of the filtered velocity gradients, but most energy backscatter takes place in regions where vorticity and vortex compression are dominant. These events are

much weaker than inverse energy transfer events in the antiattractor, which are related to the structures in the antitail.

6.4.3 The rate-of-strain tensor as a source of entropy and chaos

In §5.5, we have used the Lyapunov vectors (LV), which are complete flow fields, to derive a local measure of chaos and entropy production in physical space. We have decomposed the Lyapunov exponents into the spatial and temporal average of a scalar field, the local amplification rate λ_ℓ, and used the evolution equation of the energy of the perturbations in physical space to obtain a meaningful expression for this quantity. This field, when correlated with the features of the main flow, provides information on the events that lead to the amplification of the LV, and ultimately to the production of chaos and phase-space mixing. We have applied this analysis to the LEs calculated in the inertial scales.

The analysis of the spatial structure of λ_ℓ, for the highest inertial Lyapunov exponent (HILE) and the lowest inertial Lyapunov exponent (LILE), reveals that it is highly intermittent, and that it is consentrated in particular regions of the flow. This is a strong evidence that chaos is not homogeneously distributed in the spatial coordinates, but that some turbulent events are more chaotic than others. This is also true for the least chaotic or more 'contractive' events.

In order to identify these events, we have studied the statistics of λ_ℓ in the inertial scales conditioned to, first, Q and R of the filtered velocity gradients, and, second, to strain auto-amplification and vortex stretching of the filtered gradients. Intense values of λ_ℓ for the HILE and LILE are mostly located in the Vieillefosse tail, where the strain is dominant over the vorticity, and correlate strongly with intense strain. These results indicate that the rate-of-strain tensor is not only a maker, but also a generator of statistical irreversibility. While the local amplification rate of the HILE is related to the production of strain through strain auto-amplification, the LILE is not related to a particular sign of the strain auto-amplification. Although we also observe some contribution of vorticity-dominated regions to the total amplification rate in both exponents, this contribution is weaker than that of the strain-dominated regions.

The most chaotic events take place in regions where the rate-of-strain is intense and has a positive intermediate eigenvalue. There is a predominant alignment of the perturbation field in physical space with the most compressing eigenvector of the rate-of-strain tensor, indicating that the generation of chaos and phase-space mixing seems to be related with the formation layers by the most compressive eigenvector of the rate-of-strain tensor. The least chaotic or most contractive events are also related to the presence of strong strain, but are a consequence of the stretching of the perturbation field by the stretching eigenvectors of the rate-of-strain tensor. No preferred configuration of the rate-of-strain tensor is observed in these events.

The rate-of-strain tensor appears as a fundamental generator of intense chaos in the inertial scales. Surprisingly, it is also responsible for phase-space contraction. These results are in agreement with studies that emphasise the role of the rate-of-strain in turbulence dynamics [42, 144], and suggest that the role of vorticity in the dynamics of the energy cascade is probably overestimated. In view of these results, it seems adventurous to claim that vortex stretching has a central role in the turbulence cascade, without regarding the strain auto-amplification.

6.4.4 The essential role of coherent vortices

The strong kinematic coupling between the rate-of-strain tensor and the vorticity vector advise us against considering the former as the only source of irreversibility, chaos and energy cascades. We have complemented our analysis by considering the 3D statistics of the enstrophy, the strain and the energy transfer conditioned to intense events of λ_ℓ for the HILE and LILE. This analysis reveals an essential but nonlocal role of coherent vortices in the generation of chaos.

Results indicate that strong events of λ_ℓ for the HILE and LILE take place in the vicinity of strong vortices, which interact with weaker vortices. The organisation of the conditional average enstrophy around λ_ℓ is consistent with a stretched strong vortex interacting with one weaker co-rotating vortex and two weaker counter-rotating vortices. The conditional 3D structure of intense strain and direct energy transfer overlap the structure of intense amplification rate. These results indicate that the nonlocal interaction between the filtered rate-of-strain and the filtered vorticity plays an important role in the dynamics of the energy cascade.

6.5 New perspectives on the turbulent energy cascade

6.5.1 Implications of the entropy-driven turbulent cascade

The implications of the experiments on reversible turbulence that are presented in this thesis are manifold. The most immediate one, but not obvious, is that, so far, our knowledge of the Navier–Stokes equations alone do not seem enough to explain the macroscopic evolutions of turbulent flows.

The set of laws that govern turbulent flows operate in general over an arbitrarily large number of degrees of freedom, allowing for an overwhelmingly large number of possible trajectories and states. These laws impose only a few constrains on the system, being the conservation of mass and momentum the most immediate ones. Despite the lack of constrains, turbulent flows seem to recurrently reproduce the same organised structure common to the states within the turbulent attractor.

Turbulence research relies on the study of flows which are inside the attractor, mostly because the convergence to the attractor seems an unavoidable consequence of the dynamics. The novel approach of this work is to study backwards-evolved turbulent flows, which represent phase-space trajectories outside the turbulent attractor. Although these phase-space trajectories are not accessible from almost any initial conditions, the process to obtain such trajectories is quite simple: the equations of motion are run forward in time and then reversed. Access to these inverse evolutions has proved useful to determine the causes for the prevalence of direct energy transfer over inverse energy transfer, and for identifying mechanisms responsible for entropy production in the energy cascade.

The most intriguing question is whether there are ‘turbulent’ trajectories outside the attractor other than the backward-evolved flow fields. The study of these inverse evolutions provide information on why direct cascades in the attractor are more probable that inverse cascades in the antiattractor. However our analysis does not elucidate why cascades within the turbulent attractor are more probable than the rest of possible direct cascades.

6.5.2 Searching for strange cascades outside the turbulent attractor

We hypothesise that it might be possible to access these 'alternative' cascades by means of computationally intensive methods. These 'strange' cascades would provide, by direct comparison with the energy cascade in the turbulent attractor, arguments to explain the origin of the characteristic properties of turbulent flows, and data to test the existence of probabilistic principles in the selection of turbulent states. These data would serve to elucidate whether these principles are related to any variational principle, or to any particular definition of entropy.

Finding strange trajectories outside the turbulent attractor seems in principle an overwhelming task. This search opposes the robust chaotic nature of turbulence, and is complicated by the large number of degrees of freedom necessary to represent turbulent flows. We propose procedures for finding strange trajectories similar to the variational methods used for finding extremal states [145], or optimal non-linear perturbations [146], which allow the search of states and trajectories that maximise a prescribed macroscopic observable. We also propose the use of non-linear solvers, such as the Newton-Krylov methods, to find trajectories with a prescribed value of an average macroscopic quantity. We expect that, by guiding the search of trajectories imposing a given value of a macroscopic quantity, or searching for maxima and minima of this quantity, we will be able to locate trajectories that escape the turbulent attractor, where these macroscopic averages have a characteristic mean value, and fluctuations are much smaller than the mean value.

Although these methods are computationally intensive even for marginally turbulent flows, enough computational resources are now available in highly efficient GPUs devices, which have already been used in dynamical-system problems with outstanding results [147]. The exceptional performance of these devices pave the way for new procedures to directly test non-equilibrium hypothesis by probing the phase space of complex systems, thus extending the field of computational statistical mechanics [148] to realistic, highly-dimensional systems.

6.5.3 Towards a time- and space-local definition of chaos and coherence

Coherent structures represent an essential feature of many dynamical systems out of equilibrium, including turbulence. Since the early observations by Brown and Roshko [149], these structures have been recognised as important objects in turbulence dynamics, and their study has generated an extensive literature within turbulence research. These structures represent perhaps our best chance to understand and control the dynamics of turbulence, as they embody order generated from chaos, and emerge as manageable and solid objects in the apparently disorganised and intractable set of turbulent motions.

These structures are related to efficient transport of turbulent quantities, such as energy or momentum, and their organised motion suggest that the effective number of degrees of freedom needed to represent the dynamics of turbulence is much smaller than usually required in DNSs. Dimensional reducibility makes efforts towards reduced representations of turbulence flows, such as LES techniques, conceivable.

Despite the dynamical relevance of coherent structures, their definition and, consequently, their identification, is ambiguous, and relies on approaches with little dynamical content. A typical procedure is to identify coherent structures as joint regions of space where a particular turbulent quantity is intense [150]. It is assumed without further scrutiny that intense structures are necessarily coherent structures, but dynamical information on the evolution of the flow is strictly necessary to tag a structure as coherent.

In this work, we have used the local amplification rate, λ_ℓ, to identify the mechanisms responsible for phase-space mixing. This quantity is also a local measure of chaos, which intuitively represents the opposite of order and coherence. We propose that a similar methodology can be used to quantify the degree of coherence and chaos of different regions of turbulent flows. Negative or low local values of λ_ℓ, or a similar quantity, should indicate a high probability that that particular region of the flow field remains unperturbed, i.e coherent, over time. On the other hand, high positive values of λ_ℓ are representative of chaos-generating regions, which are expected to change over times of the order of $1/|\lambda_\ell|$. A different approach is to modify the algorithm used to calculate λ_ℓ to track desired regions of the flow field where quantities of interest are intense. This procedure would allow, for instance, to quantify the coherence of intense vortices.

Bibliography

[1] M. Lesieur. *Turbulence in fluids: stochastic and numerical modelling.* Nijhoff Boston, MA, 1987.

[2] S. B. Pope. Turbulent flows, 2001.

[3] U. Frisch. *Turbulence: the legacy of AN Kolmogorov.* Cambridge university press, 1995.

[4] A. Tsinober. *Essence of turbulence as a physical phenomenon.* Springer, 2019.

[5] R. Devaney. *An introduction to chaotic dynamical systems.* CRC Press, 2018.

[6] D. Chandler. *Introduction to modern statistical mechanics.* 1987.

[7] A. Tsinober. *An informal introduction to turbulence.* Springer Science & Business Media, 2001.

[8] L. F. Richardson. *Weather prediction by numerical process.* Cambridge University Press, 1922.

[9] A. N. Kolmogorov. The local structure of turbulence in incompressible viscous fluid for very large Reynolds numbers. *Dokl. Akad. Nauk. SSSR*, 30:9–13, 1941.

[10] A. N. Kolmogorov. Dissipation of energy in the locally isotropic turbulence. *Dokl. Akad. Nauk. SSSR*, 32:16–18, 1941.

[11] G. Boffetta and G. P. Romano. Structure functions and energy dissipation dependence on reynolds number. *Phys. Fluids*, 14:3453–3458, 2002.

[12] Y. Kaneda, T. Ishihara, M. Yokokawa, K. Itakura, and A. Uno. Energy dissipation rate and energy spectrum in high resolution direct numerical simulations of turbulence in a periodic box. *Phys. Fluids*, 15:L21–L24, 2003.

[13] L. Onsager. The distribution of energy in turbulence. In *Physical Review*, volume 68, pages 286–286, 1945.

[14] K. R. Sreenivasan and R. A. Antonia. The phenomenology of small-scale turbulence. *Annu. Rev. Fluid Mech.*, 29:435–472, 1997.

[15] F. H. Champagne. The fine-scale structure of the turbulent velocity field. *J. Fluid Mech.*, 86:67–108, 1978.

[16] S. G. Saddoughi and S. V. Veeravalli. Local isotropy in turbulent boundary layers at high reynolds number. *J. Fluid Mech.*, 268:333–372, 1994.

[17] J. I. Cardesa, A. Vela-Martín, S. Dong, and J. Jiménez. The temporal evolution of the energy flux across scales in homogeneous turbulence. *Phys. Fluids*, 27:111702, 2015.

[18] H. Yoshimoto and S. Goto. Self-similar clustering of inertial particles in homogeneous turbulence. *J. Fluid Mech.*, 577:275–286, 2007.

[19] S. Y. Chen, B. Dhruva, S. Kurien, K. R. Sreenivasan, and M. A. Taylor. Anomalous scaling of low-order structure functions of turbulent velocity. *J. Fluid Mech.*, 533: 183–192, 2005.

[20] U. Frisch, P. L. Sulem, and M. Nelkin. A simple dynamical model of intermittent fully developed turbulence. *J. Fluid Mech.*, 87:719–736, 1978.

[21] C. Meneveau and K. R. Sreenivasan. Simple multifractal cascade model for fully developed turbulence. *Phys. Rev. Lett.*, 59:1424, 1987.

[22] U. Frisch. From global scaling, a la kolmogorov, to local multifractal scaling in fully developed turbulence. *Proc. R. Soc.*, 434:89–99, 1991.

[23] E. D. Siggia. Numerical study of small-scale intermittency in three-dimensional turbulence. *J. Fluid Mech.*, 107:375–406, 1981.

[24] J. Jiménez, A. Wray, P. G. Saffman, and R. S. Rogallo. The structure of intense vorticity in isotropic turbulence. *J. Fluid Mech.*, 255:65–90, 1993.

[25] Y. Kaneda and T. Ishihara. High-resolution direct numerical simulation of turbulence. *J. Turbul.*, page N20, 2006.

[26] T. Ishihara, Y. Kaneda, and J. C. R. Hunt. Thin shear layers in high Reynolds number turbulence: DNS results. *Flow Turbul. Combust.*, 91:895–929, 2013.

[27] T. S. Kuhn. The structure of scientific revolutions. *Chicago and London*, 1962.

[28] J. I. Cardesa, A. Vela-Martín, and J. Jiménez. The turbulent cascade in five dimensions. *Science*, page eaan7933, 2017.

[29] C. Meneveau and T. S. Lund. On the lagrangian nature of the turbulence energy cascade. *Phys. Fluids*, 6:2820–2825, 1994.

[30] V. Borue and S. A. Orszag. Local energy flux and subgrid-scale statistics in three-dimensional turbulence. *J. Fluid Mech.*, 366:1–31, 1998.

[31] S. Cerutti and C. Meneveau. Intermittency and relative scaling of subgrid-scale energy dissipation in isotropic turbulence. *Phys. Fluids*, 10:928–937, 1998.

[32] T. Aoyama, T. Ishihara, Y. Kaneda, M. Yokokawa, K. Itakura, and A. Uno. Statistics of energy transfer in high–resolution direct numerical simulation of turbulence in a periodic box. *J. Phys. Soc. Jpn.*, 74:3202–3212, 2005.

[33] G. B. Folland and A. Sitaram. The uncertainty principle: a mathematical survey. *J. Fourier Anal. Appl.*, 3:207–238, 1997.

[34] C. Meneveau. Analysis of turbulence in the orthonormal wavelet representation. *J. Fluid Mech.*, 232:469–520, 1991.

[35] M. Farge. Wavelet transforms and their applications to turbulence. *Annu. Rev. Fluid Mech.*, 24:395–458, 1992.

[36] J. Jimenez. Optimal fluxes. *J. Fluid Mech.*, 641:497–507, 2017.

[37] T. S. Lundgren. Strained spiral vortex model for turbulent fine structure. *Phys. Fluids*, 25:2193–2203, 1982.

[38] M. P. Brenner, S. Hormoz, and A. Pumir. Potential singularity mechanism for the Euler equations. *Phys. Rev. Fluids*, 1:084503, 2016.

[39] H. Tennekes and J. L. Lumley. *A first course in turbulence*. MIT press, 1972.

[40] S. Goto. A physical mechanism of the energy cascade in homogeneous isotropic turbulence. *J. Fluid Mech.*, 605:355–366, 2008.

[41] T. Leung, N. Swaminathan, and P. A. Davidson. Geometry and interaction of structures in homogeneous isotropic turbulence. *J. Fluid Mech.*, 710:453–481, 2012.

[42] A. Tsinober. Vortex stretching versus production of strain/dissipation. *Turbulence Structure and Vortex Dynamics*, pages 164–191, 2000.

[43] A. Talamelli, F. Persiani, J. Fransson, P. H. Alfredsson, A. V. Johansson, H. M. Nagib, J.-D. Rüedi, K. R. Sreenivasan, and P. A. Monkewitz. Ciclope: a response to the need for high Reynolds number experiments. *Fluid Dyn. Res.*, 41:021407, 2009.

[44] P. Moin and K. Mahesh. Direct numerical simulation: a tool in turbulence research. *Annu. Rev. Fluid Mech.*, 30:539–578, 1998.

[45] V. Borue and S. A. Orszag. Self-similar decay of three-dimensional homogeneous turbulence with hyperviscosity. *Physs Rev. E*, 51:R856, 1995.

[46] J. Jiménez, J. C. del Alamo, and O. Flores. The large-scale dynamics of near-wall turbulence. *J. Fluid Mech.*, 505:179–199, 2004.

[47] L. Biferale, S. Musacchio, and F. Toschi. Inverse energy cascade in three-dimensional isotropic turbulence. *Phys. Rev. Lett.*, 108:164501, 2012.

[48] J. Jiménez and P. Moin. The minimal flow unit in near-wall turbulence. *J. Fluid Mech.*, 225:213–240, 1991.

[49] Y. Mizuno and J. Jiménez. Wall turbulence without walls. *J. Fluid Mech.*, 723: 429–455, 2013.

[50] K. Yoshida, J. Yamaguchi, and Y. Kaneda. Regeneration of small eddies by data assimilation in turbulence. *Phys. Rev. Lett.*, 94:014501, 2005.

[51] C. C. Lalescu, C. Meneveau, and G. L. Eyink. Synchronization of chaos in fully developed turbulence. *Phys. Rev. Lett.*, 110:084102, 2013.

[52] A. Pumir and B. I. Shraiman. Persistent small scale anisotropy in homogeneous shear flows. *Phys. Rev. Lett.*, 75:3114, 1995.

[53] X. Shen and Z. Warhaft. The anisotropy of the small scale structure in high Reynolds number ($Re_\lambda \sim 1000$) turbulent shear flow. *Phys. Fluids*, 12:2976–2989, 2000.

[54] L. Biferale and M. Vergassola. Isotropy vs anisotropy in small-scale turbulence. *Phys. Fluids*, 13:2139–2141, 2001.

[55] R. S. Rogallo. Numerical experiments in homogeneous turbulence. 1981.

[56] J. P. Eckmann and D. Ruelle. Ergodic theory of chaos and strange attractors. *Rev. Mod. Phys.*, 57:617, 1985.

[57] O. Flores, R. Pastor, and A. Vela-Martín. Wall-bounded turbulence control using Monte-Carlo approach. In *APS Meeting Abstracts*, 2019.

[58] M. Ávila and A. Vela-Martín. Single-droplet breakup in homogenous turbulence. In *17th ETC conference*, 2019.

[59] L. D. Landau and E. M. Lifshitz. *Fluid mechanics*. Pergamon, Oxford, 1959.

[60] L. Sirovich, L. Smith, and V. Yakhot. Energy spectrum of homogeneous and isotropic turbulence in far dissipation range. *Phys. Rev. Lett.*, 72:344, 1994.

[61] P. Constantin, C. Foias, O. P. Manley, and R. Temam. Determining modes and fractal dimension of turbulent flows. *J. Fluid Mech.*, 150:427–440, 1985.

[62] C. Canuto, M. Y. Hussaini, A. Quarteroni, and A. Thomas. *Spectral methods in fluid dynamics*. Springer Science & Business Media, 2012.

[63] C.E. Leith and R. H. Kraichnan. Predictability of turbulent flows. *J. Atmos. Sci.*, 29:1041–1058, 1972.

[64] Z. She and E. Jackson. Constrained Euler system for Navier–Stokes turbulence. *Phys. Rev. Lett.*, 70:1255, 1993.

[65] C. Cichowlas, P. Bonaïti, F. Debbasch, and M. Brachet. Effective dissipation and turbulence in spectrally truncated Euler flows. *Phys. Rev. Lett.*, 95:264502, 2005.

[66] D. Ruelle. What are the measure describing turbulence? *Prog. Theor. Phys. Supp.*, 64:339–345, 1978.

[67] W. T. Grandy. Time evolution in macroscopic systems. II. The entropy. *Found. Phys.*, 34:21–57, 2004.

[68] G. Nicolis and I. Prigogine. *Self-organization in nonequilibrium systems*, volume 191977. Wiley, New York, 1977.

[69] E. Bodenschatz, W. Pesch, and G. Ahlers. Recent developments in Rayleigh-Bénard convection. *Ann. Rev. Fluid Mech.*, 32(1):709–778, 2000.

[70] L. Onsager. Reciprocal relations in irreversible processes. I. *Phys. Rev.*, 37:405, 1931.

[71] A. Kleidon and R. D. Lorenz. *Non-equilibrium thermodynamics and the production of entropy: life, earth, and beyond*. Springer, 2004.

[72] P. Glansdorff and I. Prigogine. On a general evolution criterion in macroscopic physics. *Physica*, 30:351–374, 1964.

[73] R. Dewar. Information theory explanation of the fluctuation theorem, maximum entropy production and self-organized criticality in non-equilibrium stationary states. *J. Phys. A*, 36:631, 2003.

[74] J. C. Willems. Dissipative dynamical systems part II: Linear systems with quadratic supply rates. *Arch. Ration. Mech. Anal.*, 45:352–393, 1972.

[75] J. Loschmidt. *Sitz. Kais. Akad. d. W. Math. Naturw. II*, 73:128, 1876.

[76] D. J Evans and D. J. Searles. The fluctuation theorem. *Adv. Phys.*, 51:1529–1585, 2002.

[77] I. Prigogine and I. Stengers. *The end of certainty*. Simon and Schuster, 1997.

[78] H. Xu, A. Pumir, G. Falkovich, E. Bodenschatz, M. Shats, H. Xia, N. Francois, and G. Boffetta. Flight–crash events in turbulence. *Proc. Na*, 111(21):7558–7563, 2014.

[79] J. Jucha, H. Xu, A. Pumir, and E. Bodenschatz. Time-reversal-symmetry breaking in turbulence. *Phys. Rev. Lett.*, 113(5):054501, 2014.

[80] M. Danish and C. Meneveau. Multiscale analysis of the invariants of the velocity gradient tensor in isotropic turbulence. *Phys. Rev. Fluids*, 3:044604, 2018.

[81] G. Gallavotti. Dynamical ensembles equivalence in fluid mechanics. *Phys. D*, 105: 163–184, 1997.

[82] L. Biferale, D. Pierotti, and A. Vulpiani. Time-reversible dynamical systems for turbulence. *J. Phys. A*, 31:21, 1998.

[83] L. Rondoni and E. Segre. Fluctuations in two-dimensional reversibly damped turbulence. *Nonlinearity*, 12:1471, 1999.

[84] G. Gallavotti, L. Rondoni, and E. Segre. Lyapunov spectra and nonequilibrium ensembles equivalence in 2D fluid mechanics. *Physica D*, 187:338–357, 2004.

[85] J. Bardina, J. Ferziger, and W. C. Reynolds. Improved subgrid-scale models for large-eddy simulation. In *13th Fluid Plasma Dyn. Conf.*, page 1357, 1980.

[86] M. Germano, U. Piomelli, P. Moin, and W. H. Cabot. A dynamic subgrid-scale eddy viscosity model. *Phys. Fluids*, 3:1760–1765, 1991.

[87] G. S. Winckelmans, A. Wray, O. V. Vasilyev, and H. Jeanmart. Explicit-filtering large-eddy simulation using the tensor-diffusivity model supplemented by a dynamic smagorinsky term. *Phys. Fluids*, 13:1385–1403, 2001.

[88] D. Carati, G. S. Winckelmans, and H. Jeanmart. On the modelling of the subgrid-scale and filtered-scale stress tensors in large-eddy simulation. *J. Fluid Mech.*, 441: 119–138, 2001.

[89] V. Latora and M. Baranger. Kolmogorov-Sinai entropy rate versus physical entropy. *Phys. Rev. Lett.*, 82:520, 1999.

[90] S. A. Orszag. *Lectures on the statistical theory of turbulence.* Flow Research Incorporated, 1974.

[91] R. H. Kraichnan. Remarks on turbulence theory. *Adv. Math.*, 16:305–331, 1975.

[92] J. Eckmann, C. Pillet, and L. Rey-Bellet. Entropy production in nonlinear, thermally driven Hamiltonian systems. *J. Stats. Phys.*, 95:305–331, 1999.

[93] R. H. Kraichnan and D. Montgomery. Two-dimensional turbulence. *Rep. Prog. Phys.*, 43:547, 1980.

[94] T. Gilbert and J. R. Dorfman. Entropy production: From open volume-preserving to dissipative systems. *J. Stats. Phys.*, 96:225–269, 1999.

[95] D. J. Evans, E. G. D. Cohen, and G. P. Morriss. Probability of second law violations in shearing steady states. *Phys. Rev. Lett.*, 71:2401, 1993.

[96] D. J. Searles, L. Rondoni, and D. J. Evans. The steady state fluctuation relation for the dissipation function. *J. Stat. Phys.*, 128:1337–1363, 2007.

[97] J. Smagorinsky. General circulation experiments with the primitive equations: I. the basic experiment. *Mon. Weather Rev.*, 91:99–164, 1963.

[98] S. Ghosal, T. S. Lund, P. Moin, and K. Akselvoll. A dynamic localization model for large-eddy simulation of turbulent flows. *J. Fluid Mech.*, 286:229–255, 1995.

[99] C. Meneveau, T. S. Lund, and W. H. Cabot. A lagrangian dynamic subgrid-scale model of turbulence. *J. Fluid Mech.*, 319:353–385, 1996.

[100] D. K. Lilly. A proposed modification of the Germano subgrid-scale closure method. *Phys.Fluids A*, 4:633–635, 1992.

[101] G. K. Batchelor. *The theory of homogeneous turbulence.* Cambridge U. Press, 1953.

[102] O. Métais and M. Lesieur. Spectral large-eddy simulation of isotropic and stably stratified turbulence. *J. Fluid Mech.*, 239:157–194, 1992.

[103] G. Ayton, D. J. Evans, and D. J. Searles. A local fluctuation theorem. *J. chem. phys.*, 115:2033–2037, 2001.

[104] G. Michel and D. J. Searles. Local fluctuation theorem for large systems. *Phys. Rev. Let.*, 110:260602, 2013.

[105] C. Meneveau and K. R. Sreenivasan. The multifractal nature of turbulent energy dissipation. *J. Fluid Mech.*, 224:429–484, 1991.

[106] L. Biferale. Shell models of energy cascade in turbulence. *Annu. Rev. Fluid Mech.*, 35(1):441–468, 2003.

[107] B. Lüthi, S. Ott, J. Berg, and J. Mann. Lagrangian multi-particle statistics. *J. Turbul.*, 8:N45, 2007.

[108] A. Lozano-Durán, M. Holzner, and J. Jiménez. Multiscale analysis of the topological invariants in the logarithmic region of turbulent channels at a friction Reynolds number of 932. *J. Fluid Mech.*, 803:356–394, 2016.

[109] C. Meneveau and J. Katz. Conditional subgrid force and dissipation in locally isotropic and rapidly strained turbulence. *Phys. Fluids*, 11:2317–2329, 1999.

[110] F. Nicoud and F. Ducros. Subgrid-scale stress modelling based on the square of the velocity gradient tensor. *Flow Turbul. Combust.*, 62:183–200, 1999.

[111] P. Vieillefosse. Internal motion of a small element of fluid in an inviscid flow. *Physica A*, 125:150–162, 1984.

[112] A. Ooi, J. Martín, J. Soria, and M. S. Chong. A study of the evolution and characteristics of the invariants of the velocity-gradient tensor in isotropic turbulence. *J. Fluid Mech.*, 381:141–174, 1999.

[113] B. J. Cantwell. Exact solution of a restricted Euler equation for the velocity gradient tensor. *Phys. Fluids*, 4:782–793, 1992.

[114] A. Lozano-Durán, M. Holzner, and J. Jiménez. Numerically accurate computation of the conditional trajectories of the topological invariants in turbulent flows. *J. Comput. Phys.*, 295:805 – 814, 2015.

[115] C. Meneveau. Lagrangian dynamics and models of the velocity gradient tensor in turbulent flows. *Annu. Rev. Fluid Mech.*, 43:219–245, 2011.

[116] L. Chevillard, C. Meneveau, L. Biferale, and F. Toschi. Modeling the pressure Hessian and viscous Laplacian in turbulence: Comparisons with direct numerical simulation and implications on velocity gradient dynamics. *Phys. Fluids*, 20: 101504, 2008.

[117] B. Luethi, M. Holzner, and A. Tsinober. Expanding the Q–R space to three dimensions. *J. Fluid Mech.*, 641:497–507, 2009.

[118] K. K. Nomura and G. K. Post. The structure and dynamics of vorticity and rate of strain in incompressible homogeneous turbulence. *J. Fluid Mech.*, 377:65–97, 1998.

[119] C. G. Speziale, S. Sarkar, and T. B. Gatski. Modelling the pressure–strain correlation of turbulence: an invariant dynamical systems approach. *J. Fluid Mech.*, 227: 245–272, 1991.

[120] K. Ohkitani and S. Kishiba. Nonlocal nature of vortex stretching in an inviscid fluid. *Phys. Fluids*, 7:411–421, 1995.

[121] Z-S. She, E. Jackson, S. A. Orszag, J. C. R. Hunt, O. M. Phillips, and D. Williams. Structure and dynamics of homogeneous turbulence: models and simulations. *Proc. R. Soc. Lond. A*, 434:101–124, 1991.

[122] V. I. Oseledec. A multiplicative ergodic theorem. Lyapunov characteristic numbers for dynamical systems. *Trans. Moscow Math. Soc*, 19:197–231, 1968.

[123] D. Ruelle. Positivity of entropy production in nonequilibrium statistical mechanics. *J. Stat. Phys.*, 85:1–23, 1996.

[124] S. V. Ershov and A. B. Potapov. On the concept of stationary Lyapunov basis. *Physica D*, 118:167–198, 1998.

[125] S. Smale. Differentiable dynamical systems. *Bull. Am. Math. Soc.*, 73:747–817, 1967.

[126] A. Wolf, J. B. Swift, H. L. Swinney, and J. A. Vastano. Determining Lyapunov exponents from a time series. *Physica D*, 16:285–317, 1985.

[127] R. Grappin and J. Léorat. Lyapunov exponents and the dimension of periodic incompressible Navier–Stokes flows: numerical measurements. *J. Fluid Mech.*, 222: 61–94, 1991.

[128] J. A. Vastano and R. D. Moser. Short-time Lyapunov exponent analysis and the transition to chaos in Taylor–Couette flow. *J. Fluid Mech.*, 233:83–118, 1991.

[129] L. Keefe, P. Moin, and J. Kim. The dimension of attractors underlying periodic turbulent Poiseuille flow. *J. Fluid Mech.*, 242:1–29, 1992.

[130] M. Yamada and K. Ohkitani. Lyapunov spectrum of a chaotic model of three-dimensional turbulence. *J. Phys. Soc. Jpn.*, 56:4210–4213, 1987.

[131] L. van Veen, S. Kida, and G. Kawahara. Periodic motion representing isotropic turbulence. *Fluid Dyn. Res.*, 38:19, 2006.

[132] F. Moisy and J. Jiménez. Geometry and clustering of intense structures in isotropic turbulence. *J. Fluid Mech.*, 513:111–133, 2004.

[133] A. Lozano-Durán, O. Flores, and J. Jiménez. The three-dimensional structure of momentum transfer in turbulent channels. *J. Fluid Mech.*, 694:100–130, 2012.

[134] W. T. Ashurst, A. R. Kerstein, R. M. Kerr, and C. H. Gibson. Alignment of vorticity and scalar gradient with strain rate in simulated Navier–Stokes turbulence. *Phys. Fuids*, 30:2343–2353, 1987.

[135] J. C. del Álamo, J. Jimenez, P. Zandonade, and R. D. Moser. Self-similar vortex clusters in the turbulent logarithmic region. *J. Fluid Mech.*, 561:329–358, 2006.

[136] G. E. Elsinga and I. Marusic. Universal aspects of small-scale motions in turbulence. *J. Fluid Mech.*, 662:514–539, 2010.

[137] C. Meneveau. Statistics of turbulence subgrid-scale stresses: necessary conditions and experimental tests. *Phys. Fluids*, 6(2):815–833, 1994.

[138] M. Lesieur and O. Metais. New trends in large-eddy simulations of turbulence. *Ann. Rev. Fluid Mech.*, 28:45–82, 1996.

[139] G. L. Eyink. Locality of turbulent cascades. *Physica D*, 207:91–116, 2005.

[140] G. L Eyink and H. Aluie. Localness of energy cascade in hydrodynamic turbulence. I: Smooth coarse graining. *Phys. Fluids*, 21:115107, 2009.

[141] J. A. Domaradzki, B. Teaca, and D. Carati. Locality properties of the energy flux in turbulence. *Phys. Fluids*, 21:025106, 2009.

[142] U. Piomelli, W. H. Cabot, P. Moin, and S. Lee. Subgrid-scale backscatter in turbulent and transitional flows. *Phys. Fluids*, 3:1766–1771, 1991.

[143] J. M. Burgers. A mathematical model illustrating the theory of turbulence. *Adv. Appl. Mech.*, 1:171–199, 1948.

[144] R. Betchov. An inequality concerning the production of vorticity in isotropic turbulence. *J. Fluid Mech.*, 1:497–504, 1956.

[145] S. Motoki, G. Kawahara, and M. Shimizu. Maximal heat transfer between two parallel plates. *J. Flud Mech.*, 851, 2018.

[146] C. T. Pringle, A. P. Willis, and R. R. Kerswell. Minimal seeds for shear flow turbulence: using nonlinear transient growth to touch the edge of chaos. *J. Fluid Mech.*, 702:415–443, 2012.

[147] L. van Veen, A. Vela-Martin, and G. Kawahara. Time-periodic inertial range dynamics. *arXiv:1809.08649*, 2018.

[148] W. G. Hoover. *Computational statistical mechanics*. Elsevier, 2012.

[149] G. L. Brown and A. Roshko. On density effects and large structure in turbulent mixing layers. *J. Fluid Mech.*, 64:775–816, 1974.

[150] A. Lozano-Durán and J. Jiménez. Time-resolved evolution of coherent structures in turbulent channels: characterization of eddies and cascades. *J. Fluid Mech.*, 759: 432–471, 2014.